



Cape Peninsula  
University of Technology

**DEVELOPMENT OF A HAND-HELD MULTICELL INVERTER- BASED  
ULTRASONIC PLASTIC WELDER**

by

**EDWARD DAVIES**

Thesis submitted in fulfilment of the requirements for the degree

Magister of Technologiae: Electrical Engineering

in the Faculty of Engineering

at the Cape Peninsula University of Technology


Supervisor: Dr R H Wilkinson

Co-supervisor: Prof. J R Davies

Cape Town  
December 2009

**DECLARATION**

I, Edward Davies, declare that the contents of this thesis represent my own unaided work, and that the thesis has not previously been submitted for academic examination towards any qualification. Furthermore, it represents my own opinions and not necessarily those of the Cape Peninsula University of Technology.

**Signed**  \_\_\_\_\_

\_\_\_\_\_ **Date**

## ABSTRACT

This thesis presents the design and development of a multicell inverter for ultrasonic plastic welding applications and other ultrasonic applications. An overview of the main multilevel topologies is given, but this research focuses on the multicell inverter, because of its capacitor voltage balancing properties.

Loading effects of various plastic materials to an ultrasonic plastic welding tool are provided in this thesis. A simple method to create an approximate electrical equivalent circuit of the ultrasonic welding tool, using an impedance analyser, loaded with different plastics is discussed and illustrated.

Experimental results of the four-level multicell inverter driving a resistive load and an ultrasonic transducer tool are presented in this thesis. These results provide proof that the multicell inverter topology is capable of driving a non-linear load.

The inverter was tested with the ultrasonic load as an ultrasonic plastic welder and an ultrasonic drill. The welding joints on the plastic samples are also evaluated in order to evaluate whether or not this solution is suitable for plastic welding. The ultrasonic drilling results are also shown in this thesis.

It is further illustrated that the ultrasonic tool and power supply combination may be used in other ultrasonic applications.

## ACKNOWLEDGEMENTS

### I wish to thank:

- My Lord and Saviour, Jesus Christ for the abilities and opportunities He has provided me during my life.
- My parents, Lynton and Esté Davies for their support and love throughout my life.
- My supervisors, Dr RH Wilkinson and Prof. JR Davies for their insights, support and help during my research period.
- Prof. G de Jager and Mr J Wheeler for their valuable insights and suggestions.
- To all my colleagues at the Centre for Instrumentation Research, especially Mr Brevin Claassen, Mr Mark Matthews and Mr Shaheen Johnson for creating a fun and supportive environment.

**“I can do all things through Christ which strengthens me.” – Philippians 4:13 (KJV)**

The financial assistance of the National Research Foundation (NRF) towards this research is acknowledged. Opinions expressed in this thesis and conclusions reached are those of the author's and are not necessarily attributable to the NRF.

## TABLE OF CONTENTS

<b>Declaration</b>		<b>ii</b>
<b>Abstract</b>		<b>iii</b>
<b>Acknowledgements</b>		<b>iv</b>
<b>List of figures</b>		<b>ix</b>
<b>List of tables</b>		<b>xiii</b>
<b>Nomenclature</b>		<b>xiv</b>
<b>CHAPTER ONE: OVERVIEW</b>		<b>1</b>
1.1	Introduction to ultrasonic plastic welding	1
1.2	Multilevel inverter application	3
1.3	Four aims and objectives	3
1.4	Procedure	3
1.5	Scope and limitations	4
1.6	Thesis overview	4
<b>CHAPTER TWO: BACKGROUND STUDY OF ULTRASONIC PLASTIC WELDING SYSTEMS</b>		<b>5</b>
2.1	Fundamentals of plastic welding	5
2.1.1	Effects of ultrasonic welding on plastics materials	5
2.2	Ultrasonic plastic welding systems	6
2.2.1	Power supply	6
2.2.2	The ultrasonic transducer	7
2.2.3	The booster	8
2.2.4	The horn	8
2.3	Applications of ultrasonic plastic welding	9
2.4	The multilevel inverter	10
2.4.1	Multicell inverter topology	11
2.4.2	Diode-clamped multilevel inverter	13
2.4.3	Cascaded multilevel inverter	16
2.4.4	The chosen topology	17
2.5	Conclusion	17

<b>CHAPTER THREE: THE ULTRASONIC TRANSDUCER AS AN ELECTRICAL LOAD</b>	<b>18</b>
3.1 Bolted Langevin Type (BLT) transducers	18
3.2 Characteristics of BLT transducers	20
3.3 Modelling a BLT transducer	20
3.3.1 Butterworth Van Dyke (BVD) piezoelectric disc model	21
3.3.2 Electromechanical coupling factor	22
3.3.3 Mechanical quality factor	23
3.3.4 Modelling the basic parameters of a piezoelectric transducer	23
3.3.5 Calculated equivalent circuits versus measured systems results	24
3.4 Conclusions	25

<b>CHAPTER FOUR: THE SELECTION AND DESIGN OF AN ULTRASONIC INVERTER</b>	<b>28</b>
4.1 Design of the multicell inverter	29
4.1.1 Introduction	29
4.1.2 Design specifications	29
4.1.3 Design of the flying capacitors	30
4.1.4 Design of the DC bus capacitors	34
4.1.5 Design of the bleeding resistors	35
4.1.6 Design of the output filter	37
4.1.7 Component selection	39
4.2 Heat sink design notes	39
4.2.1 Conduction and switching power losses	40
4.2.2 PCB heat sink	44
4.3 Fibre optic isolation	45
4.4 Auxiliary power supply	46
4.4.1 Auxiliary power supply specifications	46
4.4.2 Auxiliary power supply design	46
4.4.3 Half-bridge inverter stage	47
4.4.4 Multiple output step-down transformer	48
4.4.5 Rectifying stage	52
4.5 Switching signal generator	53
4.5.1 Introduction to pulse-width modulation control (PWM)	53

4.5.2	Sinusoidal pulse-width modulation	53
4.5.3	Interleaved SPWM technique	54
4.6	Conclusions	55
 <b>CHAPTER FIVE: EXPERIMENTAL RESULTS</b>		<b>57</b>
5.1	Testing of auxiliary power supply	57
5.2	Testing of the multicell inverter	59
5.2.1	Testing a single commutation cell as a half-bridge inverter	59
5.2.2	Testing the 3 cell multicell inverter topology with a resistive load	62
5.2.3	Testing the 3 cell multicell inverter topology with the ultrasonic load	67
 <b>CHAPTER SIX: PLASTIC WELDER RESULTS</b>		<b>74</b>
6.1	Testing the system as a plastic welder	74
6.1.1	Spot welding results	75
6.1.2	The tensile strength test	78
6.1.3	The chemical quality test	80
6.1.4	Plastic welding test conclusion	80
6.2	Testing the system as an ultrasonic drill	82
6.3	Conclusions	83
 <b>CHAPTER SEVEN: CONCLUSIONS AND RECOMMENDATIONS</b>		<b>84</b>
7.1	Auxiliary power supply	84
7.2	Multicell inverter	84
7.3	Ultrasonic plastic welding system	84
7.4	Conclusions to main research questions	84
7.5	Thesis contributions	85
7.6	Future work	86
 <b>REFERENCES</b>		<b>87</b>

<b>APPENDICES</b>	<b>90</b>
Appendix A: ABBEON CAL, INC. ULTRASONIC PLASTIC WELDER QUOTE	90
Appendix B: SHARPERTEK ULTRASONIC WELDER SPECIFICATIONS AND QUOTE	91
Appendix C: CALCULATED EQUIVALENT PARAMETERS OF THE ULTRASONIC TRANSDUCER WITH BOOSTER AND HORN IN VARIOUS LOAD CONDITIONS	93
Appendix D: SCHEMATIC DIAGRAMS	95
Appendix E: PCB LAYOUTS	100
Appendix F: PROGRAMME	107
Appendix G: MEASURED AGAINST SIMULATED ADMITTANCE VERSUS FREQUENCY PLOTS OF THE ULTRASONIC TRANSDUCER WITH DIFFERENT LOADS	108
Appendix H: TENSILE STRENGTH TEST RESULTS	110
Appendix I: PSIM SIMULATION SETUP	112



## LIST OF FIGURES

Figure 1.1: The admittance versus frequency plot of an ultrasonic transducer under various loads to illustrate resonance behaviour	2
Figure 2.1: A typical power supply arrangement for an ultrasonic plastic welder	6
Figure 2.2: Ultrasonic plastic welding work-piece broken into three comprising components	7
Figure 2.3: Mason's simplified electrical equivalent representation of a piezoelectric transducer as a load (Mason, 1935)	8
Figure 2.4: Various basic horn profiles and their relative gains (Dukane, 2005)	9
Figure 2.5: Three level multicell inverter topology	11
Figure 2.6: The conduction order of the switches in a 2 cell multicell inverter together with the unfiltered output waveform of the multicell inverter	12
Figure 2.7: Three level diode-clamped multilevel inverter topology	14
Figure 2.8: A cascaded multilevel inverter topology	16
Figure 3.1: A simplified mechanical equivalent diagram of a BLT transducer (Green, 1999)	18
Figure 3.2: Ultrasonic transducer consisting of head mass ( $M_1$ ), piezoelectric disc stack (A) and the tail mass ( $M_2$ ). The booster and horn (C) combination is used with the BLT transducer for testing	19
Figure 3.3: Mason's equivalent transmission line model	20
Figure 3.4: Admittance versus frequency plot of a transducer where C is the thickness resonant mode of the transducer and A, B and D are the radial and length modes of resonance	21
Figure 3.5: BVD equivalent circuit simplified for a single resonance mode	22
Figure 3.6: Admittance versus frequency plot pointing out the maxima and minima points of the ultrasonic transducer when loaded with PP	22
Figure 3.7: A comparison between the measured admittance values versus frequency and the calculated values with the aid of a BVD model of a BLT transducer with a horn and booster in free air. The calculated theoretical circuit parameters are as follows: $C_0 = 12.6 \text{ nF}$ , $L_m = 0.023 \text{ H}$ , $R_m = 10.31 \text{ } \Omega$ and $C_m = 2.31 \text{ nF}$	25
Figure 3.8: Comparison of the equivalent circuit parameters calculated from the measured admittance versus frequency scans	25
Figure 3.9: The admittance vector diagram for a piezoelectric vibrator. Maximum and minimum admittances are represented by $f_m$ and $f_n$ in the diagram. The series and parallel mechanical resonances, $f_s$ and $f_p$ respectively, are also shown on diagram together with $R$ and $G_s$ which represents the mechanical	26

damping of the resonance and the dielectric loss conductance respectively. The half power points(-3dB) are marked as $f_1$ and $f_2$ (Stansfield, 1990)	
Figure 3.10: The simulated versus the measured admittance circles of an ultrasonic transducer	27
Figure 4.1: Various mechanical modes of an ultrasonic transducer shown with the main operating mode of the transducer	28
Figure 4.2: Diagram of the multicell inverter with the inductor currents used for designing the flying capacitors	31
Figure 4.3: Ripple current in the DC bus capacitors in the multicell inverter	34
Figure 4.4: A parallel RC circuit	36
Figure 4.5: A second order low-pass LC filter	37
Figure 4.6: Impedance versus frequency plot of the physically constructed filter measured with the HP 4192A impedance analyser	38
Figure 4.7: Phase versus frequency plot of the physically constructed filter measured with the HP 4192A impedance analyser	38
Figure 4.8: A thermal representation of the system	42
Figure 4.9: A visual representation of the main contributing power loss types in the system	44
Figure 4.10: The graph shows the PCB heat sink area required for the calculated thermal resistance of the system (Bob Wolbert, 2006)	45
Figure 4.11: The overview of the half-bridge inverter and step-down transformer stage of the auxiliary power supply	47
Figure 4.12: The half-bridge inverter with the components as used in the project	48
Figure 4.13: A waveform diagram illustrating the duty cycle of a signal	51
Figure 4.14: The rectification and regulation stage	52
Figure 4.15: Reference sinusoidal waveform being compared with a high frequency carrier triangle waveform. The resulting SPWM signal from the comparison between the reference and the carrier waveform is shown	53
Figure 4.16: The resulting output of a 3 cell multicell inverter with the interleaved SPWM switching scheme	54
Figure 4.17: The FPGA development board used to generate the switching signals for the inverter	55
Figure 4.18: The 3 cell multicell inverter prototype	56
Figure 5.1: The output of the inverter of the auxiliary power supply on the primary of the transformer	57
Figure 5.2: The output of the inverter on the secondary of the transformer	58
Figure 5.3: The regulated outputs of one of the regulating stages	58
Figure 5.4: Block diagram illustrating the experimental setup used for testing half-	59

bridge inverter	
Figure 5.5: The inverter output at a switching frequency of 100 kHz	60
Figure 5.6: The gate signals on the IRF520 MOSFET at 300 kHz	60
Figure 5.7: The output of the half-bridge inverter at 300 kHz driving a resistive load	61
Figure 5.8: The equivalent circuit of a power MOSFET device (Anon, 2008)	61
Figure 5.9: The output of the inverter after leads were shortened and D2PAK device was used	62
Figure 5.10: Block diagram illustrating the experimental setup used for testing the 3 cell multicell inverter with a resistive load	63
Figure 5.11: Unfiltered output of the multicell inverter at a switching frequency of 80 kHz or an apparent switching frequency of 240 kHz	63
Figure 5.12: Filtered output of the multicell inverter at a switching frequency of 80 kHz or an apparent switching frequency of 240 kHz	64
Figure 5.13: A screen shot of the 300 kHz complimentary pair of switching signals for the three commutation cells taken from a logic analyser	64
Figure 5.14: The simulated flying capacitor voltage levels	65
Figure 5.15: The flying capacitor voltage levels	65
Figure 5.16: Unfiltered output of the multicell inverter at a switching frequency of 300 kHz or an apparent switching frequency of 900 kHz	66
Figure 5.17: The frequency spectrum measurement of the unfiltered waveform shown in Figure 5.16	66
Figure 5.18: The filtered output voltage(top) and current (bottom) waveforms of the multicell inverter driving a wire wound resistor that contains a small inductance, causing the output current to lag the voltage	67
Figure 5.19: Block diagram illustrating the experimental setup used for testing the 3 cell multicell inverter with an ultrasonic load	68
Figure 5.20: The flying capacitor voltage levels with the ultrasonic transducer	69
Figure 5.21: The simulated output voltage and current waveforms of the multicell inverter driving the ultrasonic transducer loaded with a Perspex sample	69
Figure 5.22: The simulated output voltage (top) and current (bottom) waveforms that were captured after filtering of the multicell inverter driving the ultrasonic transducer loaded with Perspex sample	70
Figure 5.23: The filtered output voltage and current waveforms of the multicell inverter driving the ultrasonic transducer loaded with Perspex sample	70
Figure 5.24: The filtered simulated output voltage and current waveforms of the multicell inverter driving the ultrasonic transducer loaded with a HDPE sample	71
Figure 5.25: The filtered output voltage and current waveforms of the multicell inverter driving the ultrasonic transducer loaded with a HDPE sample	71

Figure 5.26: The output voltage and current waveforms into the ultrasonic transducer to calculate the output power	72
Figure 6.1: Typical tensile strength testing apparatus	75
Figure 6.2: Experimental ultrasonic plastic welding setup	76
Figure 6.3: ABS samples from a credit card spot welded	77
Figure 6.4: Pure ABS samples spot welded together	77
Figure 6.5: Polyester samples spot welded	77
Figure 6.6: PVC strip samples spot welded	77
Figure 6.7: PET samples spot welded	78
Figure 6.8: The Instron 8801 material strength tester	79
Figure 6.9: The adaptors used to secure the samples for tensile strength tests	80
Figure 6.10: A spot welded sample immersed in acetone	80
Figure 6.11: Unfiltered and filtered waveforms while performing plastic welding	81
Figure 6.12: The top view of a 17mm thick HDPE sample after being drilled through	82
Figure 6.13: The bottom view of Figure 5.31	82
Figure 6.14: Drilled 3.0mm Perspex sample	82
Figure 6.15: Drilled 3.0mm polypropylene sample	83
Figure 6.16: Drilled acetal sample	83

## LIST OF TABLES

Table 4.1: Design specifications of an ultrasonic inverter	29
Table 4.2: MOSFET data used for conduction and switching power losses	41
Table 4.3: Calculated answers for the heat sink design	44
Table 4.4: Specifications of the auxiliary power supply	46
Table 4.5: Transformer output ratings	48
Table 4.6: The design parameters of the transformer	49

## NOMENCLATURE

<b>Terms/Acronyms/Abbreviations</b>	<b>Definition/Explanation</b>
A/D	Analog to digital
ABS	Acrylonitrile butadiene styrene
AC	Alternating current
ASTM	American Society of Testing and Materials
B	Magnetic flux
BLT	Bolted langevin type
BVD	Butterworth Van Dyke
C	Capacitor
CIR	Centre for Instrumentation Research
CT	Current transformer
D	Duty cycle
DC	Direct current
DSP	Digital signal processor
E	Energy
EMI	Electromagnetic interference
FCMLI	Flying capacitor multilevel inverter
FPGA	Field programmable gate array
HDPE	High density polyethylene
K	Force of the spring
$k_{\text{eff}}$	Electromagnetic coupling factor
L	Inductance
M	Mass
$m_a$	Modulation index of the top switch
$m_b$	Modulation index of the bottom switch
MOSFET	Metal oxide semiconductor field effect transistor
MSSP	Master synchronous serial port
N	Number of turns in a transformer
$p$	Number of commutation cells in a multicell inverter
P	Power
PCB	Printed circuit board
PE	Polyethylene
PET	Polyethylene terephthalate
PIC	Programmable interrupt controller
PP	Polypropylene

PVC	Polyvinyl chloride
PWM	Pulse width modulation
Q	Quality factor
RMS	Root means square
SCK	Serial clock
SDO	Serial data out
SPI	Serial peripheral interface
SPWM	Sinusoidal pulse width modulation
T	Temperature
USD	United States Dollar
Y	Admittance
ZAR	South African Rand
$\lambda$	Wavelength
$\Phi$	Phase shift
$\omega$	Angular frequency

# CHAPTER ONE

## OVERVIEW

### 1.1 Introduction to ultrasonic plastic welding

Ultrasonic welding is a process wherein thermoplastics are joined by using heat generated from an ultrasonic motion at high frequency (high rate of vibration). Such mechanical motion is achieved through conversion of high frequency electrical energy into high frequency mechanical movement. This movement, in conjunction with applied force, generates frictional heat at the joining area of plastic samples. This causes the plastic material to melt, forming a molecular bond between the samples.

Ultrasonic welding is a major industrial process for joining thermoplastics, as it is economical and satisfies the intense demand for ultra-fine finishing of welded joints. The ultrasonic welding process is also rapid, typically less than 1 second (Mistry, 1997), with the benefit of the exclusion of adhesives or welding flux. In applications where thermoplastics must be joined, it is difficult to bond them with microwave joining because of their low dielectric losses (Tsujino, *et al.* 1996). Other plastic welding techniques, such as hot gas welding, extrusion welding, contact welding and hot plate welding, are temperature sensitive and difficult to control with refined plastic materials, such as polyethylene. It is usually a preferred choice on assembly line productions thanks to high energy efficiency, high productivity, low cost and ease of automation. This welding technique is used mainly in mass production, as careful design of components and fixtures is required for a successful weld. Examples of applications are domestic appliances and medical blood filters (Rajagopal, 2008).

Industry, however, faces a major problem with ultrasonic welding - the process is material dependant. Welding machines are usually optimised for a specific type of plastic material with a predetermined thickness. This makes it difficult for a manufacturer to substitute standard plastic for something stronger. It is well known the resonance behaviour of an ultrasonic transducer changes as the load (in this case the variety of plastic) changes (ISA, 1962). This is illustrated in Figure 1.1. This admittance versus frequency plot illustrates the resonance behaviour of an ultrasonic transducer under varied load conditions, in this case differing plastic samples. This is why it is difficult or near-impossible to design a generic ultrasonic welding machine. If this problem could be overcome it would be possible to design such a welding machine for use in hand-held application. If this was achieved, generic welding machines could be developed for industrial applications, making the set-up simpler and a substitution of plastic materials possible.



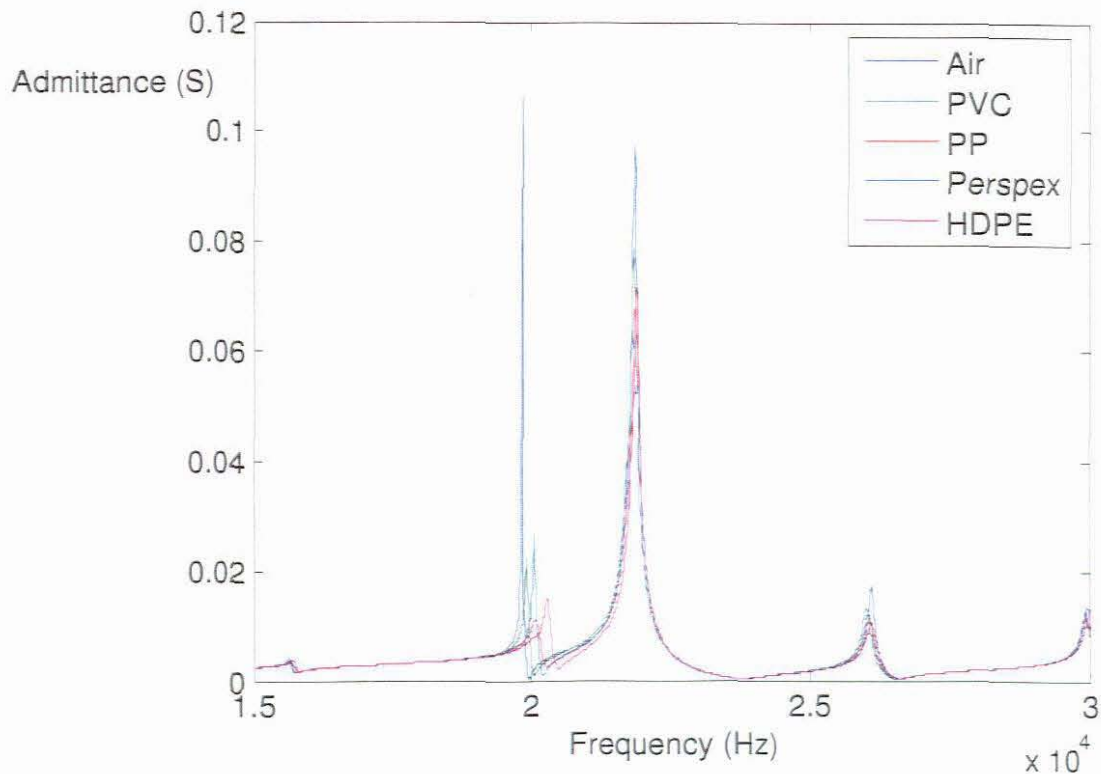


**Figure 1.1: The admittance versus frequency plot of an ultrasonic transducer under various loads to illustrate resonance behaviour**

Research by J Tsujino et al. (Tsujino, 2004) indicates the higher the operating frequency of an ultrasonic plastic welder, the more effective the system because of higher vibration loss of the plastic welding specimens. It is further mentioned that the welded strength improved as the operating frequency of the system increased. The welded strength and area were further improved by simultaneously driving the ultrasonic transducer at fundamental and higher resonance frequencies. This caused the ultrasonic transducer to be more efficient with its conversion of electric energy to sound energy.

A more local problem (in South Africa) is the cost involved in ultrasonic plastic welding systems (refer to Appendices A and B for examples). To create a cost-effective alternative for ultrasonic power supplies was an added motivation in carrying out this project. From the quotes received for the power supplies (see Appendices A and B), the cost according to the exchange rate (2 April 2009, 1 USD = 9.33688 ZAR) in South African Rand, power supplies cost R 44 817.02 and R 29 878.07 respectively. By manufacturing such power supplies locally cost could be significantly reduced.

## 1.2 Multilevel inverter application

Multilevel inverters are shown to reduce the size and cost of power supply systems, as lower power switches and smaller filtering components can be used, in turn reducing systemic cost. Higher power levels can be reached with standard low cost switches and an increased number of switches is justified with reduction in size of the output filter (Meynard et al, 2002).

Various multilevel inverter topologies have been developed. One such topology is the Flying capacitor multilevel inverter (FCMLI) or multicell inverter topology. This has the advantage of implementing cell capacitors which act as "voltage balancers." A *balanced* capacitor voltage means each cell capacitor remains at its assigned steady-state voltage (Wilkinson, 2004). This converter topology has to date not been tested with an ultrasonic load. If it proves to work sufficiently with an ultrasonic load, then it could open many doors to exciting possibilities of implementing a multicell inverter.

## 1.3 Four aims and objectives

The first aim was to study, design, build and test, if possible, an FCMLI to drive an ultrasonic load; the ultrasonic transducer is a non-linear, electromechanical load.

This led to a second objective - which was to research a rapid simple solution to measure an equivalent electrical circuit for an ultrasonic transducer - a useful tool to simulate any given transducer in computer simulation models with the use of an impedance analyser.

A third aim was to test if the developed ultrasonic plastic welding system was able to produce sound welded joints, ultimately testing the effectiveness of the entire design.

A fourth objective was to investigate whether the system was sufficiently versatile to be used in other ultrasonic applications. The reason for this investigation was to open doors and to create interest for development in the field of ultrasonic technology, by proving that multicell inverters can efficiently drive ultrasonic transducers in various ultrasonic applications.

## 1.4 Procedure

The resonance behaviour of the ultrasonic plastic spot welding tool was studied to help to design the multicell inverter. The electrical equivalent model of the ultrasonic transducer was calculated and results compared against measured admittance scans. The multicell inverter was then designed and populated. The multicell inverter prototype was tested with a resistive and an ultrasonic load. The measured results of the multicell inverter were compared with the simulated results using the calculated equivalent circuit models; the system was then tested as an ultrasonic plastic spot welder.

## 1.5 Scope and delineation

The study focuses on the design of an ultrasonic plastic welder using a multicell inverter topology. The inverter needed to be driven only at the main mode of resonance and, therefore, the derived equivalent electrical model of the ultrasonic transducer had to simulate only the main resonance mode. It was desired to prove the multicell inverter topology could drive an ultrasonic load. The materials used as samples for the plastic spot welding were acrylonitrile butadiene styrene (ABS), polyester, polyvinyl chloride (PVC) and polyethylene terephthalate (PET). To measure the effectiveness of the ultrasonic plastic spot welding system, the tensile strength of the spot welds were tested according to the ASTM D638 testing procedure from the American Society of Testing and Materials (ASTM).

## 1.6 Thesis overview

A brief overview of the research and work undertaken in each chapter of this study is as follows:

**Chapter 2:** Explains the theoretical background of ultrasonic plastic welding and background information on other topics used throughout this thesis.

**Chapter 3:** Discusses the behaviour of an ultrasonic transducer as a load and the methodology for calculating its equivalent circuit parameters.

**Chapter 4:** Covers the selection and design of the ultrasonic inverter used in this project.

**Chapter 5:** Presents and discusses experimental results obtained of the multicell inverter driving linear and non-linear loads.

**Chapter 6:** Discusses the experimental tests and results obtained of the system as an ultrasonic plastic welder.

**Chapter 7:** Summarises the thesis with conclusions and recommendations for further development.

## CHAPTER TWO BACKGROUND STUDY OF ULTRASONIC PLASTIC WELDING SYSTEMS

### 2.1. Fundamentals of plastic welding

Ultrasonic plastic welding is a process whereby plastics are joined or reshaped by melting or softening through the use of heat generated from a mechanical movement at a high frequency (Mistry, 1997). This high frequency mechanical movement is achieved by the conversion of high frequency electrical energy into high frequency mechanical movement. This type of conversion of energy is called electromechanical conversion. This mechanical movement, in conjunction with applied force, will create frictional heat at the plastic specimens' joining area, which in turn will cause the plastic material to melt, creating a molecular bond between the plastic specimens (Troughton, 2008).

#### 2.1.1 Effects of ultrasonic welding on plastic materials

There are two main groups of plastics: Thermosets and thermoplastics.

- **Thermosets**

These plastics are comprised of large continual chains of chemical molecules, which undergo a permanent reaction to form a close networked structure with strong covalent bonds (Mistry, 1997). When the material is cool its rigidity emanates from the cross-linked structure of the molecules. A disadvantage of this type of plastic material is an inability to be welded or joined together (Mistry, 1997). Plastic welders, therefore, cannot be used to join such plastics. This is because the cross-links prevent their molecular chains from diffusing and flowing freely. If excess heat is applied to thermoset materials they degrade (Mistry, 1997).

Examples of thermosets are urea formaldehyde ( $C_3H_6N_2O_3$ ), melamine formaldehyde ( $C_4H_6N_6O$ ) and polyurethane ( $C_{25}H_{42}N_2O_6$ ).

- **Thermoplastics**

Thermoplastics are also made up of large continual chains of chemical molecules known as "mers", which when joined form polymers (Mistry, 1997). The outcome of this process to form polymers is described as polymerisation. The links between the chain molecules of thermoplastics are fundamentally linear and devoid of cross-links. With the application of heat, these plastics melt, flow and are, therefore, suitable for welding (Mistry, 1997).

Two thermoplastic materials which do not weld easily with ultrasonic plastic welding are polypropylene (PP) and polyethylene (PE).

## 2.2. Ultrasonic plastic welding systems

The complete system is usually comprised of four main components. These are the power supply, the transducer (in our case the ultrasonic transducer), the amplitude modifying device (booster) and the acoustic tool (horn). Figure 2.1 shows a typical arrangement of an ultrasonic plastic welding system.

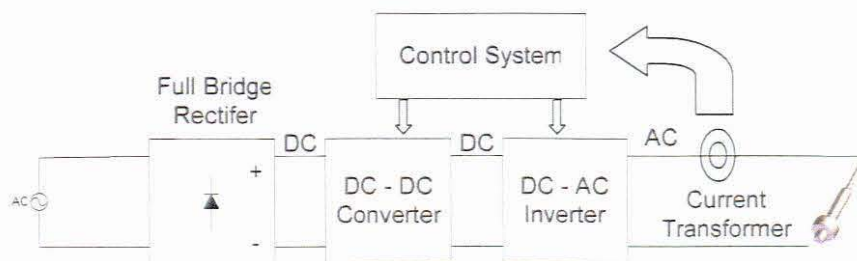


Figure 2.1: A typical power supply arrangement for an ultrasonic plastic welder

### 2.2.1 Power supply

The function of an ultrasonic plastic welding power supply is to convert the low frequency AC voltage from the mains into a high frequency AC output voltage at a specified output power to the load. Such power supplies usually operate in a frequency range of 20 to 40 kHz (Malloy, 1994:405).

The low frequency mains voltage is converted to a DC voltage by a rectifier (usually a bridge rectifier) and a parallel capacitor which acts as a smoothing capacitor. Then a DC – DC converter is used to either increase or decrease the voltage to the inverter by means of a buck or boost regulator. An inverter, usually in half-bridge or full-bridge configuration, converts the DC voltage back to a high frequency AC voltage. This high frequency AC voltage is supplied to the ultrasonic load made up of the ultrasonic transducer, the booster and the horn.

The control system is the core of the power supply and controls output power and frequency. The control system receives sampled input data, which represents voltage and current values at various stages of the power supply and makes the necessary calculations to send output signals to the switches which then produce the correct output to the ultrasonic load.

### 2.2.2 The ultrasonic transducer

An ultrasonic transducer is a device which converts applied electrical energy into mechanical acoustic energy. The acoustical energy generated is above human audible frequency range, usually above 20 kHz. The ultrasonic plastic welding work-piece is illustrated in Figure 2.2.

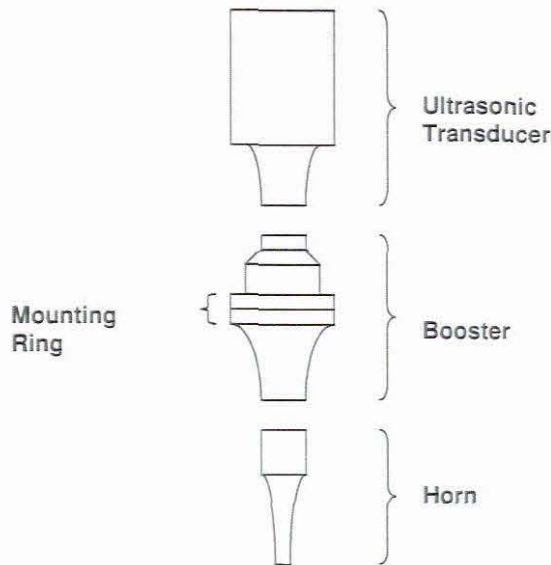


Figure 2.2: Ultrasonic plastic welding work-piece broken into three comprising components

The transducer consists of piezoelectric ceramic elements separated by thin metal plates, all firmly clamped under pressure. When an alternating voltage ( $dV/dt$ ) is applied to a piezoelectric element, a corresponding electrical field ( $dE/dt$ ) is produced across it and a variation in thickness ( $dL/dt$ ) induced. The variation in thickness of the ceramic discs results in the generation of a pressure wave ( $dP/dt$ ). Because of the nature of atoms and molecules in a solid object the pressure wave propagates through the material and is reflected by the end metal mass of the converter. The displacement at the edge of the transducer is extremely small (20 micron for a 20 kHz transducer) (Levy et al, 1993) and, therefore, the displacement distance needs to be amplified by a horn and a booster.

Figure 2.3 shows Mason's simplified equivalent circuit of a piezoelectric transducer as a load, where the electrical branch comprises of  $C_o$  and the mechanical branch comprises of  $R_m$ ,  $L_m$  and  $C_m$  (Mason, 1935).

where:  $V$  refers to the velocity of sound in material (m/s)  
 $f$  refers to the frequency of oscillation (Hz)  
 $\lambda$  refers to the wavelength (m)  
 $N$  refers to the oscillation mode

It can be seen that the higher the frequency of operation, so the smaller the acoustic wavelength will be and consequently the smaller the horn. This relation is linear; a 60 kHz horn will be half the size of a 30 kHz horn.

The horns have to be constructed from a material to propagate the ultrasonic energy with as little attenuation as possible. The metals usually used for manufacturing of ultrasonic horns are titanium or any other high-strength aluminium alloy. Both offer excellent acoustic properties. For durable, long lasting, wear-resistant horn tips, custom machined tips coated with chrome, titanium nitride or carbide could be connected to the horn.

The amplification factor of the ultrasonic horn is also determined by its slope and profile. There are various standard profiles which provide different amplification ratios. The selection of a specific profile of a horn depends on the application at hand. The basic horn shapes consist of straight, exponential, catenoidal and stepped profiles; these shapes are illustrated in Figure 2.4 (Dukane, 2005).





Horn Illustration				
<b>Profile</b>	Straight	Exponential	Catenoidal	Step
<b>Gain</b>	None	Low	Medium	High

Figure 2.4: Various basic horn profiles and their relative gains (Dukane, 2005)

### 2.3 Applications of ultrasonic plastic welding

Plastic joining by means of ultrasound is rapidly replacing conventional techniques such as solvent welding, contact welding, hot gas welding and hot plate welding. There are various different ultrasonic plastic joining techniques which require differently shaped and sized transducers.

The object of this study is to focus on plastic welding where the process is to generate a melt at the mating surfaces of two thermoplastic specimens using a hand-held spot welding probe. Some benefit of using ultrasonic plastic welding over conventional techniques includes the energy efficiency, high productivity gained from short weld times and a clean assembly process, without need for consumables such as adhesives, screws and solvents (Ling et al, 2006).

Applications where some or all such conditions are necessary or beneficial and where ultrasonic plastic welding is used are: (Suslick, 1988:111)

- Home appliances where high volumes are produced and cosmetic appearance and strength are important factors;
- electrical products such as terminal blocks, connectors and switches where high volumes are produced and high reliability is required;
- consumer products where high precision is required;
- medical applications where non-contamination and an ability to operate in a clean environment is as important as the weld strength. These applications include arterial filters, cardiometry reservoir, blood filters and gas filters;
- toy industry where the elimination of screws, solvents and adhesives are additional benefits to ensure the products are safe and strong.
- automotive industry in applications such as lenses, filters, instrument clusters, glove box doors and mass airflow sensors and,
- packaging industry benefits from the good cosmetic appearance. Tamper-evident seals are made for blister packs with the use of ultrasonic plastic welding. Applications in this industry include juice pouches, juice cartons and plastic coated paper cups.

## **2.4 The multilevel inverter**

A brief overview of various multilevel topologies is presented with reasons for choosing the multicell inverter as the topology for this study.

Multilevel converters produce an output voltage waveform with a low harmonic content (Meynard et al, 1992). A multilevel inverter produces a stepped output voltage waveform at different levels from a DC bus. The more levels the output has, the smaller the voltage step. The three most common multilevel inverter topologies mentioned in literature are the multicell inverter topology, the diode-clamped multilevel inverter topology and the cascaded multilevel inverter topology (Tolbert, 1998; Rodriguez, 2002; Soto, 2002; Meynard, 1995; Meynard, 1992). These topologies will be briefly discussed in the following subsections.



### 2.4.1 Multicell inverter topology

The multicell inverter topology is illustrated in Figure 2.5.

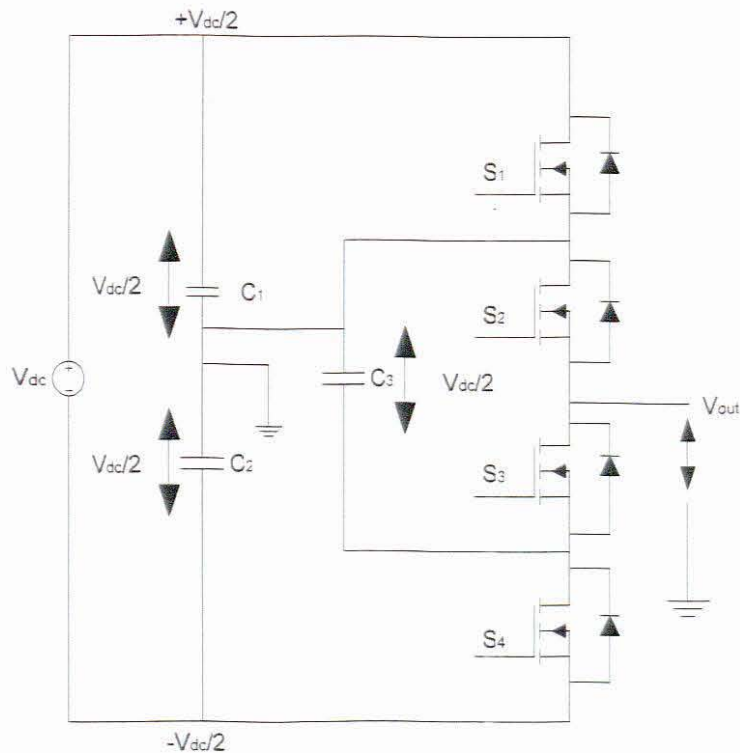
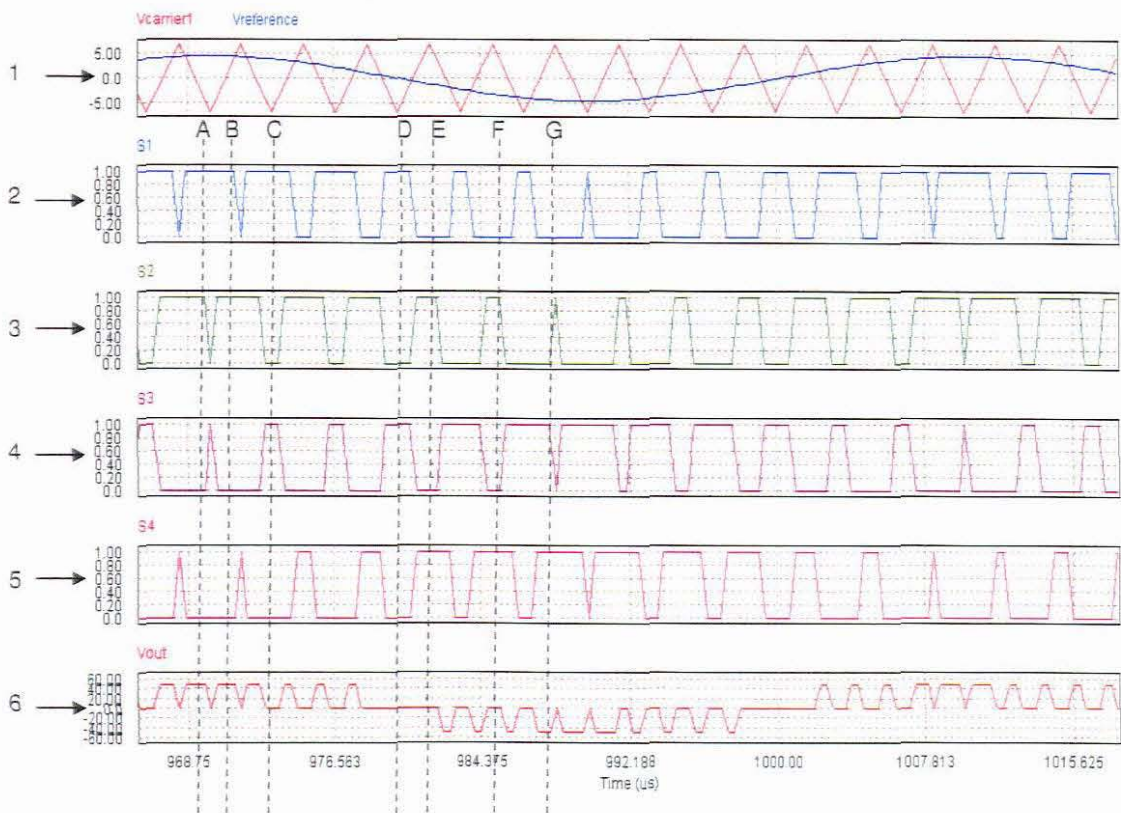


Figure 2.5: The three level multicell inverter topology

This type of converter is also known as a FCMLI inverter, but will from this point onwards be referred to as the multicell inverter topology. The magnitude of the voltage increment between two neighbouring capacitors is equal to the size of the voltage increment in the steps on the output voltage waveform. The inverter illustrated in Figure 2.5 provides a three-level voltage output ( $V_{dc}/2$ , 0 and  $-V_{dc}/2$ ; see Equation (4.10) for the values of the calculation of the cell capacitor voltage levels). For voltage level  $V_{dc}/2$ , switches  $S_1$  and  $S_2$  need to be conducting, while switches  $S_3$  and  $S_4$  need to be conducting for a voltage level of  $-V_{dc}/2$ . For a voltage level of 0 either  $S_1$  and  $S_3$  or  $S_2$  and  $S_4$  need to be conducting. The clamping capacitor is charged when  $S_1$  and  $S_3$  are conducting, but discharges when  $S_2$  and  $S_4$  are turned on.  $S_1$  and  $S_4$  and  $S_2$  and  $S_3$  switch as complementary pairs.

The conduction order of the switches in a three level multicell inverter is illustrated in Figure 2.6. The formation of the output waveform is also illustrated thereon.



**Figure 2.6: The conduction order of the switches in a 2 cell multicell inverter together with the unfiltered output waveform of the multicell inverter**

Plot 1 on Figure 2.6 illustrates the reference sinusoidal waveform that was being compared to the high frequency triangular carrier waveform. The frequency of the high frequency carrier signal is also the switching frequency of each cell. The apparent switching frequency is equal to the number of cells in the multicell inverter multiplied by the switching frequency. For explanation purposes only one carrier waveform is shown in plot 1, however, for a three level multicell inverter two carrier waveforms were required; the second carrier waveform being  $180^\circ$  out of phase with the first one. The resulting switching signals that were generated by comparing the reference signal to the two carrier signals are shown from plots 2 -5. The plots are labelled S1, S2, S3 and S4 to match up with the switches in Figure 2.5., because these respective signals are the switching signals for those individual switches in the multicell inverter. It was seen in Figure 2.6, as explained earlier, that the output waveform was built according to the combination of switches that were conducting at the same time. Reference lines A and B in Figure 2.6 shows that when S<sub>1</sub> and S<sub>2</sub> were conducting, the output was  $V_{dc}/2$  ( $V_{dc}$  being 100 V DC in this case). Reference lines C, D, E and F showed that when S<sub>1</sub> and S<sub>3</sub> or S<sub>2</sub> and S<sub>4</sub> are conducting, the output voltage level was zero. Reference line G showed that when S<sub>3</sub> and S<sub>4</sub> were conducting the output voltage became  $-V_{dc}/2$ .

The output voltage ripple is dependant on the number of cells. The output frequency of the multicell inverter is equal to the switching frequency times the number of cells of the inverter. This frequency is described as the apparent switching frequency and permits the output filter size to be reduced by a factor of  $1/p^2$  (Meynard, 1995).

Some advantages of the multicell inverter topology are as follows (Lai et al, 1996) (Kou et al, 2002):

- Switching multiplication factor will reduce switching losses;
- large number of storage capacitors provides extra ride through capabilities;
- no capacitor balancing problems if a switch might fail;
- no separate DC bus voltage sources are needed;
- good power quality;
- good electromagnetic compatibility (EMC);
- low switching losses and,
- high voltage capability.

Disadvantages of this topology are as follows (Lai et al, 1996):

- When the number of converter levels become too high, the amount of storage capacitors needed becomes excessive and,
- inverter control is complicated.

#### **2.4.2 Diode-clamped multilevel inverter**

The three-level diode clamped multilevel inverter is shown in Figure 2.6.

The output voltage ripple is dependant on the number of cells. The output frequency of the multicell inverter is equal to the switching frequency times the number of cells of the inverter. This frequency is described as the apparent switching frequency and permits the output filter size to be reduced by a factor of  $1/p^2$  (Meynard, 1995).

Some advantages of the multicell inverter topology are as follows (Lai et al, 1996) (Kou et al, 2002):

- Switching multiplication factor will reduce switching losses;
- large number of storage capacitors provides extra ride through capabilities;
- no capacitor balancing problems if a switch might fail;
- no separate DC bus voltage sources are needed;
- good power quality;
- good electromagnetic compatibility (EMC);
- low switching losses and,
- high voltage capability.

Disadvantages of this topology are as follows (Lai et al, 1996):

- When the number of converter levels become too high, the amount of storage capacitors needed becomes excessive and,
- inverter control is complicated.

#### **2.4.2 Diode-clamped multilevel inverter**

The three-level diode clamped multilevel inverter is shown in Figure 2.6.

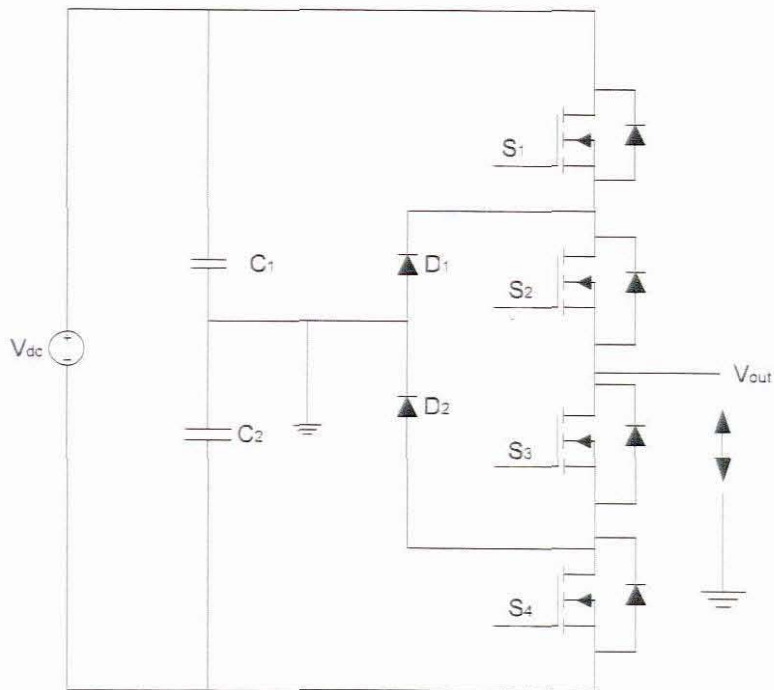


**Figure 2.7: The three-level diode-clamped multilevel inverter topology**

In this type of inverter, the DC bus voltage is split into three levels ( $V_{dc}/2$ , 0 and  $-V_{dc}/2$ ) by two series connected capacitors. As seen in Figure 2.7, the centre point of the two series connected capacitors is used as a ground reference point. To achieve the output voltage level of  $V_{dc}/2$ , switches  $S_1$  and  $S_2$  have to be conducting. To achieve an output voltage level of 0, switches  $S_2$  and  $S_3$  need to be conducting. Therefore, to achieve the output voltage level of  $-V_{dc}/2$ , switches  $S_3$  and  $S_4$  need to be conducting. The two diodes,  $D_1$  and  $D_2$ , play an important part in the balancing and sharing of the voltage across the switches. When both  $S_1$  and  $S_2$  are conducting the voltage level across  $S_3$  and  $S_4$  will be equal to  $V_{dc}$ . The voltage across  $S_2$  and  $S_3$  will be shared equally because of the balancing effect of  $D_2$ .  $S_3$  blocks the voltage across  $C_1$  and  $S_4$  blocks the voltage across  $C_2$ .

Some advantages of the diode-clamped multilevel inverter topology are as follows (Lai, 1996):

- Efficiency of the converter is high as all devices are switched at fundamental frequency;
- inverter control is simple and,
- the more levels there are, the smaller the harmonics will be and, therefore, the filters will be small.

Some disadvantages include the following (Lai, 1996):

- Number of clamping diodes is large when levels are high and,
- difficult to conduct real power flow control for the individual converter.

### 2.4.3 Cascaded multilevel inverter

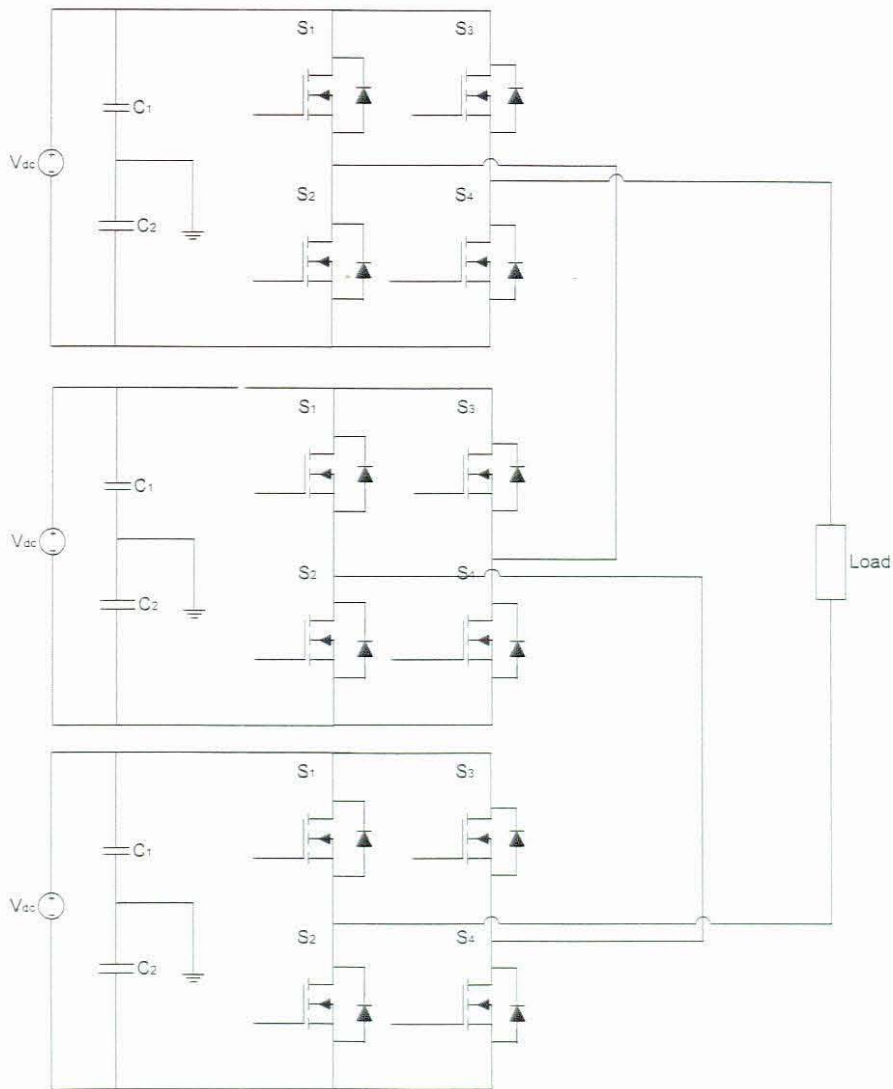


Figure 2.8: A cascaded multilevel inverter topology

A cascaded multilevel inverter (see Figure 2.8) is made up of single phase full-bridge inverters connected in series. Each individual single phase inverter has a separate DC voltage source. Each full-bridge inverter has three voltage levels ( $V_{dc}$ , 0 and  $-V_{dc}$ ). The output voltage would be the result of the addition of the individual single phase inverters' outputs. The more converters are connected in series, the closer output voltage would be to a sinusoidal waveform; the output waveform is a staircase waveform.

Advantages of a cascaded multilevel inverter include the following (Lai, 1996):

- Requires fewer switches to achieve a certain number of voltage levels than other multilevel topologies;

- soft-switching can be used to avoid the use of snubber circuits which could be inefficient and,
- easier to manufacture as a modular unit as it does not require extra clamping diodes or balancing capacitors.

Disadvantages were as follows (Lai, 1996):

- Applications were limited from a need for separate DC sources.

#### **2.4.4 The chosen topology**

After considering all topologies, the multicell inverter topology was chosen. The reasons for choosing this topology were as follows:

- No separate DC voltage sources required;
- switching multiplication factor reduced switching losses;
- low harmonic distortion level decreased the size of the output filter and,
- cell capacitors has a “balancing effect.”

Chapter 4 offers the specifications of the multicell inverter and discusses design procedure.

## **2.5 Conclusion**

This chapter dealt with plastic welding fundamentals and provided an introduction to ultrasonic plastic welding systems and their basic layouts. Applications of ultrasonic plastic welding were also discussed. A brief overview of the multicell inverter topology and how it fitted into the system was also provided.

Chapter Three discusses an ultrasonic transducer as an electrical load; an equivalent electrical model is presented for simulation purposes.



## CHAPTER THREE

### THE ULTRASONIC TRANSDUCER AS AN ELECTRICAL LOAD

Ultrasound is generally defined as sound above the human audible frequency range; typically above 20 kHz. An ultrasonic transducer is, therefore, a device which converts electrical energy into acoustic energy, or vice versa, as in the frequency range between 20 kHz and 1 MHz (Davies, 2002).

There are many varieties of ultrasonic transducer - the most popular being a piezoelectric transducer. When an electric field is applied across a piezoelectric disc, the disc's physical dimensions change and, therefore, most electrical energy is converted into mechanical energy. This is known as the piezoelectric effect. The piezoelectric effect is caused by a poling procedure in the construction of the piezoelectric material disc. The disc is heated to a temperature just below its Curie temperature – the Curie temperature for most piezoelectric ceramics lies between 160 °C and 350 °C (Janocha, 2007). At this temperature the randomly oriented dipoles' direction can be altered when an electric field is applied across the material. The electric field is then applied across the piezoelectric material in a direction according to a desired operating mode and held in that position as the material cools. When the material has cooled, the electric field can be removed, leaving the dipoles in the desired direction. W P Mason derived the electrical equivalent model for a piezoelectric disc which is named the Mason's equivalent model (see Figure 2.3) (Mason, 1935). An ultrasonic transducer consists of piezoelectric discs clamped between head and tail masses.

#### 3.1 Bolted Langevin Type (BLT) transducers

The Bolted Langevin Type (BLT) piezoelectric transducer consists of multiple piezoelectric discs separated by thin metal plates and clamped between a head and a tail mass under compression (Dukane, 2008). The transducer can be represented as a mechanical system as seen in Figure 3.1.

To explain the effect of added head and tail masses to a piezoelectric ceramic disc, the ceramic disc is represented by a spring.

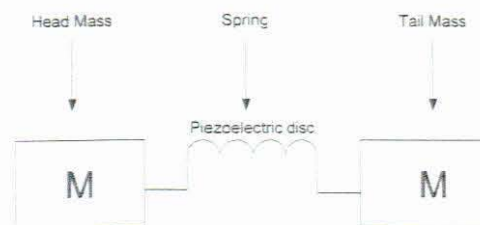


Figure 3.1: A Simplified mechanical equivalent model of a BLT transducer (Green, 1999)

When this spring is stretched and released in free space, it begins to oscillate at its natural frequency, also known as the Eigen Frequency. The factors which determine this frequency are the stiffness of the spring and, therefore, the physical construction of the spring and the masses added on either side. If the mass on either side is increased while the spring pressure is kept constant, the oscillation frequency will decrease. This is typically what happens with a BLT transducer with the addition of a booster and horn.

The relationship between the oscillation frequency and mass could be illustrated by modelling the mechanical system as an electrical system (Green, 1999).

In a BLT transducer more than one piezoelectric ceramic disc is used to handle higher power levels. Therefore, a pre-stressing bolt is used to clamp the spring for sufficient coupling. The bolt can be equated to a stiff spring placed in parallel with the entire system. The stiffer the spring and the tighter the bolt, the better the coupling between ceramic discs. At a specific tension, the ceramics couple to such an extent that they are forced to oscillate at an equivalent frequency. The bolt is used to bias the vibration and ensure the piezoelectric discs do not crack under expansion at the tuning frequency.

When the ultrasonic transducer is being driven it becomes a source of standing waves. When the length of the ultrasonic transducer is matched to the driving frequency, the device resonates mechanically and becomes a source of standing waves where the amplitude of the standing waves is at its highest. The physical output movement of a typical multiple disc BLT ultrasonic transducer at a frequency of 20 kHz and operating power of about 100 W is about 20 micron (Dukane, 2008), that could be amplified by using boosters and/or horns as is the case shown in Figure 3.2.

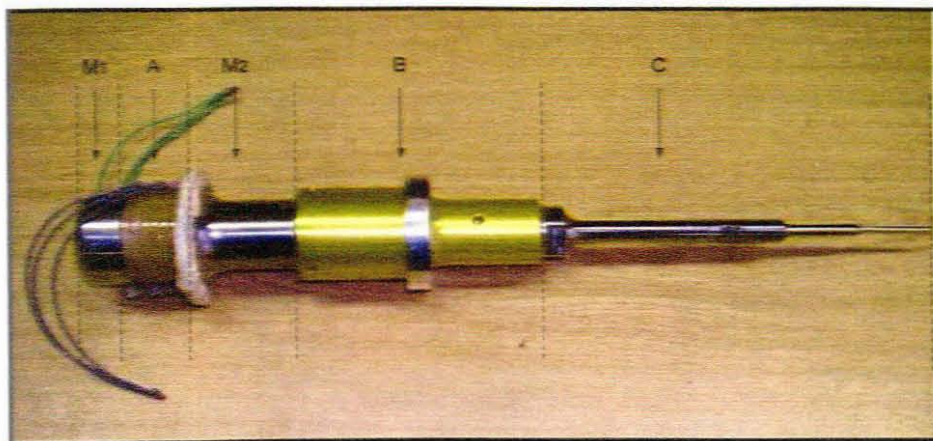


Figure 3.2: Ultrasonic transducer consisting of head mass ( $M_1$ ), piezoelectric disc stack (A) and the tail mass ( $M_2$ ). The booster (B) and stepped horn (C) combination is used with the BLT transducer for testing

The photograph (Figure 3.2) shows the head and tail masses ( $M_1$  and  $M_2$ ), the piezoelectric stack (A), the booster (B) and the stepped horn (C) - the components that make up the ultrasonic tool.

### 3.2 Characteristics of BLT transducers

BLT transducers were the preferred type of ultrasonic transducer used for ultrasonic plastic welding applications, as the physical displacement at the edge of the transducer was large compared to other types of transducers. The BLT transducer was also physically stronger because of its construction. A feature of BLT transducers is they use poreless, high density piezoelectric discs (Peric, 2004). The mechanical contact between the discs and masses are improved so that the mechanical damping is decreased. It is also mechanically extremely strong and stable (Chang, 2003).

### 3.3 Modelling a BLT transducer

An equivalent electrical model of the ultrasonic BLT transducer is required to simulate the ultrasonic load (which is comprised of mechanical components) in the inverter topology. Although there are commercially available impedance analysers that would have been able to measure the equivalent circuit parameters of an ultrasonic transducer automatically, one was not available for use in this project and these analysers are generally expensive. Therefore it was necessary to develop a quick way of measuring the equivalent circuit with the equipment available at the time of the project.

Mason developed an equivalent transmission line model for piezoelectric ceramics as shown in Figure 3.3.

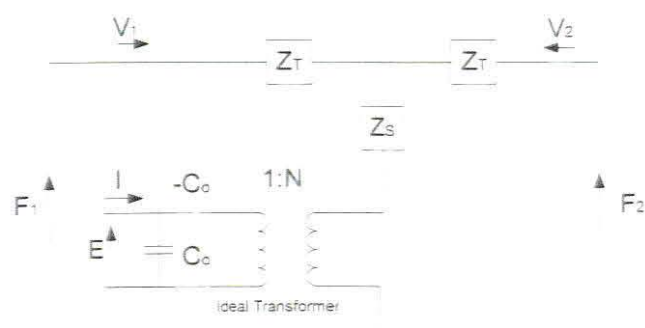
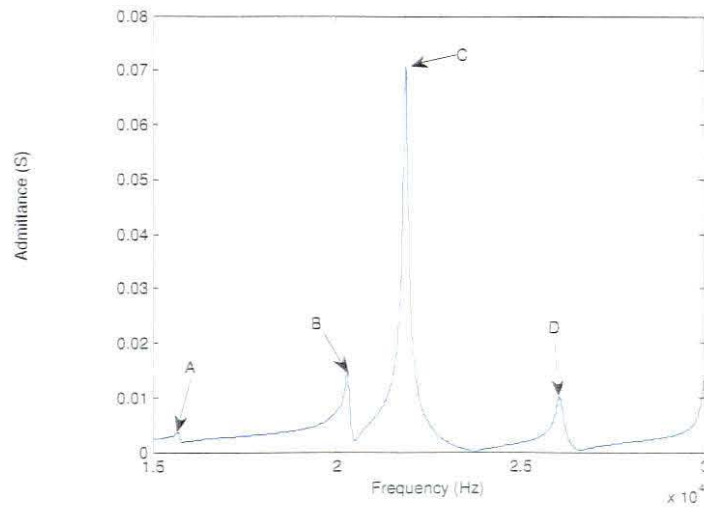


Figure 3.3: Mason's equivalent transmission line model

This model can be used to simulate all the modes of resonance of an ultrasonic transducer, as shown in Figure 3.4. It was unnecessary to use this model, as the inverter would be driven only around the main resonant mode. Therefore, a simpler solution was found.



**Figure 3.4: Admittance versus frequency plot of a transducer where C is the thickness resonant mode of the transducer and A, B and D are the radial and length modes of resonance**

The electrical equivalent circuit, often used to represent the electromechanical relationship of a piezoelectric device, is called a Butterworth Van Dyke (BVD) electrical equivalent circuit (Butterworth, 1914) (Van Dyke, 1925). Butterworth Van Dyke simplified Mason's transmission line model for a quartz resonator (see Figure 3.5). The BVD electro acoustic model was thus used to simulate the ultrasonic transducer, since only a single piezoelectric resonance was to be examined (see resonance mode C, Figure 3.4), because the transducer was driven at its resonant frequency only.

### 3.3.1 Butterworth Van Dyke (BVD) piezoelectric disc model

The BVD equivalent circuit is comprised of a RLC series resonant circuit in parallel with an electrical capacitance. The RLC circuit ( $R_m$ ,  $C_m$  and  $L_m$ ) represents the mechanical branch of the transducer and the parallel capacitance  $C_o$  represents the electrical branch (illustrated in Figure 3.5).

Sections 3.3.2 to 3.3.4 describe the methods used to determine the values of these parameters in the BVD circuit.

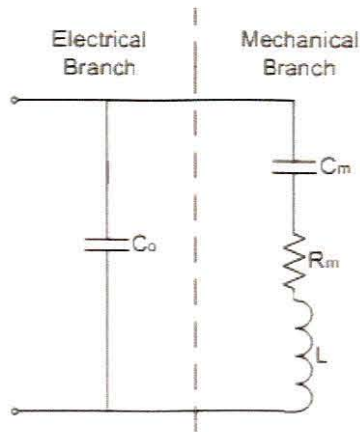


Figure 3.5: BVD equivalent circuit simplified for a single resonance mode

### 3.3.2 Electromechanical coupling factor

The first parameter to be calculated was the electromechanical coupling factor, since the only data available was the admittance versus frequency sweep that was obtained from an impedance analyser. The electromechanical coupling factor,  $k_{eff}$ , is defined as the conversion rate between the input electrical energy and the stored mechanical energy (Iula, 2002). When  $k_{eff}$  is equal to 1 it means there is 100 % energy transfer and vice versa, when  $k_{eff}$  is equal to 0.

The admittance plot displays both the mechanical and electrical resonance behaviour through the maxima and minima of the plot (Figure 3.6).

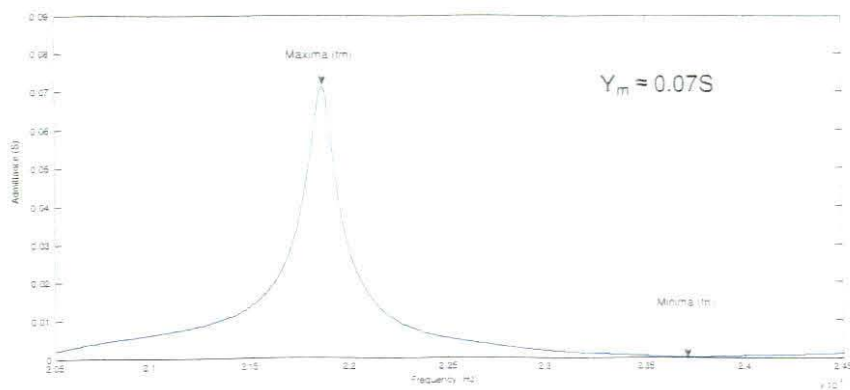


Figure 3.6: Admittance versus frequency plot pointing out the maxima and minima points of the ultrasonic transducer when loaded with PP

The magnitude plot of these maxima and minima points provided the information needed to calculate the electromechanical coupling factor,  $k_{eff}$ , of the transducer as follows (Davies, 2002):

$$k_{eff} = \sqrt{1 - \frac{f_s^2}{f_p^2}} \approx \sqrt{1 - \frac{f_m^2}{f_n^2}} \quad (3.1)$$

where

- $f_p \approx$  the parallel resonance frequency,
- $f_s \approx$  the series resonance frequency obtained from the conductance curve;
- $f_m \approx$  the maxima, representing the series resonance and,
- $f_n \approx$  the minima, representing the parallel resonances from the absolute admittance plot.

### 3.3.3 Mechanical quality factor

The quality factor  $Q_m$  can be calculated by reading the series resonance  $f_s$  and the half power point  $\Delta f_{3dB}$  from the conductance curve:

$$Q_m = \frac{f_s}{\Delta f_{3dB}} \quad (3.2)$$

or it may be approximated from the absolute admittance curve:

$$Q_m \approx \frac{\omega_m}{2(\omega_n - \omega_m)} \left[ \frac{|Y_{pn}|}{|Y_{m}|} \right] \quad (3.3)$$

### 3.3.4 Modelling the basic parameters of a piezoelectric transducer

There are four fundamental electrical parameters used for the modelling of piezoelectric transducers, namely  $R_m$ ,  $L_m$ ,  $C_m$  and  $C_o$ . These parameters define the network completely and are acceptable from which to derive other parameters. When the value of  $Q_m$  is obtained, the following parameters can be calculated (J Davies, 2002):

$$R_m = \frac{1}{|Y_{pn} - Y_{m}|} \quad (3.4)$$

$$L_m = \frac{Q_m R_m}{\omega_s} \quad (3.5)$$

$$C_m = \frac{1}{\omega_s Q_m R_m} \quad (3.6)$$

If it is impossible to measure the clamped electrical capacitance  $C_o$  using either a capacitance bridge or a Q-meter, the electromechanical coupling factor,  $k_{eff}$ , obtained from equation (3.1) could be used in the following equation:

$$C_o = C_m \left( \frac{1}{k_{eff}^2} - 1 \right) \quad (3.7)$$

### 3.3.5 Calculated equivalent circuits versus measured systems results

By using equations (3.4) to (3.7), the electrical equivalent BVD circuit was modelled to approximate the measured values of an ultrasonic transducer under various load conditions. A comparative admittance plot between the measured and the theoretical calculations are shown in Figure 3.7. The various load conditions compared are the transducer in free air (shown in Figure 3.7), the transducer loaded with high density polyethylene (HDPE) (Appendix G), the transducer loaded with polypropylene (PP) (Appendix G), the transducer loaded with polyvinylchloride (PVC) (Appendix G) and the transducer loaded with Perspex (Appendix G).

The theoretical values for the models were generated from the Matlab source code shown in Appendix F. The values for the parameters  $f_m$ ,  $f_n$ ,  $Y_m$  and  $Y_n$  were obtained from the measured admittance versus frequency plots of the transducer in the various load conditions as illustrated in Figure 3.6. The actual values used for these parameters are shown in Appendix C.

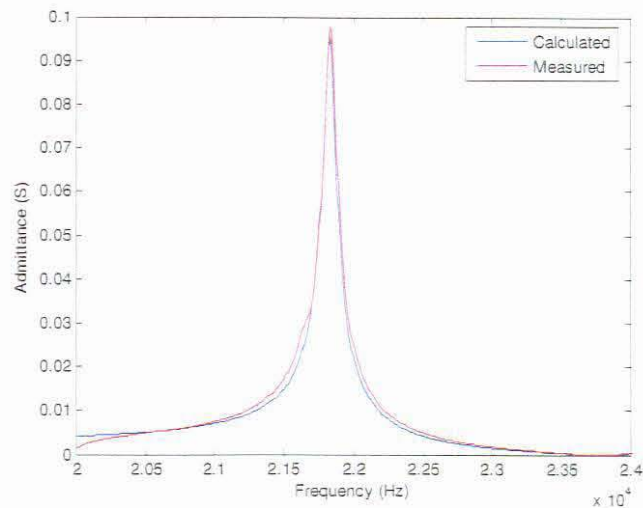


Figure 3.7: A comparison between the measured admittance values versus frequency and the calculated values with the aid of a BVD model of a BLT transducer with a horn and booster in free air. The calculated theoretical circuit parameters are as follows:  $C_o = 12.6 \text{ nF}$ ,  $L_m = 0.023 \text{ H}$ ,  $R_m = 10.31 \text{ } \Omega$  and  $C_m = 2.31 \text{ nF}$

### 3.4 Conclusions

The ultrasonic transducer as an electrical load was discussed in order to understand the complications and difficulties associated with driving such devices. The basic ultrasonic theory, the BLT transducer and the characteristics of such a transducer were explained.

To understand the dynamic behaviour of the ultrasonic transducer under different load conditions, a bar chart representation of the change in the equivalent circuit parameters when loaded with various plastic samples, is provided as Figure 3.8.

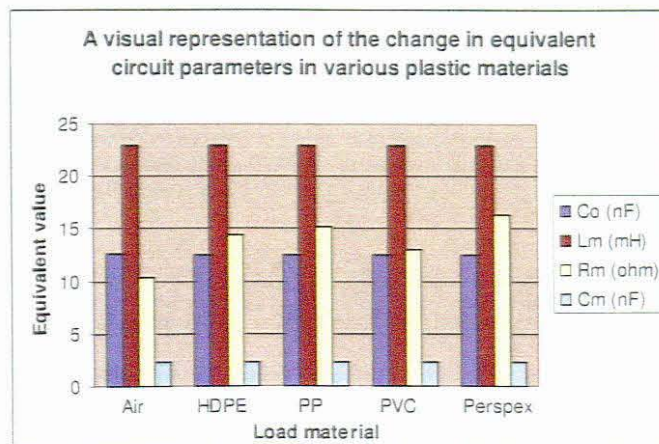


Figure 3.8: Comparison of the equivalent circuit parameters calculated from the measured admittance versus frequency scans



Note the values of  $C_o$ ,  $L_m$  and  $C_m$  remains constant for all practical purposes; however, the value for  $R_m$  changes significantly under various load materials.

The accuracy of the BVD equivalent circuit results are illustrated through the admittance versus frequency plots from the BVD equivalent circuit against the original admittance versus frequency scan. Figure 3.7 (also see Appendix G) shows that the calculated BVD equivalent circuit correlates closely with the actual transducer in the frequency versus admittance scans.

The susceptance versus the conductance plot, better known as an admittance circle, was drawn of the measured versus the calculated BVD equivalent circuit parameters (see Figure 3.10). All information from the transducer was derived from the admittance circle, as illustrated in Figure 3.9. Vector diagrams were used to derive values for  $C_o$ ,  $f_m$ ,  $f_n$ ,  $f_s$  and  $f_p$ . An admittance circle gives an overall understanding of a particular transducer's resonance behaviour.

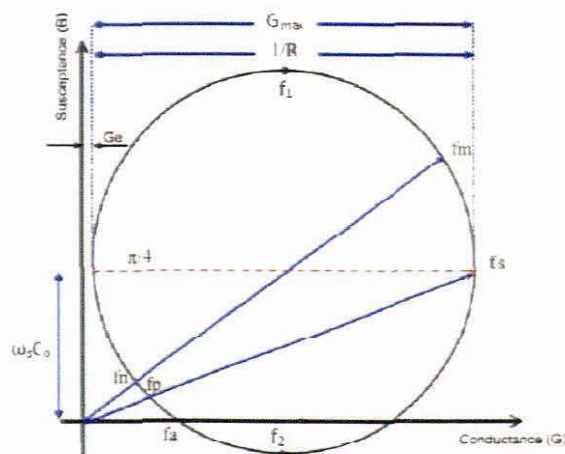


**Figure 3.9: The admittance vector diagram for a piezoelectric vibrator. Maximum and minimum admittances are represented by  $f_m$  and  $f_n$  in the diagram. The series and parallel mechanical resonances,  $f_s$  and  $f_p$  respectively, are also shown on diagram together with  $R$  and  $G_e$  which represents the mechanical damping of the resonance and the dielectric loss conductance respectively. The half power points (-3dB) are marked as  $f_1$  and  $f_2$  (Stansfield, 1990)**

Result of comparison between simulated and measured admittance circles of the ultrasonic transducer is shown in Figure 3.10. The vertical offset of the admittance circle in the susceptance axis was because of the clamped capacitance  $C_o$ . The circle illustrates the single piezoelectric mode and has a diameter of  $1/R$  which could be measured by the absolute admittance difference. The additional smaller admittance circle represents a superimposed resonance.

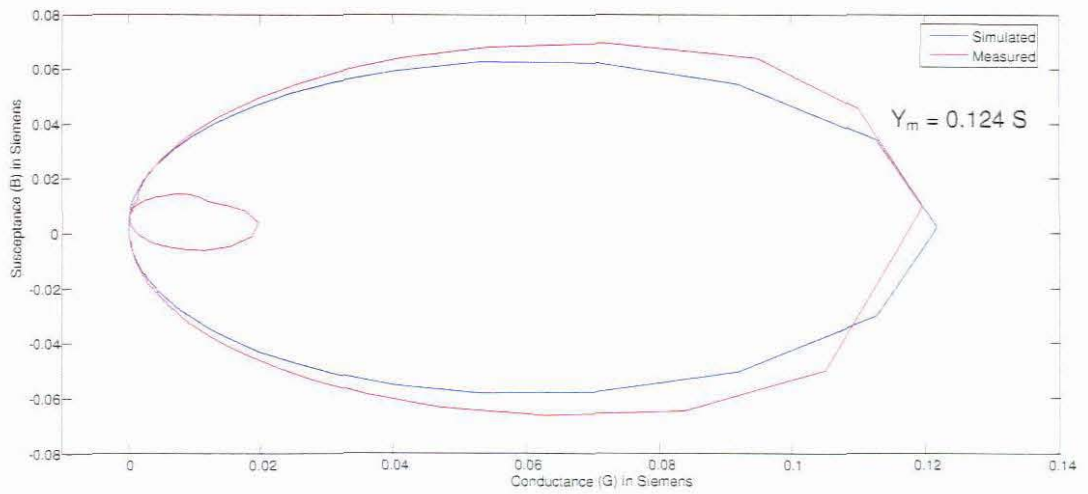


**Figure 3.10: The simulated versus the measured admittance circles of an ultrasonic transducer in free air**

The measured and calculated admittance circles did not correlate perfectly; however, the information illustrated in Figure 3.9 could still be derived from the plot.

It was, therefore, evident from the simulated results that the BVD model was adequate for the simulation of the ultrasonic transducer at its main resonant frequency.

## CHAPTER FOUR THE SELECTION AND DESIGN OF AN ULTRASONIC INVERTER

The ultrasonic transducer needed to be excited with a sinusoidal AC driving voltage.

An ultrasonic transducer has various mechanical modes of operation as seen in Figure 4.1.

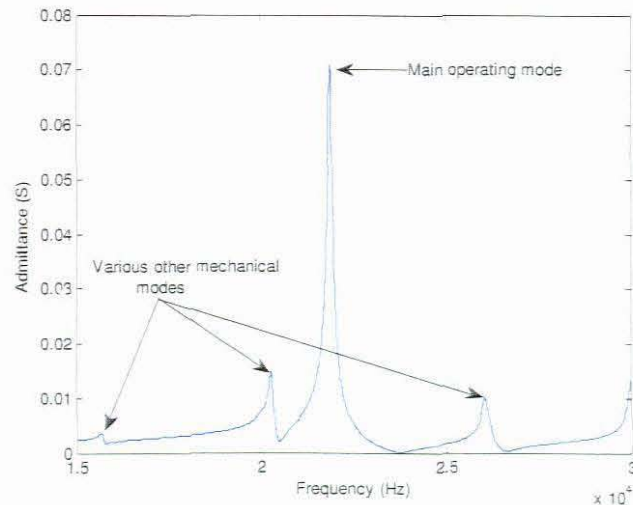


**Figure 4.1: Various mechanical modes of an ultrasonic transducer shown with the main operating mode of the transducer**

When an ultrasonic transducer is driven off its main resonance mode, unwanted mechanical resonances of the ultrasonic transducer can be excited that could cause physical damage to the device (Green, 1999). Therefore, an ultrasonic transducer cannot be driven with only a square wave, because of the wave's harmonics (Kaiser, 2004)(Bracewell, 1963). This is because a square wave consists of a theoretical infinite number of sinusoidal waves (Kaiser, 2004) (Bracewell, 1963). It is, therefore, essential to operate the transducer with a driving voltage which is as close as possible to a sinusoidal driving voltage.

The power supply should be small and economic because of a need for a low-cost portable ultrasonic plastic welder. An overview of the various multilevel inverter topologies was discussed in Chapter Two. The reason for choosing the multicell inverter topology was also discussed.

The next section discusses the design procedure of the multicell inverter.

## 4.1 Design of the multicell inverter

The theoretical design methodology is presented in the following sections.

### 4.1.1 Introduction

The multicell inverter uses a ladder structure of capacitors where the voltage level of each differed from the next. The voltage difference between two adjacent capacitors was equal to the voltage step size in the output voltage waveform of the inverter.

An interleaved switching scheme was used in the multicell inverter to optimise the output voltage waveform in respect of the reference sinusoidal waveform. Interleaving control signals resulted in an apparent switching frequency equal to  $p$  times the switching frequency (switching frequency was the rate at which a DC voltage was switched in order to produce an AC voltage). This apparent switching frequency created switching harmonics at a higher frequency than the inverter's output voltage waveform, resulting in the use of a much smaller output filter than normally required; in turn reducing the overall weight and size of the system.

The multicell inverter topology solved the problem of the static and the dynamic voltage sharing of the voltage across the blocking switches (Molepo, 2003). In this type of converter voltage stress on all blocking switches is identical; voltage stress over a blocking switch is equal to the voltage difference between neighbouring capacitors.

### 4.1.2 Design specifications

Design specifications were defined from the transducer type (as discussed in Chapter Three) and research undertaken on the operating ranges of commercially available ultrasonic plastic welders. The design specifications set for the ultrasonic inverter are listed in Table 4.1.

Table 4.1: Design Specifications of an ultrasonic inverter

Parameter	Symbol	Value	Unit
Input voltage	$V_d$	100	$V_{dc}$
Output voltage	$V_o$	100	$V_{p-p}$
Output frequency	$f_o$	25	kHz
Switching frequency	$f_s$	300	kHz
Maximum output current	$I_o$	10	A

The input voltage was chosen as 100 V DC to generate a 50 V AC driving voltage on the output of the inverter. The output frequency of the inverter was specified as 25 kHz as an upper limit for the output driving voltage, because of the ultrasonic transducer's resonant frequency in the region of 21 kHz (depending on the load condition). A switching frequency of 300 kHz was chosen in order to produce an apparent switching frequency of 900 kHz, which was high enough to reduce the harmonic distortion on the output voltage of the inverter. A rule of thumb is to have the switching frequency of the MOSFETs at least 10 times greater than the output frequency of the inverter in order to reduce the chance of switching harmonics overlapping. This in turn reduces the size of the output filter of the inverter. The factor by which the high apparent switching frequency reduces the filter size is  $p^2$  (Meynard, 1995), where  $p$  is the number of commutation cells in the multicell inverter.

During operation the ultrasonic plastic welding tool drew more or less 1.5 A<sub>p-p</sub>. The maximum output current was specified as 10 A to provide a safety margin and also flexibility to use other ultrasonic transducer types in future which might draw more current.

#### 4.1.3 Design of the flying capacitors

The design methodology for the reactive components of a multicell inverter was proposed by Hamma et al (Hamma et al, 1995). To design the capacitor  $C_k$  it was necessary to determine characteristics of the ripple voltage and the current flowing in this capacitor. For design purposes the ripple current in the smoothing inductor was neglected. The current in the smoothing inductor was assumed constant, although in reality it varied with respect to time.

Because the natural stability of the voltage distribution (Hamma et al, 1995) a maximum voltage of 33.3 V was applied across each blocking switch. These capacitors guaranteed the maximum voltage per switch would not exceed  $E/P$ ; this voltage was damped by the use of flying capacitors.

It is worth noting that the state of the other elementary cells had no influence on the current and voltage applied to the switches of a given cell. The shape of the current  $i_{ck}$  was dependent only on the state of the two switches,  $Sk_{t+i}$  and  $Sk_t$  and the instantaneous current ( $i_{ck}$ ) in the capacitor  $C_k$  could have only three values (Hamma et al, 1995) as:

- $i_{ck} = I_o$ , when  $Sk_{t+i}$  is on and  $Sk_t$  is off;
- $i_{ck} = 0$ , when  $Sk_{t+i}$  and  $Sk_t$  are in the same state and,
- $i_{ck} = -I_o$ , when  $Sk_{t+i}$  is off and  $Sk_t$  is on.

where  $I_o$  is the average value of the current in the inductor,  $i_l$  (Hamma et al, 1995) as illustrated in Figure 4.2.

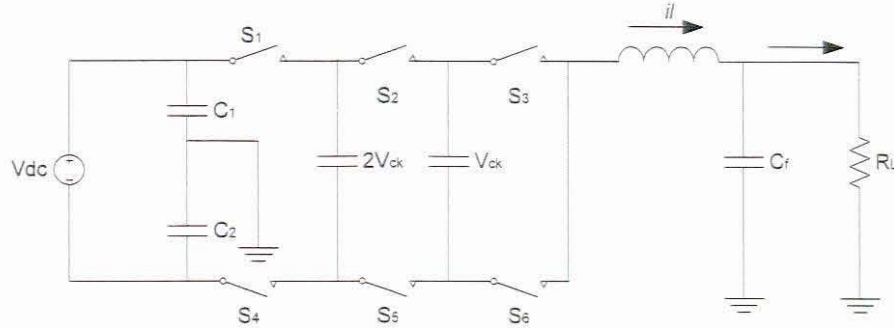


**Figure 4.2: Diagram of the multicell inverter with the inductor currents used for designing the flying capacitors**

The three operating modes were derived from the value of the duty cycle  $D$  and the phase difference between the triangular carrier signals ( $\phi$ ). The following analysis is for a DC – AC inverter and valid for any number of cells where  $p \neq 1$  ( $p$  represents the number of cells):

1. When  $0 \leq D \leq T_s \phi / 2\pi$ , the charge and the discharge time of the current  $I_{ck}$  in the capacitor  $C_k$  is equal to  $DT_s$ . The RMS current is given by the following equation (Hamma et al, 1995):

$$I_{ck_{rms}} = I_o \cdot \sqrt{2 \cdot D} \quad (4.1)$$

When equation (4.1) is normalised with respect to  $I_o$  it gives:

$$\frac{I_{ck_{rms}}}{I_o} = \sqrt{2 \cdot D} \quad (4.2)$$

where  $I_o$ ,  $I_{ck_{rms}}$  and  $D$  are the load current, the RMS current flowing in the capacitor and duty cycle respectively.

The normalised voltage ripple is given by:

$$\frac{C_k \Delta V_{ck}}{T_s I_o} = D \quad (4.3)$$

F. Hamma *et al.* illustrated that a plot of the characteristics of equation (4.2) and equation (4.8), i.e.  $I_{ck(rms)}/I_o$  and  $C_k\Delta V_{ck}/T_s I_o$  versus duty cycle with phase-shift ( $\phi$ ) as a parameter, are symmetrical with respect to the  $D = 1/2$  axis (Hamma et al, 1995).

The capacitor value  $C_k$  can be determined from equation (4.6). It must be noted the capacitor  $C_k$  should be able to withstand cell voltage equal to  $kV_o/p$ . Flying capacitors enjoy the same capacitance values, but their voltage ratings differ.

Using the known values of the maximum ripple voltage  $\Delta V_{ck(max)}$ , the load current  $I_o$  for a given value of phase-shift, the switching frequency  $f_s$ , the size of a capacitor had to satisfy the following limit which is derived from equation (4.6):

$$C_k \geq \frac{\phi I_o}{2\pi \Delta V_{ck} f_s} \quad (4.9)$$

When a current flows through the capacitors it causes a voltage ripple. The maximum voltage ripple was assumed to be 5% of the DC bus voltage, therefore, the maximum voltage ripple was assumed to be 5V.

With the voltage ripple (5 V), switching frequency (300 kHz), phase-shift between cells ( $2\pi/p$ ) and the RMS output current (7.071 A<sub>RMS</sub>) all known, the capacitance of  $C_k$  is calculated to be greater than or equal to 1.571  $\mu$ F.

The two flying capacitor voltage ratings are calculated using the following equation (Hamma et al, 1995):

$$V_{ck} = \frac{k \cdot E}{p} \quad (4.10)$$

Where E is the input DC voltage and p is the number of cells and  $k=1, 2, \dots, p-1$

Therefore, the voltage ratings of the flying capacitors  $V_{c1}$  and  $V_{c2}$  are 66.6 V and 33.3 V respectively. As the calculated value is not standard, any larger value could have been chosen. A voltage rating of at least 100V was sufficient for the flying capacitors, which resulted in a safety margin of at least 33 V. The flying capacitors that were used in the multicell inverter had a capacitance of 2.5  $\mu$ F and had a voltage rating of 1000  $V_{dc}$ .

#### 4.1.4 Design of the DC bus capacitors

The selection of the two DC bus capacitors was determined essentially by the ripple current. The cost of the components also played a role in the selection. A figure of the ripple current in the DC bus capacitors is shown as:

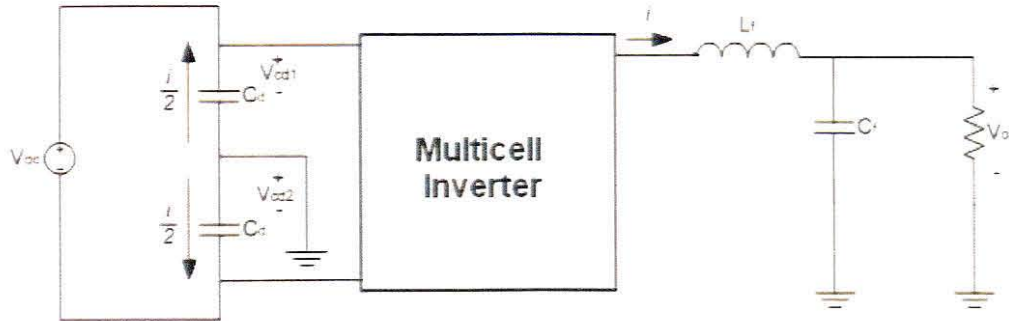


Figure 4.3: Ripple current in the DC bus capacitors in the multicell inverter

The voltages and currents shown and named in Figure 4.3 are used in the derivation of the DC bus capacitor calculations.

The high-frequency component of the ripple current is ignored in the calculation of the DC bus capacitance. The current that is flowing in the filter inductor is given by the formula:

$$i = 10 \sin \omega t \quad (4.11)$$

Where 10 A is the peak output current, which was chosen in the design specifications.

The current flowing through the bottom capacitor to ground is, therefore, given by the following equation:

$$\frac{i}{2} = C_d \frac{dV_{dc}}{dt} \quad (4.12)$$

Substituting (4.11) into (4.12) gives:

$$\begin{aligned} 5 \sin \omega t &= C_d \frac{dV_{dc}}{dt} \\ dV_{dc} &= 5C_d \sin \omega t dt \end{aligned} \quad (4.13)$$



$$V_{dc} = \frac{-5}{C_d \omega} \cos \omega t + \frac{V_d}{2} \quad (4.14)$$

where  $\omega$  is the fundamental angular frequency equal to  $2\pi 50$  rad/s.

It was assumed there was a voltage ripple of 5% on the DC bus with a voltage of 100V. The expression for the maximum allowable voltage ripple on the DC bus is given by:

$$V_{\max} = \frac{5}{C_d \omega} = 5 \text{ V} \quad (4.15)$$

From equation (4.15) the DC bus capacitance is calculated as:

$$C_d = \frac{5}{(314.159)(5)} = 3183 \text{ } \mu\text{F}$$

The capacitance value of each of the two DC bus capacitors had to be a standard value as close as possible to the calculated value. Therefore, in this design a standard value of 3300  $\mu\text{F}$  was chosen. The voltage rating of the capacitors had to be at least 50 V.

#### 4.1.5 Design of the bleeding resistors

The role of the bleeding resistor in the multicell inverter was the resistor discharged a high voltage DC bus when the inverter was switched off in a no-load condition. The bleed resistors were connected across the DC bus capacitors; this ensured a quick discharge of capacitors when the power supply was switched off. It also minimised the chance of electric shock.

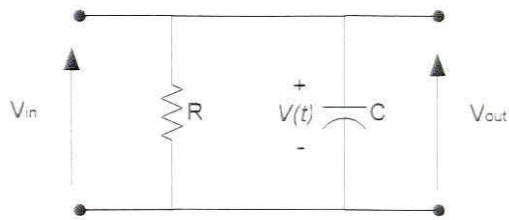


Figure 4.4: A parallel RC circuit

Figure 4.4 shows a simple parallel RC circuit with the appropriate labelling referred to in the calculations of the bleeding resistors.

From the step response of an RC circuit the voltage across the discharging capacitor (as seen in Figure 4.4) is given by:

$$v(t) = V_o e^{-\frac{t}{RC}} \quad (4.16)$$

which gives:

$$t = -RC \ln\left(\frac{v(t)}{V_o}\right) \quad (4.17)$$

The power dissipated in the resistor is equal to:

$$P = \frac{V^2}{R} \quad (4.18)$$

In order to discharge the 3300  $\mu\text{F}$  capacitors with an initial voltage of 50 V to a voltage of 2 V, a resistor of 8.2 k $\Omega$  will take (4.17):

$$\begin{aligned} t &= -(8200)(3183\mu) \ln\left(\frac{2}{50}\right) \\ &= 23.91 \text{ seconds} \end{aligned}$$

With a bleeding resistor, the DC bus took 23.91 seconds to discharge to 2 V.

It was calculated the 8.2 k $\Omega$  resistor would take 23.91 seconds to discharge the 3300  $\mu\text{F}$  capacitors. This meant determining the power rating of the resistors was more than the power dissipated in the resistor which was calculated by (4.18):

$$P = \frac{V^2}{R}$$

$$\begin{aligned}
 &= \frac{50^2}{8200} \\
 &= 304.878 \text{ mW}
 \end{aligned}$$

Therefore, a  $\frac{1}{2}$  Watt, 8.2k  $\Omega$  resistor has placed across each DC capacitor.

#### 4.1.6 Design of the output filter

To obtain the desired sinusoidal waveform from the inverter, an output filter had to be designed. In this case a second order low-pass filter was created, because it had the ability to attenuate the higher frequencies more steeply. The filter was comprised of an inductor in series and a capacitor in parallel with the load (as seen in Figure 4.5).

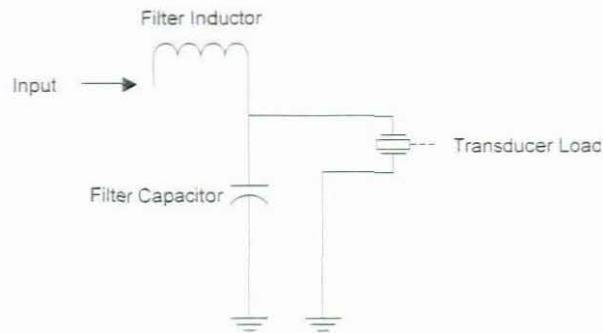


Figure 4.5: A second order low-pass LC filter

Equations for the second order low-pass filter used are shown (Killen et al, 1985; Boylstadt et.al, 1994).

$$L_f = \frac{Z_o}{\pi f_c} \quad (4.19)$$

where:  $L_f$  represents the filter inductor  
 $Z_o$  represents the output Impedance  
 $f_c$  represents the cut-off frequency

The output impedance  $Z_o$  was taken as 10  $\Omega$  and the cut-off frequency  $f_c$  was taken as 25 kHz. The calculated value for the filter inductor  $L_f$  was 127.3  $\mu\text{H}$ .

$$C_f = \frac{1}{\pi f_c Z_o} \quad (4.20)$$

where:  $C_f$  represents the filter capacitor  
 $Z_o$  represents the output Impedance

$f_c$  represents the cut-off frequency

Using the same values for the cut-off frequency  $f_c$  and the output impedance  $Z_o$  that were used for the filter inductor calculation, the filter capacitor  $C_f$  was calculated to be  $1.3 \mu\text{F}$ .

Figures 4.6 and 4.7 show the measured impedance versus frequency and the phase versus frequency plots of the constructed low-pass filter respectively.

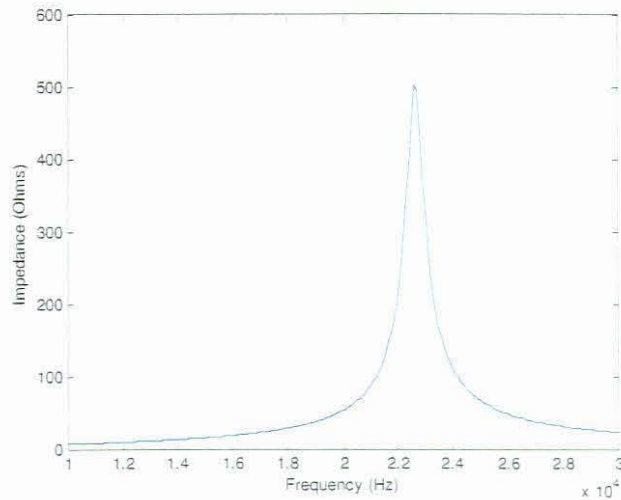


Figure 4.6: Impedance versus frequency plot of the physically constructed filter measured with the HP 4192A impedance analyser

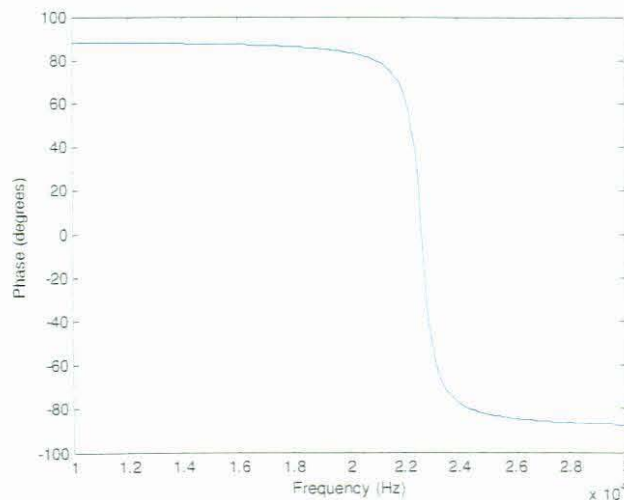


Figure 4.7: Phase versus frequency plot of the physically constructed filter measured with the HP 4192A impedance analyser

#### 4.1.7 Component selection

The section explains the considerations that were taken for the physical components used in the design and construction of the multicell inverter.

The MOSFET drivers used in each switch were ICL 7667 drivers from Intersil Corporation. The ICL 7667 was a dual high speed driver that was capable of producing switching signals of up to 15 V. The input voltage required ranged from 4.5 to 15 V DC. The output resistance was 7  $\Omega$  while the device had a low power consumption of 20 mW. The device was TTL compatible which was important because of the TTL switching levels that were supplied from the power electronic modulator.

The MOSFETs used in this project were IRF 520 devices. It was an N-channel power MOSFET that had a current rating of 9.2A and a voltage rating of 100V. The drain-to-source on-state resistance of the device was 0.270  $\Omega$ .

The flying capacitors had values of 2.5  $\mu$ F per device and 1000 V DC voltage rating. The tolerance of the capacitor were  $\pm 5\%$ .

The schematic diagrams illustrating the components and the component values used to construct the physical multicell inverter are shown in Figures D3 and D4. Figure D3 shows the schematic diagram of the high side switch of a single cell, while Figure D4 illustrates the schematic diagram of the low side switch of a single cell in the multicell inverter.

#### 4.2 Heat sink design notes

Semiconductor switching devices have power losses which are dissipated in the form of heat, derived from the switching junction. The reliability and life expectancy of a power semiconductor device is directly associated with the maximum junction temperature experienced by the device.

In the process of choosing a suitable heat sink, the maximum allowable junction temperature the device could tolerate had to be considered. In calculating a heat sink with absolute minimum specifications (no safety margin), the maximum junction temperature, maximum power dissipation (sum of the switching power loss and conduction loss) and the maximum ambient temperature of the device were used.

#### 4.2.1 Conduction and switching power losses

Similar to that of a half-bridge inverter, the cell of a multicell inverter is controlled in a complementary method so that only one switch conducts at a time. Therefore, the power loss based on the behaviour of one of the switches was calculated.

Conduction losses occurred only when the devices were switched on and began conducting. The on-time ( $t_{on}$ ) was determined by the duty-cycle ( $D$ ) of the switches, which was again determined by the modulation index ( $m_a$ ) of the reference signal. The modulation index ( $m_a$ ) of the reference signal is given by:

$$m_a = \frac{2\hat{V}_o}{V_{d(\min)}} \quad (4.21)$$

Where  $\hat{V}_o$  is the peak output voltage and  $V_{d(\min)}$  is the minimum input voltage.

The maximum duty cycle ( $D_T$ ) of the top switch is given as:

$$D_T = 1 - D_B \quad (4.22)$$

$$D_T = \frac{1}{2}(1 + m_a \sin(\omega t))$$

The bottom switch was turned on when the carrier waveform was greater than the reference waveform. Therefore, the duty cycle of the bottom switch ( $D_B$ ) was given by:

$$D_B T_S = \frac{T_S}{2}[1 - m_a \sin(\omega t)] \quad (4.23)$$

$$D_B = \frac{1}{2}[1 - m_a \sin(\omega t)]$$

The power loss in a metal oxide semiconductor field effect transistor (MOSFET) device is a function of the current flowing through it and the resistance of the device in its on state. When the top switch is on, the current flowing through the device is equal to the current flowing in the filter inductor. If a unity power factor is assumed (a power factor of 1 means the load is purely resistive) and the ripple current ignored, the current in the inductor is given by:

$$i_l = B \sin(\omega t) \quad (4.24)$$

where  $\omega = 2\pi f_o$  and  $B = I_o \sqrt{2} = 14.142 \text{ A}$

The on state resistance ( $R_{DS(ON)}$ ) is obtained from the manufacturer's data sheet. The conduction and switching losses for a MOSFET is dependant only on the device's on state resistance and the switching frequency (switching time).

**Table 4.2: MOSFET data used for conduction and switching power losses**

Parameters	Symbol	Maximum value
Drain - to -source on-state resistance	$R_{DS(ON)}$	0.0105 $\Omega$
Turn-on time	$t_{ON}(s)$	25 ns
Turn-off time	$t_{OFF}(s)$	85 ns
Forward voltage	$V_F(V)$	1.5 V
Forward current	$I_F = I_{RMS} (A)$	7.071A
Peak reverse recovery current	$I_{rr} (A)$	7A
Reverse recovery time	$t_{rr}(s)$	140 ns
Junction to case thermal resistance	$R_{th(j-c)}$	0.6 $^{\circ}C/W$
Case to sink thermal resistance	$R_{th(c-s)}$	0.5 $^{\circ}C/W$
Junction to ambient thermal resistance	$R_{th(j-a)}$	40 $^{\circ}C/W$
Maximum junction temperature	$T_j$	150 $^{\circ}C$
Maximum ambient temperature	$T_a$	25 $^{\circ}C$

The **conduction losses** in the switching devices are calculated in the next subsection.

The conduction energy dissipated in the top device during one switching cycle is given by (Molepo, 2003):

$$E_{t(cond)} = \frac{1}{2} V_{ON} (1 + m_a \sin(\omega t_1)) (B \sin(\omega t_1)) T_s \quad (4.25)$$

The average conduction losses dissipated in a switch are given by:

$$P_{cond} = R_{DS(ON)} I_{RMS}^2 D \quad (4.26)$$

Where  $R_{DS(ON)}$  is the on state resistance,  $D$  is the duty-cycle and  $I_{RMS}$  is the RMS current flowing in the MOSFET switch.

The switching losses in the devices are calculated as:

The switching power losses of a MOSFET switch over a fundamental period is given by (Molepo, S.A.2003):

$$P_{switching} = \frac{f_s}{2\pi} V_{cell} m_b (t_{ON} + t_{OFF}) \quad (4.27)$$

The reverse recovery losses in the antiparallel diodes were also calculated.

A diode requires time to switch from conducting the forward current ( $I_f$ ) to blocking it. This time is referred to as reverse recovery time ( $t_{rr}$ ). The turn-off energy of the diode during a switching cycle is given by:

$$E_{rr} = I_{rr} V_{cell} D \frac{t_{rr}}{2} \quad (4.28)$$

Where  $I_{rr}$  is the reverse recovery current,  $t_{rr}$  is the reverse recovery time,  $V_{cell}$  is the voltage across the diode at recovery and  $D$  is the duty cycle.

The power loss of one fundamental cycle is given by (Powerex application note, 2007):

$$P_{rr} = 0.125 I_{rr} t_{rr} V_{cell} f_s \quad (4.29)$$

The next step was to calculate the heat sink value.

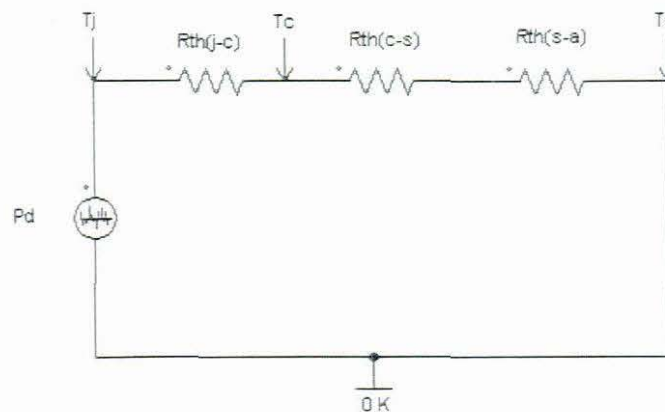


Figure 4.8: A thermal representation of the system

Transmission of heat from the semiconductor devices through the heat sink to the ambient occurred in the following order, as shown in Figure 4.8.

- Transfer from the heat source to the surface of the device case;
- transfer from the device's case surface to the surface of the heat sink and,



- transfer from the heat sink to surrounding air, by means of free or forced convection.

The thermal resistance values sought for the heat sink design were obtained from the manufacturer's data sheet. Thermal resistance was defined as the ratio of temperature to power (degree of temperature increase resulted from an input power).

The junction-to-case temperature ( $T_{j-c}$ ) is given by:

$$T_{j-c} = R_{th(j-c)} \times [P_{cond} + P_{switching}] \quad (4.30)$$

Where  $R_{th(j-c)}$  is the junction-to-case thermal resistance and  $P_{cond}$  and  $P_{switching}$  is the conduction and switching power losses respectively as calculated before.

The junction-to-case temperature  $T_{j-c(max)}$  is used to calculate the maximum allowable case temperature  $T_c$ , which is given by:

$$T_c = T_j - T_{j-c(max)} \quad (4.31)$$

Where  $T_j$  is the junction temperature.

The maximum allowable heat sink temperature ( $T_s$ ) is given by:

$$T_s = T_c - [R_{th(c-s)} (P_{ST(loss)})] \quad (4.32)$$

Where  $P_{ST(loss)}$  is the total loss per switch.

The sink-to-ambient thermal resistance ( $R_{th(s-a)}$ ) determines the size and type of the heat sink to be used to provide sufficient cooling and prevention of overheating of devices.

$$R_{th(s-a)} = \frac{T_s - T_a}{P_{Tl}} \quad (4.33)$$

where  $P_{Tl}$  is the total power loss per inverter.

Table 4.3: Calculated answers for the heat sink design

Parameter	Calculated answer (Unit)
$P_{cond}$	0.525 W
$P_{switching}$	2.451 W
$P_{rr}$	1.224 W
$P_T$	4.2 W
$T_{j-c}$	1.786 °C
$m_a$	0.9
$B$	14.142 V
$T_c$	148.214 °C
$T_s$	145.909 °C
$R_{th(s-a)}$	28.788 °C/W

Figure 4.9 gives a visual representation of the main contributing power loss types as discussed and the calculations given in Section (4.2.1).

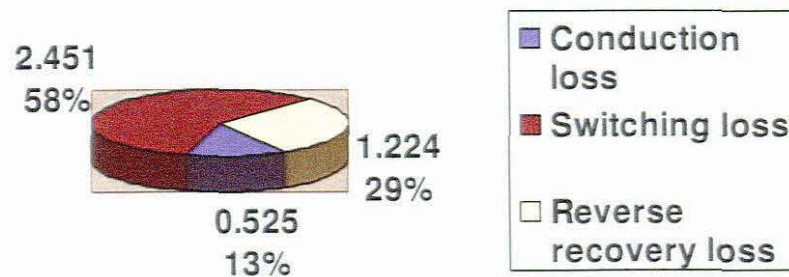


Figure 4.9: A visual representation of the main contributing power loss types in the system

The value of  $R_{th(s-a)}$  allows for no safety margin, therefore, the value had to be reduced by at least 30% to permit for a 30% safety margin.

#### 4.2.2 PCB heat sink

When designing a PCB using power switching devices such as MOSFETs, an effective heat sink should be used to dissipate excess heat generated within the system. As surface

mounted MOSFETs were used in this design, a conduction pad area on the PCB was designed to ensure sufficient cooling. Figure 4.10, from Mircell Technologies (Bob Wolbert, 2008), shows the required PCB pad area for efficient dissipation of heat.

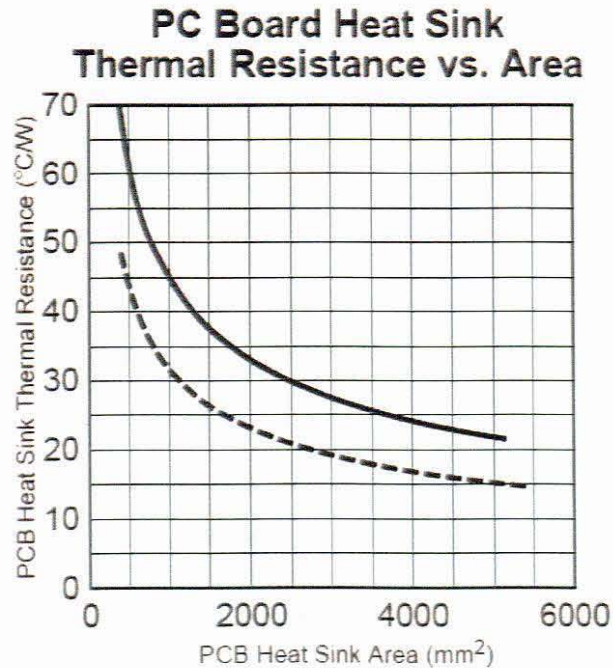


Figure 4.10: The graph shows the PCB Heat Sink Area required for the calculated thermal resistance of the system (Bob Wolbert, 2006)

The solid line represents the area of a square, horizontal, single-sided, solder masked, copper PCB trace heat sink. No airflow is assumed. The broken line represents a heat sink covered in black oil-based paint with airflow of 1.3 m/seconds.

#### 4.3 Fibre optic isolation

To electrically isolate the inverter from the digital controller, all gate driving and feedback signals were sent and received through fibre optic transmitters and receivers respectively. The type of fibre optic cable used was a simplex fibre optic cable. It was constructed of a single index plastic core sheathed in a plastic jacket.

The transmitters used in the project were Agilent HFBR 2521, the receivers Agilent HFBR 1521. To be able to transmit data via fibre optic, a driver interface IC was used. The IC used was the Fairchild SN 75451 open collector driver. The emitter of the transistor in the driver chip is internally connected to ground, while the collector was unconnected. The advantage of the open collector driver was that a pull-up resistor could have been added to the open collector of the driver, making it possible to drive devices with a higher voltage requirement.

The schematic diagrams of how the fibre optic interface drivers were connected to each cell of the multicell inverter were shown in Figure D3 and D4 in Appendix D.

#### 4.4 Auxiliary power supply

An auxiliary power supply was needed to provide the required DC voltage levels to the control circuits and drivers of the inverter system. There were two problems to be investigated. The first was each switch's driver and control power supply had to be electrically isolated from each another. Another problem was the auxiliary power supply had to be powered from the same supply as the inverter, rather than an external power supply. The solutions to these problems are explained in this section. Therefore an auxiliary power supply consisting of six floating supplies was needed to be custom designed for the multicell inverter. It was not possible to use commercially available power supplies, because the cost of the project had to be kept to a minimum.

##### 4.4.1 Auxiliary power supply specifications

The required specifications of the auxiliary power supply are given in Table 4.4.

Table 4.4: Specifications of the auxiliary power supply

Parameter	Value	Unit
Power Rating	30	W
Input Voltage	100	V
Switching frequency	50	kHz
Regulated DC outputs × 6:		
Output 1	15	V
Output 2	5	V

The auxiliary power supply was required to run off the same supply voltage as the multicell inverter. Therefore, the input voltage specified was 100V DC. Each MOSFET switch's driving and control circuit needed both a 5V and a 15V DC supply; this meant only six 5V outputs and six 15V outputs. The switching frequency was chosen as 50 kHz because of the transformer core type used in the step-down transformer.

##### 4.4.2 Auxiliary power supply design

As noted previously in section 4.4.1, an auxiliary power supply needs to run from the same supply voltage as supplied to the multicell inverter. This was realised by using a zener diode as a voltage regulator to clamp the voltage down to 15.1V (the voltage rating of the diode). This clamped voltage of 15.1V was fed to the signal generator and the gate drivers of the half-bridge inverter used in the auxiliary supply, as shown in Figure 4.11.

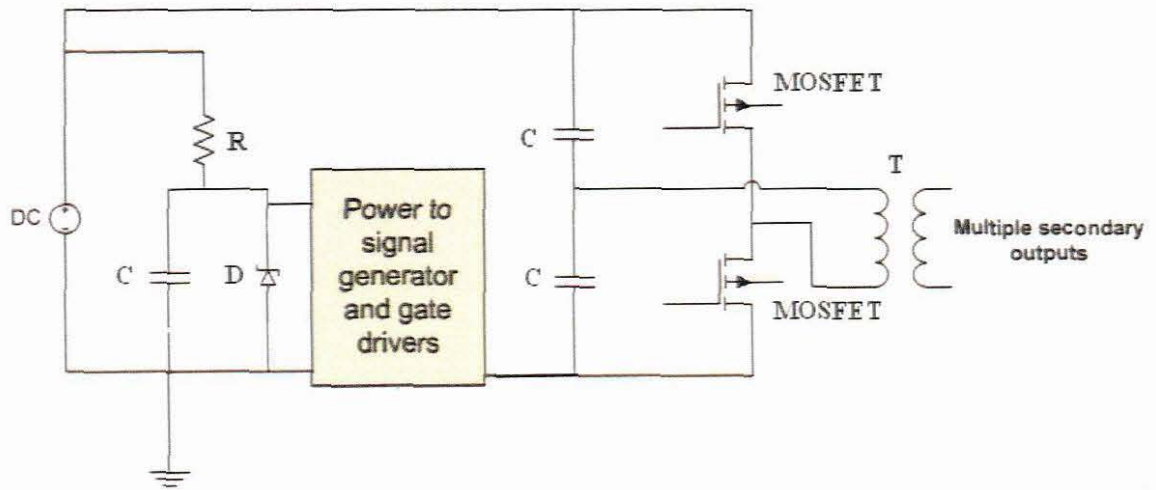


Figure 4.11: The overview of the half-bridge inverter and step-down transformer stage of the auxiliary power supply

The output AC voltage waveform of the half-bridge inverter was then fed into a step-down transformer where it is stepped-down into six identical lower voltage waveforms. These lower voltage AC waveforms were then rectified and regulated to produce specified voltage levels.

#### 4.4.3 Half-bridge inverter stage

The first part of the auxiliary power supply was, therefore, the half-bridge inverter. The half-bridge inverter used in the auxiliary power supply converted the 100 V DC bus voltage to a 100 V peak to peak AC voltage.

The MOSFET driver used for the inverter circuit was an International Rectifiers IR2113 high and low side driver. Two 100  $\mu$ F bus splitting capacitors were used and the MOSFETs used were International Rectifiers IRF520 devices with voltage and current rating of 100 V and 9.2 A respectively. Figure 4.12 illustrates the converter.

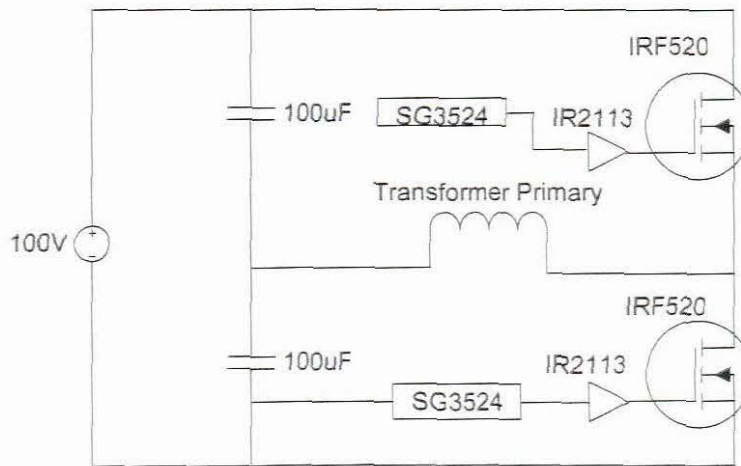


Figure 4.12: The half-bridge inverter with the components as used in the project

The next stage of the auxiliary power supply was to convert the 100  $V_{p-p}$  to smaller voltage levels, isolated from one another, in order to be rectified by a bridge rectifier. The schematic diagram with the actual components used for the half-bridge inverter in the auxiliary power supply was shown in Figure D1 in Appendix D.

#### 4.4.4 Multiple output step-down transformer

The multiple output transformer was an important part of the auxiliary power supply as the outputs to the switches and its driving circuits needed to be electrically isolated from one another. The design methodology of the transformer is discussed.

Table 4.5: Transformer output ratings

Transformer Output	Voltage( $V_{p-p}$ )	Current( $mA_{RMS}$ )
1	15	100
2	15	100
3	15	100
4	15	100
5	15	100
6	15	100

Multiple outputs were needed from the transformer, as shown in Table 4.5. The transformer was designed to give an output voltage of 15 V and an output current handling capability of 100 mA per output winding. The current rating was chosen after considering the total current that was drawn by the driving circuitry of each switch. A greater current value was chosen for a reasonable safety margin.

The transformer was designed for a primary voltage of + 50V and -50V swing from the half-bridge inverter. An ETD 29 core made of N27 material was selected for the design of the transformer for this power supply. The ETD 29 transformer cores were used for power applications for a switching frequency of up to 100 kHz. The design parameters of the transformer are shown in Table 4.6.

**Table 4.6: The design parameters of the transformer**

Parameter	Symbol	Value	Unit
Maximum input voltage	$V_d/2$	50	V
Maximum primary side voltage	$V_p$	100	V
Switching frequency	$f_s$	50	kHz
Effective area of core	$A_e$	76	mm <sup>2</sup>
Maximum magnetic flux density of the core	$\hat{B}_m$	200	mT
Maximum magnetic flux	$\varphi = \hat{B}_m A_e$	15.2	μWb

The design of the primary windings of the transformer used Faraday's Law.

From:

$$V_{pri} = N_{pri} \times \frac{d\varphi}{dt} \quad (4.34)$$

We get:

$$N_{pri} = V_{pri} \times \frac{\Delta t}{\Delta\varphi} \quad (4.35)$$

Since  $\varphi = \hat{B}_m A_e$ , then

$$N_{pri} = \frac{V_{pri}}{4A_e \Delta \hat{B}_m f_s} \quad (4.36)$$

Therefore:

$$N_{pri} = \frac{50}{4(15.2\mu)(50000)} = 16.4 \text{ turns}$$

This was the minimum amount of turns theoretically on the primary winding. The next integer 17 would be the *minimum number of turns* needed. To prevent the transformer from saturating, the number of turns was increased to 20.

The secondary windings for the secondary voltages were calculated using:

$$\frac{V_{sec}}{V_{pri}} = \frac{N_{sec}}{N_{pri}} \times D \quad (4.37)$$

Which was rewritten as

$$N_{sec} = \frac{V_{sec} N_{pri}}{V_{pri} D} \quad (4.38)$$

For the 15 V output, the secondary windings were:

$$N_{sec1} = \frac{(15)(20)}{(100)(0.5)} = 6 \text{ turns}$$

The duty cycle  $D$  is defined as the ratio between the duration of the pulse  $t_o$  and the total period  $t_T$  of the rectangular waveform, as illustrated in Figure 4.13.



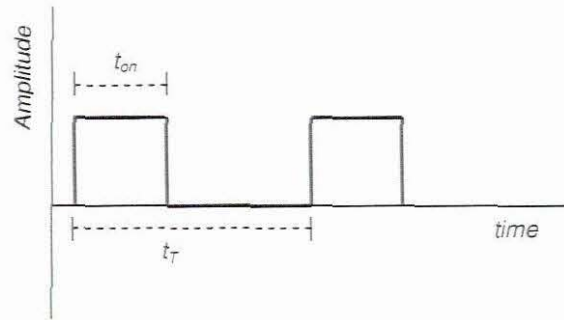


Figure 4.13: A waveform diagram illustrating the duty cycle of a signal

The thickness of the primary and secondary windings was a function of the current flowing through it. This was determined using the maximum current density of  $6 \text{ A/mm}^2$ . The cross-sectional area of the secondary winding was given by:

$$A_{\text{sec}} = \frac{I_s}{6}$$

The diameter of the secondary winding was given by:

$$D_{\text{wire}} = \sqrt{\frac{4A_{\text{sec}}}{\pi}} \quad (4.39)$$

$$D_{\text{wire}} = \sqrt{\frac{4 \times \frac{I_s}{6}}{\pi}} \quad (4.40)$$

Using a 100 mA for all the windings, the diameter of the wire was given by:

$$D_{\text{wire}} = \sqrt{\frac{4 \times \frac{0.1}{6}}{\pi}}$$

$$D_{\text{wire}} \approx 0.21 \text{ mm}$$

Therefore, a wire diameter of 0.4 mm was chosen as suitable for all secondary windings. The diameter was chosen as a greater value than calculated as a safety margin.

The primary current is given by the relation:

$$\frac{I_{\text{pri}}}{I_{\text{sec}}} = \frac{V_{\text{sec}}}{V_{\text{pri}}} = \frac{N_{\text{sec}}}{N_{\text{pri}}} D \quad (4.41)$$

$$\frac{I_{\text{pri}}}{I_{\text{sec}}} \approx 0.5$$

$$I_{pri} = 0.5(200 \times 10^{-3})$$

$$= 0.1$$

$$A_{pri} = \frac{0.1}{6}$$

$$A_{pri} = 0.016 \text{ mm}^2$$

The thickness of each of the secondary wires was given by:

$$D_{wire} = \sqrt{\frac{4A_{pri}}{\pi}} = 0.143 \text{ mm}$$

A wire diameter of 0.4mm was selected in this power supply design. The diameter was chosen to be a greater value than calculated as a safety margin.

The output voltages from the various secondary windings had to be rectified, then regulated to DC voltages required by the drivers and controllers of the multicell inverter. Section 4.6.5 describes the final stage of the auxiliary power supply.

#### 4.4.5 Rectifying stage

This stage of the power supply rectified each of the secondary output voltage waveforms from the transformer to a DC voltage and thereafter regulated the voltages to its desired magnitudes.

This was easily achieved by connecting the secondary output of the transformer to a full-bridge rectifier as seen in Figure 4.14. The full-bridge rectifiers used for the rectification had a current rating of 1A. The rectified voltage is then regulated by using 15V (LM7815) and 5V (LM7805) regulators. The schematic diagram of the regulator stage was illustrated in Figure D2 in Appendix D.

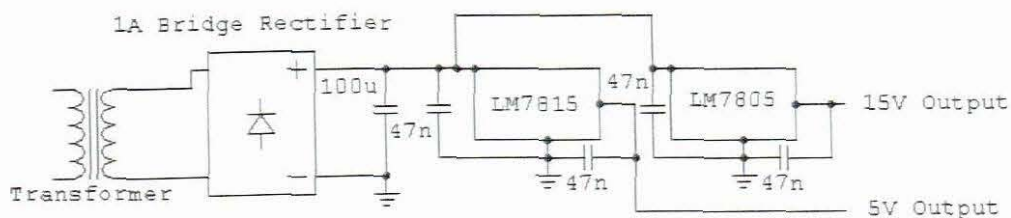


Figure 4.14: The rectification and regulation stage

## 4.5 Switching signal generator

In order to produce the stepped output waveform of the multicell inverter, the switches needed to be conducting in a specific sequence. This switching pattern was a modulation technique and the modulation technique used for this inverter topology is described next:

### 4.5.1 Introduction to Pulse-Width Modulation Control (PWM)

PWM control is a method for controlling the output voltage of an inverter system. The output voltage waveform consisted of a single pulse in each half-cycle. The pulse-width of the switching signal was varied to control the output AC voltage waveform. For a simple half bridge inverter the output voltage was obtained by driving the MOSFETs with two square wave signals which were  $180^\circ$  out of phase with each other. The switching sequence required to build the stepped near-sinusoidal output waveform of the multicell inverter required a variation of the modulation technique, explained in Section 4.5.2.

### 4.5.2 Sinusoidal Pulse-Width Modulation

The PWM technique used for this study was the SPWM technique. The name of the modulation technique describes the nature of the implementation. A reference sinusoidal waveform was compared against a high frequency carrier signal to produce the SPWM signals as shown in Figure 4.15.

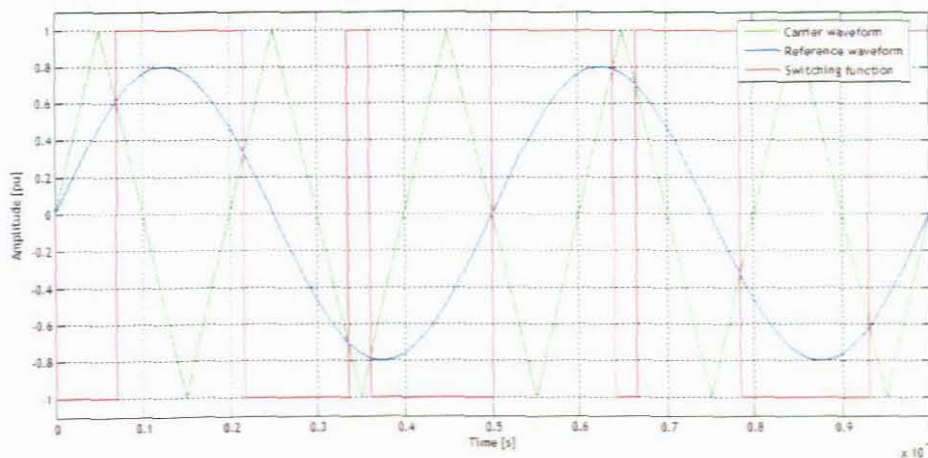


Figure 4.15: Reference sinusoidal waveform being compared with a high frequency carrier triangle waveform. The resulting SPWM signal from the comparison between the reference and the carrier waveform is shown

### 4.5.3 Interleaved SPWM technique

For implementation in the multicell inverter topology, SPWM signals generated must be phase shifted in order for commutation cells not to switch simultaneously; when they are switched at the same time it will effectively be a short circuit condition. This is called interleaved switching. For a 3 cell multicell inverter the carrier signals of the cells are phase-shifted by  $2\pi/p$  where  $p$  is the number of commutation cells. It was, therefore, seen each commutation cell was controlled by its own carrier signal which is compared to a reference signal at a fundamental frequency. The interleaved SPWM switching technique resulted in an apparent switching frequency which was  $p$  times the switching frequency of a single commutation cell. It also produced an output ripple voltage of amplitude equal to  $V_d/p$ . This high apparent switching frequency resulted in the smoothing inductor size to be reduced by a factor of  $p^2$  (Meynard et al, 1995) and the capacitor size to be reduced by a factor of  $p^3$  compared to a conventional half-bridge inverter. It also resulted in the flying capacitor values to be smaller (Wu et al, 1999). The result of the interleaved SPWM switching scheme on a 3 cell multicell inverter is shown in Figure 4.16.

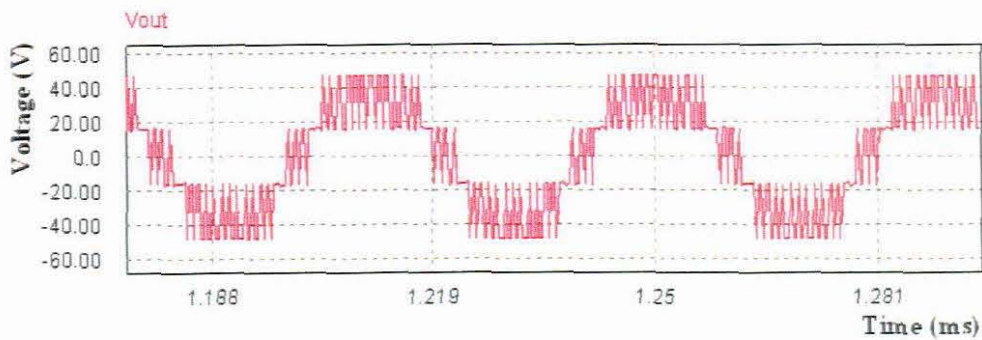
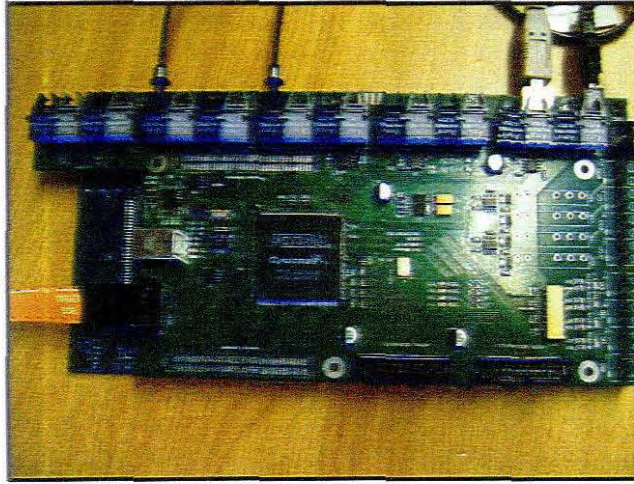


Figure 4.16: The resulting output of a 3 cell multicell inverter with the interleaved SPWM switching scheme

The digital controller is being designed by another Masters student (CR Jooste) at the Centre for Instrumentation Research (CIR) at the Cape Peninsula University of Technology (CPUT). A sinusoidal reference signal generated by a DSP (digital signal processor) device is compared with a modulator in a FPGA (field programmable gate array) device. An example of the development board used is shown in Figure 4.17.



**Figure 4.17:** The FPGA development board used to generate the switching signals for the inverter

The FPGA phase shifted the switching signals of the three cells and inverted the switching signals for the complementary switching pairs; the digital controller was electrically isolated by fibre optic transmitters and receivers. .

#### **4.6 Conclusions**

The design procedure of a four-level multicell inverter inverter was given. The switching frequency of each cell of the inverter is 300 kHz, which causes the apparent switching frequency of the inverter to be 900 kHz, because the output apparent frequency is equal to switching frequency multiplied by the number of commutation cells (Hamma, 1995).

A 3 cell multicell inverter prototype was designed and built (see Figure 4.18) according to design specifications and results obtained are discussed in Chapter Five.

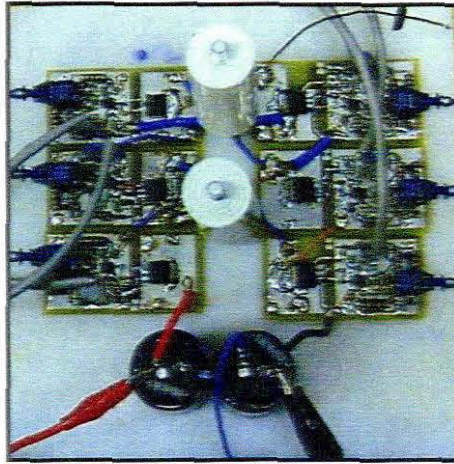


**Figure 4.18: The 3 cell multicell inverter prototype**

The specifications and the design of the auxiliary power supply were also discussed in detail. The auxiliary power supply was tested (see Chapter Five for results).

Chapter Five presents and discusses the experimental results of the multicell inverter, the auxiliary power supply and the ultrasonic plastic welding system.

## CHAPTER FIVE EXPERIMENTAL RESULTS

This chapter presents the experimental results obtained from the practical work completed on the auxiliary power supply described in Chapter Four and the multicell inverter described in Chapter Five. The equipment used for measuring and capturing the data for the auxiliary power supply was a Tektronix TDS 2024B oscilloscope with a Tektronix P2220 probe and an Agilent 54622A oscilloscope with the Agilent 10074C probes used for both auxiliary power supply and multicell inverter. The Tektronix TCPA300 Amplifier and AC/DC current probe measured the multicell inverter current waveforms. The voltages of the balancing capacitors were measured using a Tektronix 1103 TEKPROBE Power Supply with the Tektronix P5205 differential probes. The software package used to simulate the predicted waveforms of the multicell inverter with the various plastic loads was PSIM version 7.0.

### 5.1 Testing of auxiliary power supply

The half bridge inverter in the auxiliary power supply was the first of the auxiliary power supply to be tested. A first reading taken was the output of the half-bridge inverter used in the auxiliary power supply with an input voltage of 100V DC. The captured waveform is seen in Figure 5.1 to be a voltage  $100 V_{p-p}$  at an operating frequency of 50 kHz.

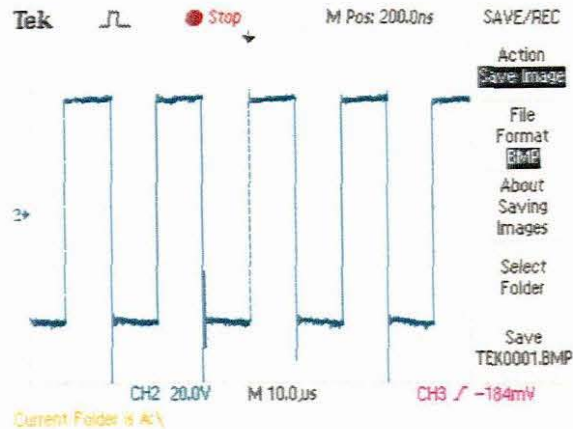


**Figure 5.1: The output of the inverter of the auxiliary power supply on the primary of the transformer**

The output voltage of the half-bridge inverter was then fed into the primary side of the multiple-output step-down transformer. The voltage waveform on one of the secondary outputs was measured and the captured waveform is displayed in Figure 5.2; the output voltage waveform is  $15 V_{p-p}$  at a frequency of 50 kHz.

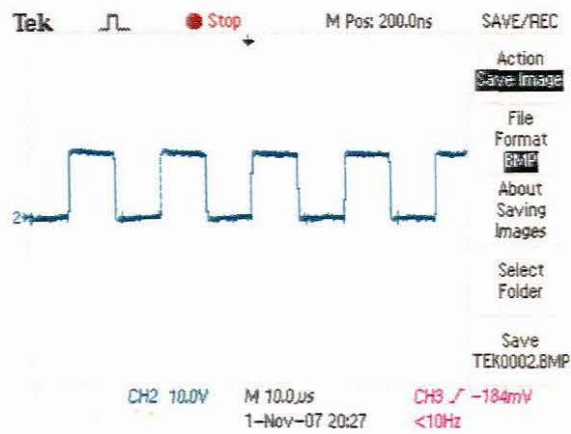


Figure 5.2: The output of the inverter on the secondary of the transformer

Each of the six output AC voltage waveforms from the transformer, as shown in Figure 5.2, was then fed through an individual rectifying and regulating circuit. The two voltage levels obtained for each of the six switches' driving circuitry are seen in Figure 5.3, and are identical.

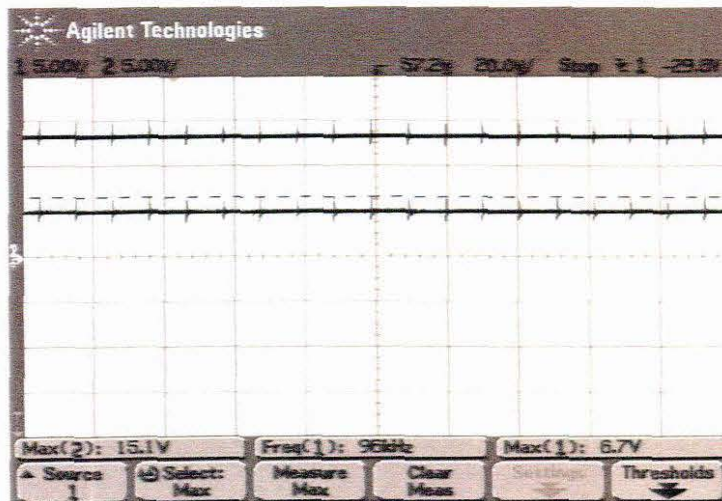


Figure 5.3: The regulated outputs of one of the regulating stages

The complete auxiliary power supply was tested with the multicell inverter as a system and all voltage levels were correct.



## 5.2 Testing of the multicell inverter

The multicell inverter had to be tested with both a resistive and an ultrasonic load to prove it operated correctly in line with this study.

### 5.2.1 Testing a single commutation cell as a half-bridge inverter

Figure 5.4 gives an illustration of the experimental setup that was used to test a single commutation cell as a half-bridge inverter.

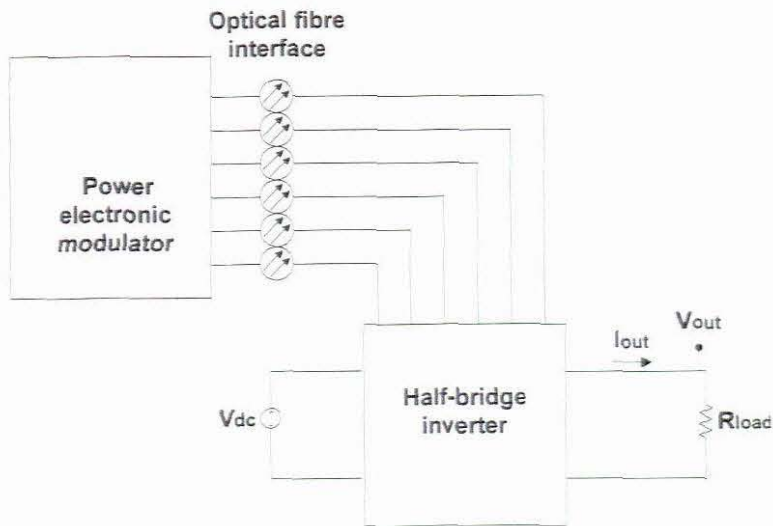


Figure 5.4: Block diagram illustrating the experimental setup used for testing the half-bridge inverter

A single cell of the multicell inverter was first tested as a half-bridge inverter topology to discover if everything worked correctly. The first result obtained from the half-bridge inverter was when it was driven at a switching frequency of 100 kHz. The captured waveform is shown in Figure 5.5; this initial test was carried out at a lower DC bus voltage of only 17 V DC.

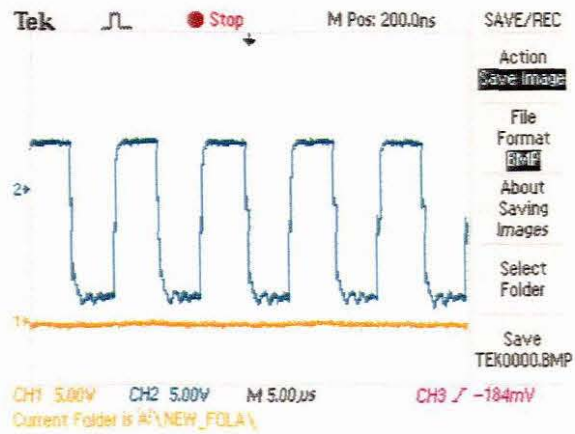


Figure 5.5: The inverter output at a switching frequency of 100 kHz

A stable output waveform was obtained and it was decided to increase the switching frequency of the inverter to the specified 300 kHz.

With the half-bridge inverter setup switching at 300 kHz waveforms of the gating signals (see Figure 5.6) and the output voltage (see Figure 5.7) were taken.

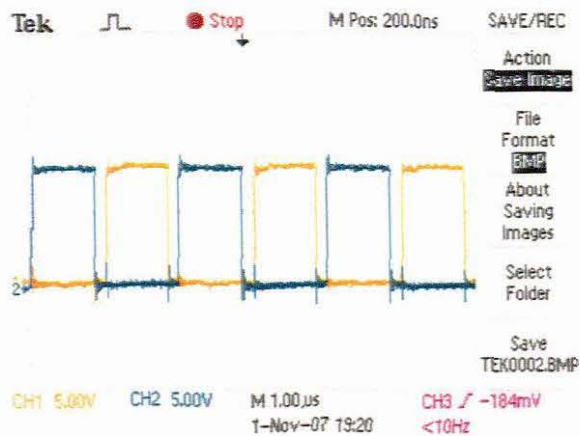


Figure 5.6: The gating signals on the IRF520 MOSFET at 300 kHz

The signals on the gate of the MOSFETs were measured to be the correct voltage level (10 V) and frequency (300 kHz), but the output waveform of the inverter contained unwanted oscillations and ringing.

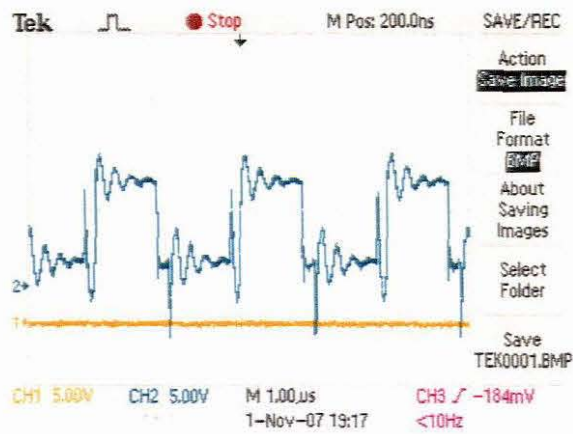


Figure 5.7: The output of the half-bridge inverter at 300 kHz driving a resistive load

As can be seen in Figure 5.7, there was considerable oscillation, or ringing on the output voltage of the inverter. Upon further investigation a possible cause of the ringing was identified as parasitic inductance in the physical inverter circuit. The MOSFET switching device had parasitic inductance from the packaging, as seen in the equivalent circuit of power MOSFET device in Figure 5.8. These inductances are caused by physical wire connections to the circuit which are typically negligible at low frequencies, but have an effect at high frequencies as the parasitic inductance maintains a constant current during the turn-off of the MOSFET. This causes the MOSFETS to have a greater commutation loss.

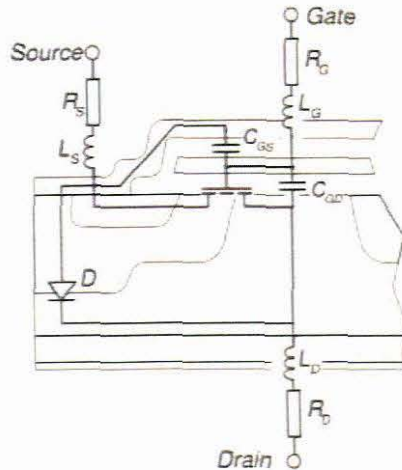
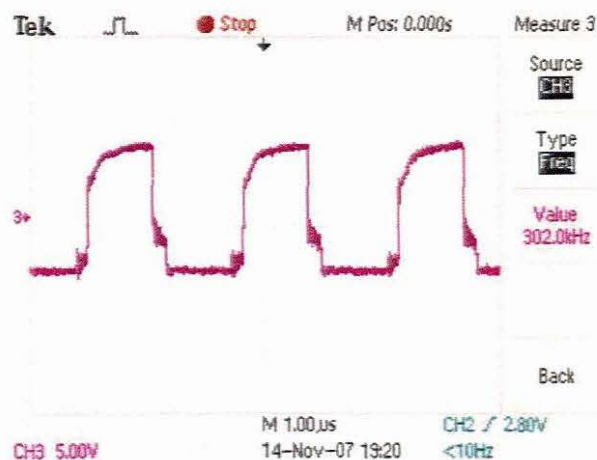


Figure 5.8: The equivalent circuit of a power MOSFET device (Anon, 2008)

Other factors which might have added to the parasitic inductance of the system were lead inductance, poor PCB layout and long connection wires. These effects were reduced by shortening all the connection wires and by using decoupling capacitors at the correct places in the circuit. The MOSFET device inductance was reduced by choosing a D2PAK package instead of the TO220 package, because the leg leads are shorter and the drain tab is also

much smaller compared to the TO220 package. A future consideration would be to opt for a DirectFET switching device, which when connected the correct way, has the smallest inductance of all the standard packages.

The results obtained after shortening all the connecting wire lengths and replacing the TO220 packages with D2PAK packages are shown in Figure 5.9.



**Figure 5.9: The output of the half-bridge inverter after leads were shortened and D2PAK device were used**

Results of the output voltage of the half-bridge inverter after the D2PAK MOSFETs were switched at 300 kHz contained virtually no ringing and were stable. It was decided, therefore, to test the multicell inverter as a 3 cell topology.

### 5.2.2 Testing the 3 cell multicell inverter topology with a resistive load

Figure 5.10 provides an illustration of the experimental setup that was used to test the 3 cell multicell inverter with a resistive load.

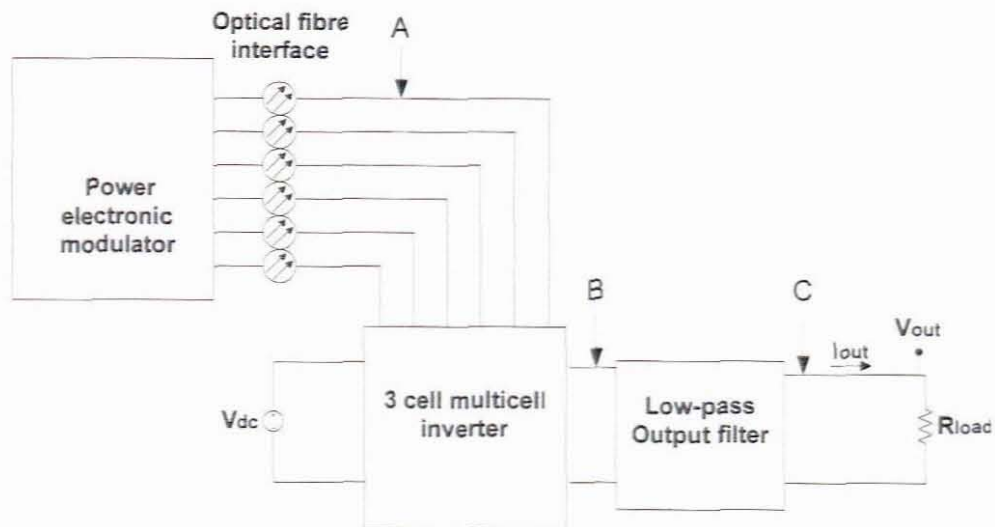


Figure 5.10: Block diagram illustrating the experimental setup used for testing the 3 cell multicell inverter with a resistive load

The FCMLI was then tested with a resistive load as the three cell configuration was used for this project. The first test run used a switching frequency for each commutation cell of 80 kHz. This related to an apparent switching frequency of the converter of 240 kHz. The captured unfiltered output voltage waveform at a switching frequency of 80 kHz is shown in Figure 5.11. The unfiltered waveform presented in Figure 5.11 was measured at the point B in Figure 5.10.

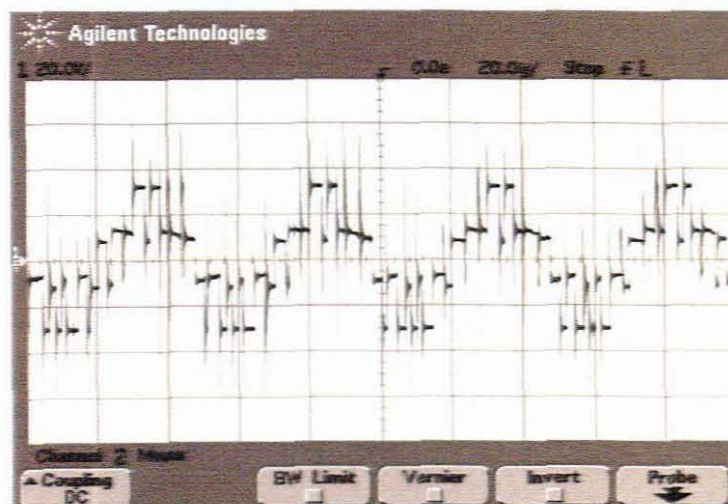


Figure 5.11: Unfiltered output of the multicell inverter at a switching frequency of 80 kHz or an apparent switching frequency of 240 kHz

The 3 cell multicell inverter operating at a switching frequency of 80 kHz was tested. A stable 4 level output voltage were measured at an apparent switching frequency of 240 kHz.

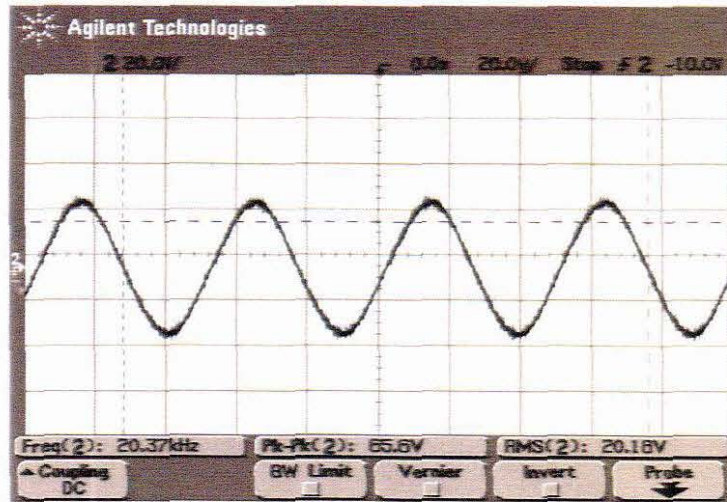


Figure 5.12: Filtered output of the multicell inverter at a switching frequency of 80 kHz or an apparent switching frequency of 240 kHz

The filtered output voltage seen in Figure 5.12 was measured at point C in Figure 5.10.

It was decided to increase the frequency to the specified 300 kHz per commutation cell as stated for this project. This translates to an apparent switching frequency of 900 kHz of the inverter. The 300 kHz complementary pair of switching signals for one commutation cell measured at the gates of the MOSFETs measured at point A on Figure 5.10 is shown in Figure 5.13.

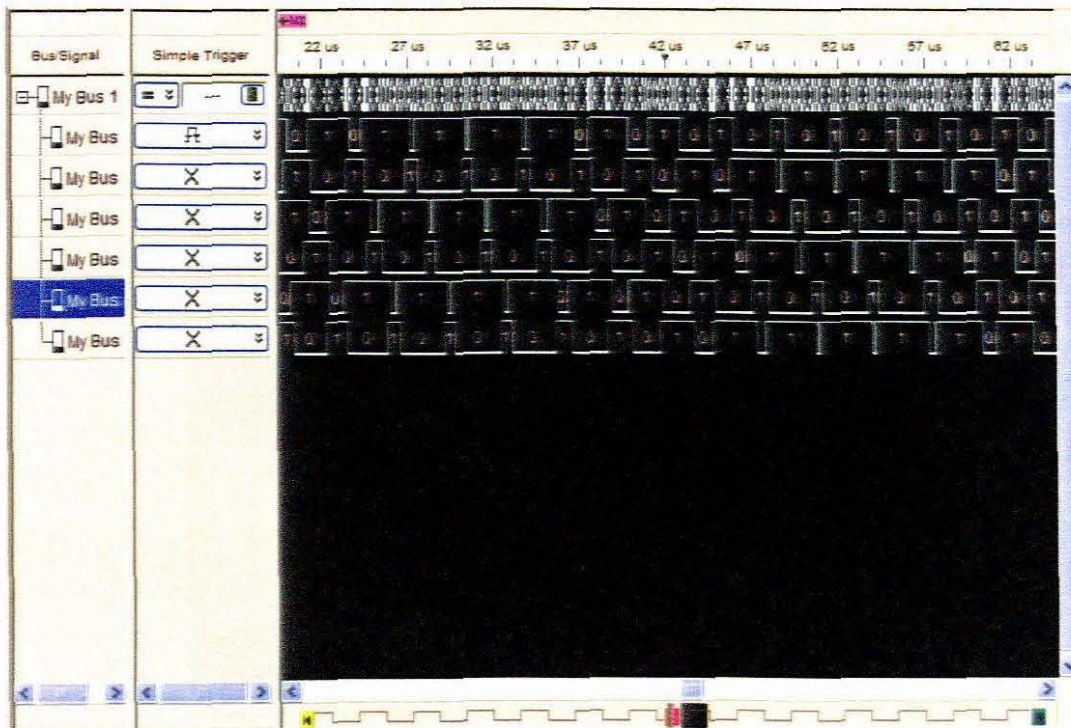


Figure 5.13: A screen shot of the 300 kHz complementary switching signals for the three commutation cells taken from a logic analyser

The next step was to see if the flying capacitors were “balanced,” in other words constant at required voltage levels. The required voltage levels for the 3-cell multicell inverter were 66% of the input voltage for the first flying capacitor and 33% of the input voltage for the second flying capacitor. The input voltage to the inverter for the simulation was set at 120 V DC and the corresponding voltage levels on the flying capacitors were 80 V for the first flying capacitor and 40 V for the second flying capacitor as was expected (see Figure 5.14 for the simulated). The experimental setup for the resistive load was set to an input voltage of 56 V. The measured waveforms in Figure 5.15 shows that  $V_{c1}$  was 37.5 V (cursor Y2 on Figure 5.15) which is  $2/3 V_{dc}$ .  $V_{c2}$  was shown to be  $1/3 V_{dc}$ .

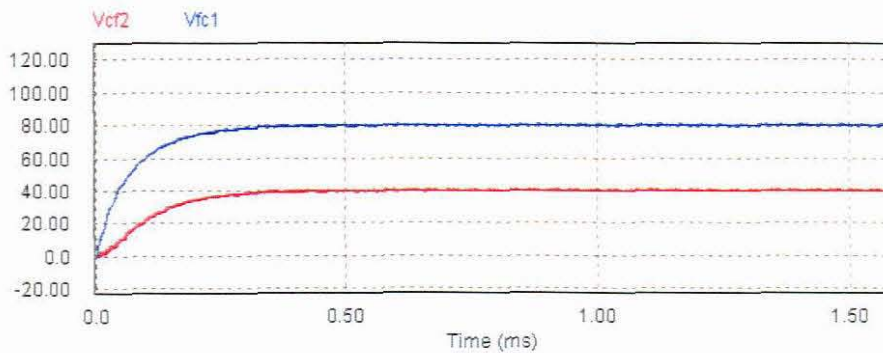


Figure 5.14: The simulated flying capacitor voltage levels

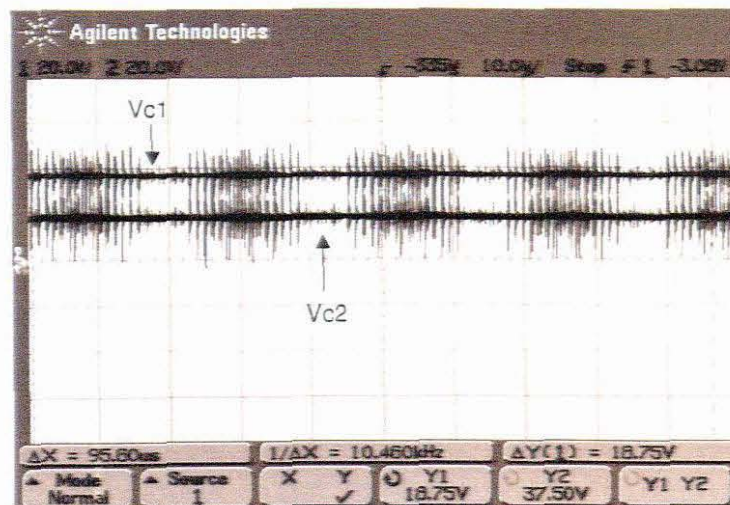


Figure 5.15: Flying capacitor voltage levels

The unfiltered output voltage was also measured and the captured waveform seen in Figure 5.16. Although the output signal at an apparent switching frequency of 900 kHz was “noisy”, the four voltage levels can be seen clearly. The waveform in Figure 5.16 was measured at measuring point B in Figure 5.10.

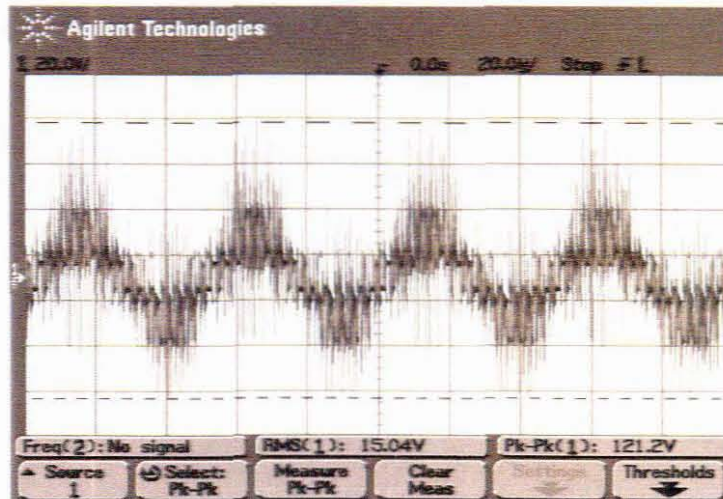


Figure 5.16: Unfiltered output voltage of multicell inverter at a switching frequency of 300 kHz or an apparent switching measured at a frequency of 900 kHz

The frequency spectrum of the waveform shown in Figure 5.16 is shown in Figure 5.17. The span of the spectrum was set to be 5 MHz with the centre of the spectrum set at 2.5 MHz.

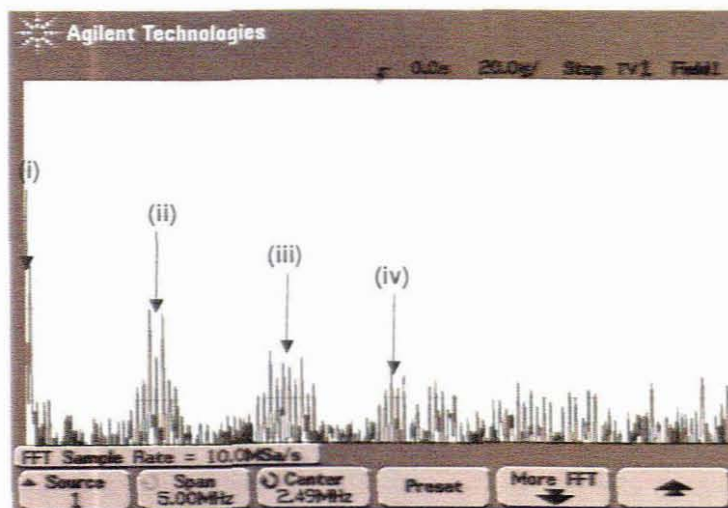


Figure 5.17: The frequency spectrum measurement of the unfiltered output voltage measured at measuring point B in Figure 5.10



It was illustrated in Figure 5.17 that the apparent switching frequency caused the switching harmonics to be shifted up the frequency spectrum to 900 kHz (marker (ii)). The fundamental of the reference waveform (22 kHz) was indicated by marker (i). The harmonics at multiples of the apparent switching frequency (marker (iii) at 1.8 MHz and marker (iv) at 2.7 MHz) is propagated down the frequency spectrum until it is insignificantly small.

The filtered voltage and current waveforms of the multicell inverter, driving a resistive load is shown in Figure 5.17. The waveforms in Figure 5.18 were measured at measuring point C in Figure 5.10.

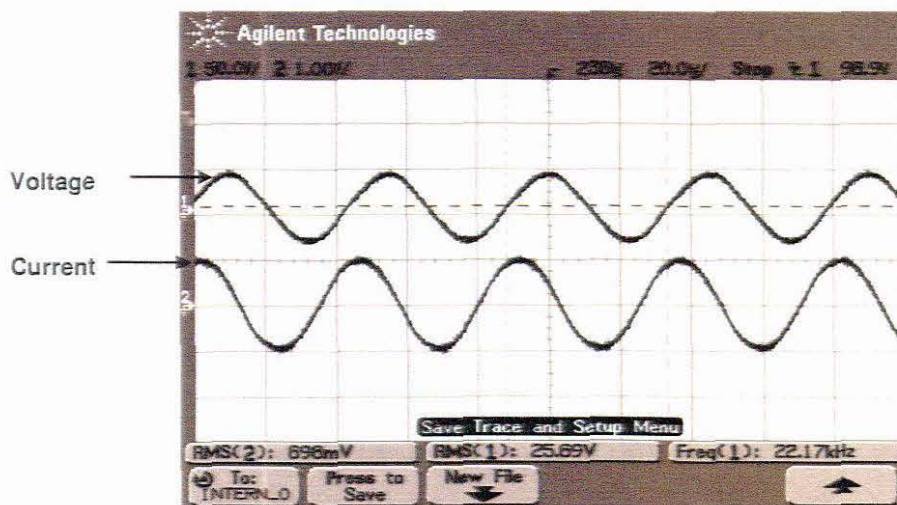


Figure 5.18: The filtered output voltage (top) and current (bottom) waveforms of the multicell inverter driving a wire wound resistor that contains a small inductance, causing the output current to lag the voltage

It was noted the output current and voltage of the inverter was out of phase, but this was expected as the power resistor used for measurement was a wire-wound resistor, therefore not purely resistive, but contained an inductance, which caused the output current to lag the voltage. Trace 1 represented the output voltage; Trace 2 output current.

### 5.2.3 Testing the 3 cell multicell inverter topology with the ultrasonic load

Figure 5.19 gives an illustration of the experimental setup that was used to test the 3 cell multicell inverter with an ultrasonic load.

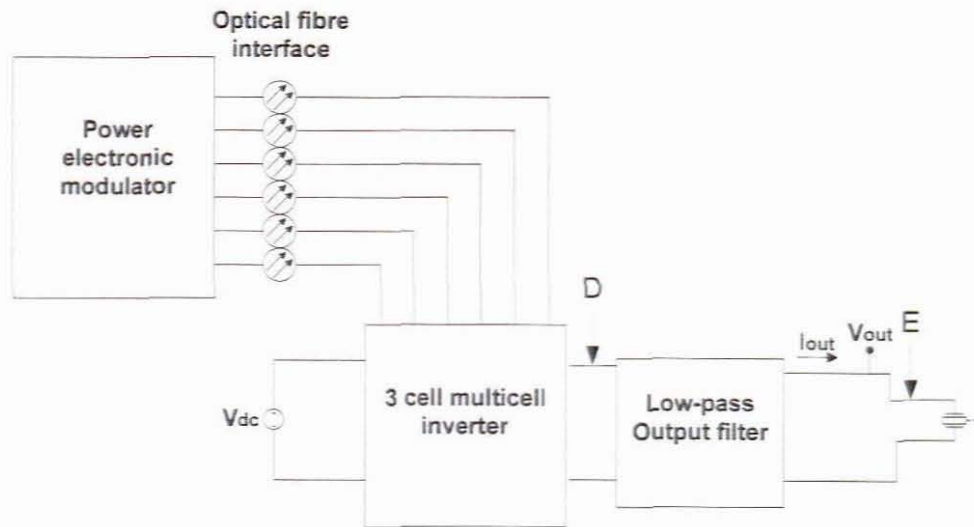


Figure 5.19: The block diagram illustrating the experimental setup used for testing the 3 cell multicell inverter with an ultrasonic load

After good results had been obtained from initial tests of the 3 cell multicell inverter driving a resistive load, it was decided to test it with the ultrasonic transducer as a load at a fixed frequency close to the natural oscillating frequency of the transducer in free air. This frequency at which the ultrasonic transducer resonates in free air was measured as 22.3 kHz with the HP4192A impedance analyser. The reference frequency was set to 22.1 kHz to drive the ultrasonic load. The power was varied manually by increasing the bus voltage supplied to the multicell inverter. However, this is not ideal and would not work in industry applications. Future work will have to include development of a variable PWM drive signal to the buck converter to change the bus voltage supplied to the multicell inverter automatically at turn-on. The frequency was manually set in the firmware of the signal generator to the measured resonance frequency of the ultrasonic transducer obtained from the admittance versus frequency scan on the impedance analyser.

The first test was to see if the flying capacitor would remain "balanced". With an input voltage of 90 V DC, the flying capacitors remained "balanced" with voltage levels at 62.5 V (cursor Y2 in Figure 5.120) and 30 V (cursor Y1 in Figure 5.20) respectively.

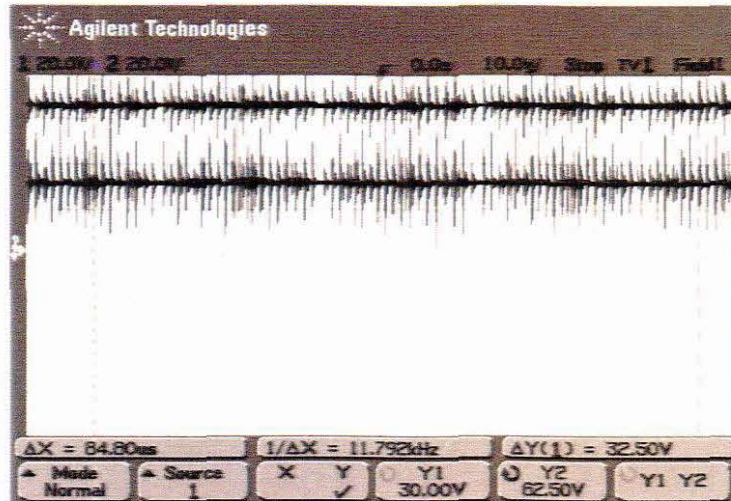


Figure 5.20: Flying capacitor voltage levels with the ultrasonic transducer

The output voltage and current waveforms of the multicell inverter with an ultrasonic load was captured with the transducer loaded with two different plastic samples. The transducer had to be loaded with a material so that sound energy could be transferred into that material. The reason for this was if sound energy was not transferred, it would be reflected back from the tool tip towards the piezoelectric discs and could then lead to the destruction of the device. This in turn is from the acoustic impedance of air being much higher than the acoustic impedance of the ultrasonic transducer.

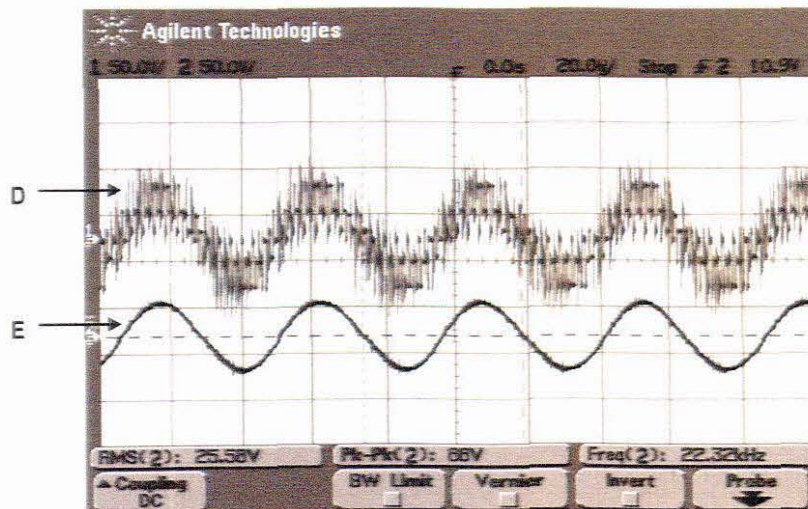


Figure 5.21: The unfiltered (top) and filtered (bottom) waveforms measured at points D and E respectively in Figure 5.19. The switching frequency was 300 kHz and the apparent switching frequency 900 kHz

The simulated output voltage and current waveforms of the ultrasonic tool loaded with a Perspex sample are illustrated in Figure 5.22. The simulated waveforms suggest that the

voltage would lead the current. See Appendix I1 for the simulation setup.

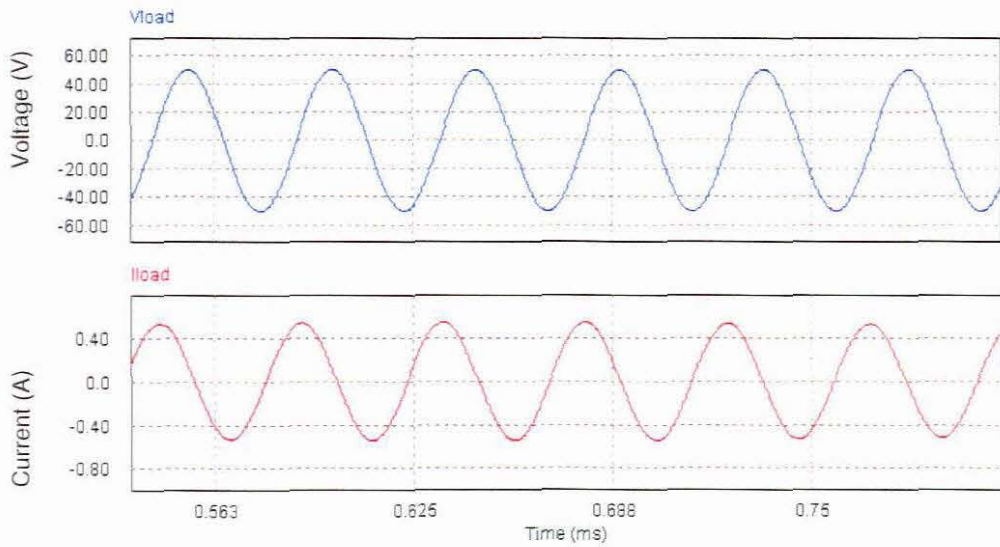


Figure 5.22: The simulated output voltage (top) and current (bottom) waveforms that were captured after filtering of the multicell inverter driving the ultrasonic transducer loaded with a Perspex sample

Figure 5.23 show that the measured voltage of the ultrasonic welding tool loaded with Perspex was leading the current.

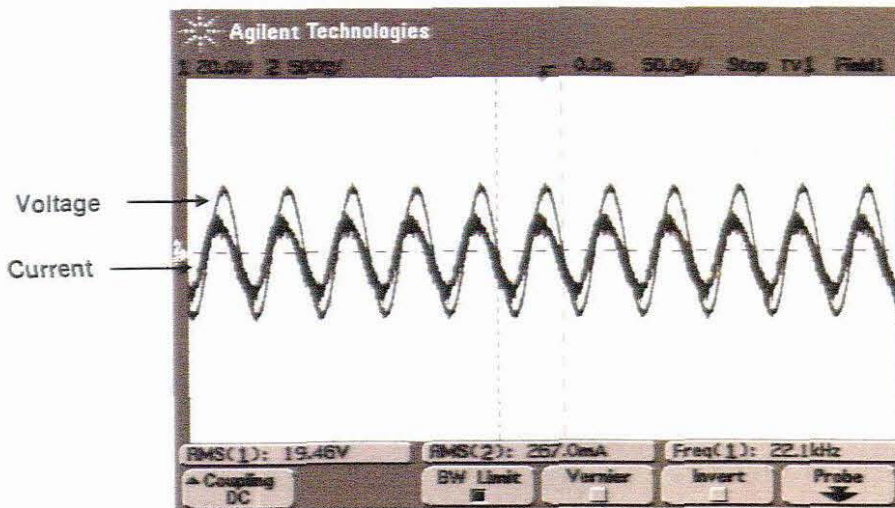


Figure 5.23: The filtered output voltage and current waveforms of the multicell inverter driving the ultrasonic transducer loaded with Perspex sample

The simulated output waveforms of the ultrasonic welding tool loaded with HDPE expected to appear in the measured results (see Figure 5.24), showed current was leading the voltage.

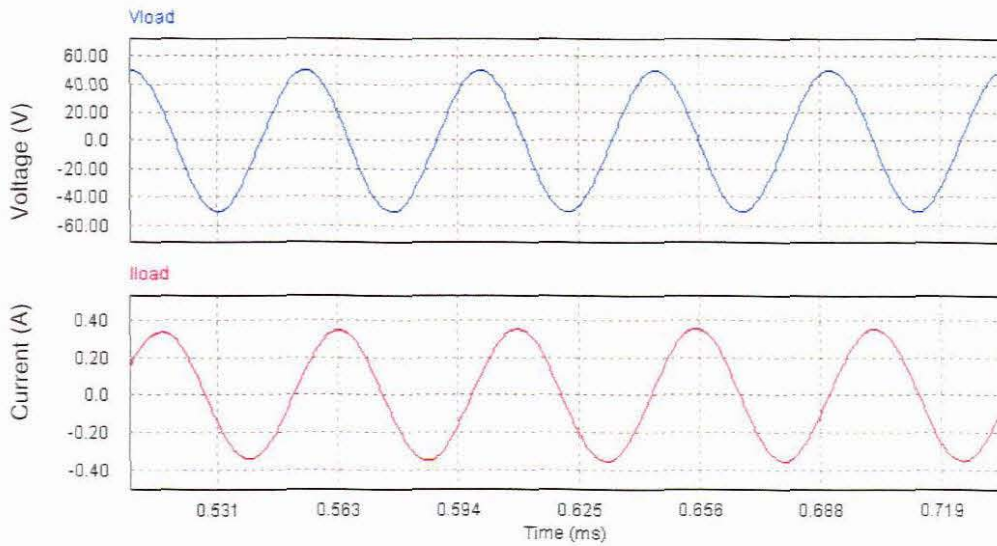


Figure 5.24: The filtered simulated output voltage and current waveforms of the multicell inverter driving the ultrasonic transducer loaded with a HDPE sample

The current and voltage waveforms in Figure 5.25 correlate very well with the predicted simulation in Figure 5.24. It was seen that the ultrasonic transducer was being seen as a capacitive load by the inverter.

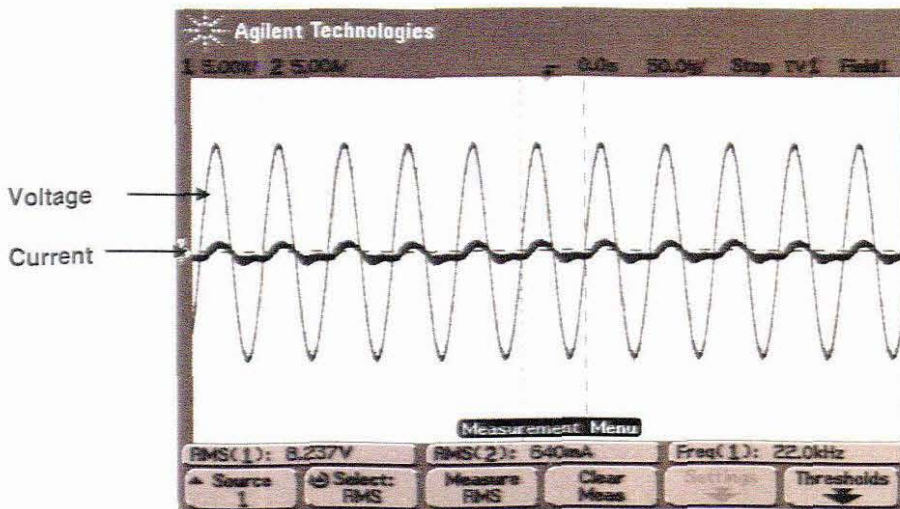


Figure 5.25: The filtered output voltage and current waveforms of the multicell inverter driving the ultrasonic transducer loaded with HDPE sample

It is important to note that the load current seen in Figure 5.25 is of a non-linear load. It was seen from Figure 5.25 that the non-linear load was being driven successfully by the multicell

inverter that was used in this project. This proves that the multicell inverter can drive a non-linear load successfully.

The measured input voltage and current values for the input power calculations were measured as 99.74 V and 93 mA respectively.

The output voltage and current waveforms that were used to calculate the output power is shown in Figure 5.26.

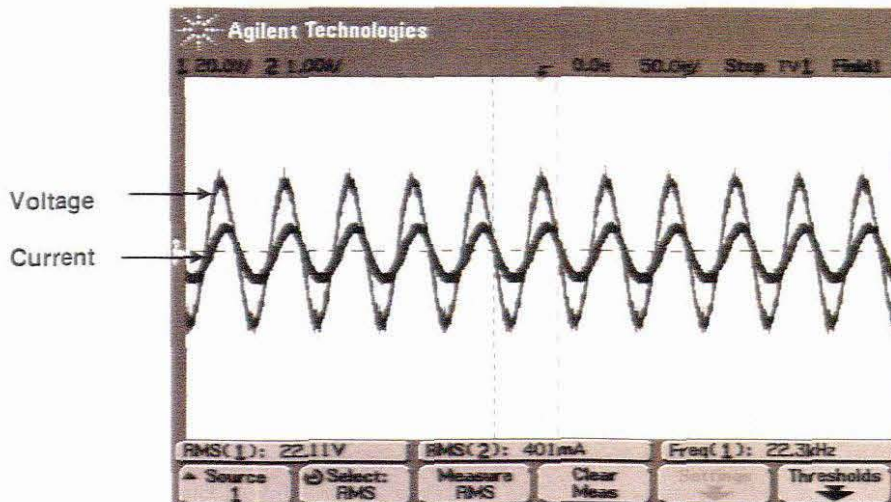


Figure 5.26: The output voltage and current waveforms into the ultrasonic transducer to calculate the output power

The input and output voltage and current levels were measured at exactly the same conditions. The ultrasonic transducer was loaded with HDPE and drilling into it. The input power was calculated to be:

$$P_{IN(RMS)} = V_{IN(RMS)} \cdot I_{IN(RMS)} = (99.74)(0.093) = 9.267W_{RMS} \quad (5.1)$$

where  $V_{IN(RMS)}$  was the input RMS voltage and  $I_{IN(RMS)}$  was the input RMS current delivered to the multicell inverter.

The output power was calculated to be:

$$P_{OUT(RMS)} = V_{OUT(RMS)} \cdot I_{OUT(RMS)} = (22.1)(0.401) = 8.866W_{RMS} \quad (5.2)$$

where  $V_{OUT(RMS)}$  was the output RMS voltage and  $I_{OUT(RMS)}$  was the output RMS current delivered to the ultrasonic transducer.

From the input and output RMS power values the inverter efficiency while driving an ultrasonic load could be calculated.

The efficiency was given as:

$$\eta = \frac{P_{OUT(RMS)}}{P_{IN(RMS)}} = \frac{8.866}{9.276} = 0.956 = 95.6\% \quad (5.3)$$

The efficiency of the three cell multicell inverter driving the ultrasonic load while welding HDPE was calculated to be 95.6 %.

### 5.3 Conclusions

The results obtained from various experiments and tests were presented in this chapter. The auxiliary power supply, the multicell inverter with a resistive and an ultrasonic load were shown to operate effectively from results achieved. The efficiency of the multicell inverter with an ultrasonic transducer loaded with HDPE was also good at 95.6 %. It was shown that the multicell inverter was driving a non-linear load while the inverter was still providing a sinusoidal output voltage and the flying capacitors remained balanced.

## **CHAPTER SIX PLASTIC WELDER TEST**

### **6.1 Testing the system as a plastic welder**

To examine whether or not the inverter and ultrasonic transducer combination used in the project could produce effective spot welds, the quality of the welding joints had to be tested. The test methodology to evaluate the weld quality is also described in this chapter. The welding joint strength could be tested by performing a tensile strength test. A tensile force is defined as a force that tends to pull the component apart (U S Department of Energy, 1992); in other words it is said a component is in tension.

The tested tensile strength can then be compared to either a set of standards or given as a percentage of the tensile strength of the material, ie the tensile strength of a plastic sample is tested then a test is carried out on the welding joint in a sample of the same material.

The tensile property testing procedure ASTM D638, from the American Society for Testing and Materials, was used as a test procedure guideline. In short, the document stated an Instron testing machine must be used for the tensile strength tests and the jaws may move apart at rates of 0.2, 0.5, 2 or 20 inches a minute while pulling the sample from both ends (Society of Plastics Industry, 1976).

In a tensile strength test the sample material will be secured between two clamps. This sample will then be pulled with a specified pulling force until the sample tears or breaks. The breaking point is measured and the tensile strength is given in Newton. An illustration of a typical tensile strength testing apparatus is shown in Figure 6.1. This test is a good indicator of the strength quality of a plastic spot weld where the welds produced were under nearly perfect application of downward force and welding time.



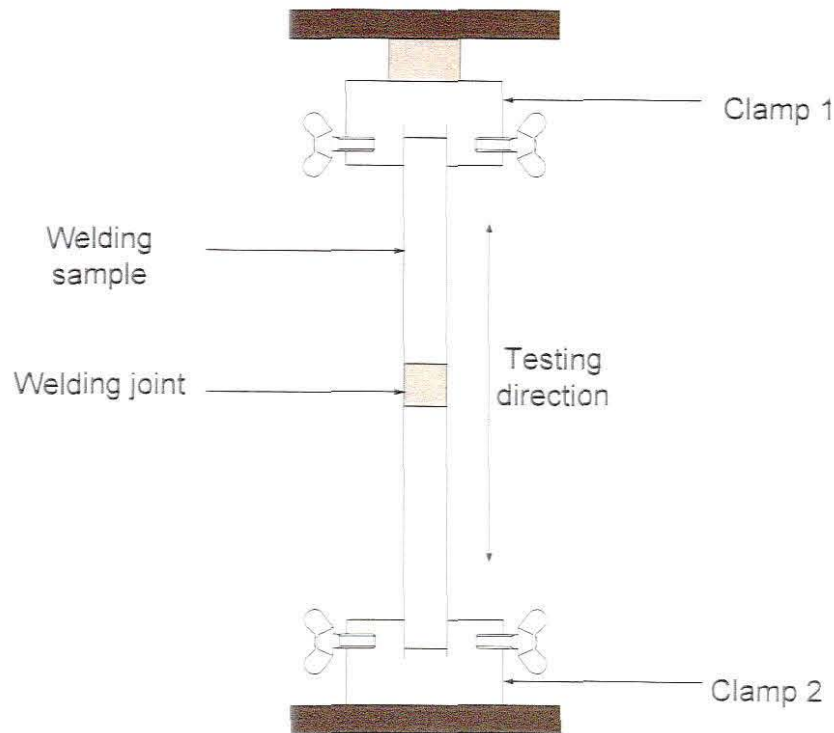


**Figure 6.1: Typical tensile strength testing apparatus**

Another method to evaluate a plastic spot weld was by a chemical test. This method required the spot welded sample to be immersed in acetone between two and four hours (Kamweld, 2003). Faulty welds separate from the sample material. Any strains and stresses will also be visible, because the chemical causes the material to swell in that area (Kamweld, 2003). The chemical used for the test is acetone. This method clearly showed whether or not the system produced good quality spot welds regardless of downward force and time applied.

### **6.1.1 Spot welding results**

The types of plastic samples chosen to be welded were the thermoplastics acrylonitrile butadiene styrene (ABS), polyester, polyvinyl chloride (PVC) and polyethylene terephthalate (PET).

ABS was the plastic material credit cards are made from. The samples used had a thickness of 0.8mm. Polyester is the material that transparency paper is made of. The thickness of the polyester samples used in the experiments was 0.3mm. The thickness of the PVC sample used was 0.4mm and such PVC strips were commonly used in the packaging industry. The PET samples were 0.4 mm thick and was the plastic material used to construct certain soft drink bottles.

Among factors influencing the quality of the weld were downward force and the welding tip diameter and shape. The tip of the ultrasonic horn was measured to have a diameter of 3.28mm; the transducer is setup as shown in Figure 6.2.



**Figure 6.2: Experimental ultrasonic plastic welding setup**

No external downward force, except for the weight of the welding tool was applied during the welding operation. Therefore, the downward force given was the weight of the ultrasonic welding tool multiplied by the gravitational acceleration. The downward welding force was about 19.62 N (with the transducer/welding tip combination weighing 2 kg).

When the spot welding tests were performed, two plastic samples were placed on top of each other and clamped down rigidly. Without applying external downward force on the transducer, the samples came into contact with the welding tip for 5 seconds each. The physical results of the welded samples are shown in Figures 6.3 – 6.7. Three ABS sample pairs from a credit card were welded together as shown in Figure 6.3. Figure 6.4 shows two pure ABS sample pairs welded together. Figure 6.5 shows the results of the polyester samples welded together and Figure 6.6 shows the result of the PVC strips welded together. The final samples that were spot welded were the PET samples, shown in Figure 6.7.

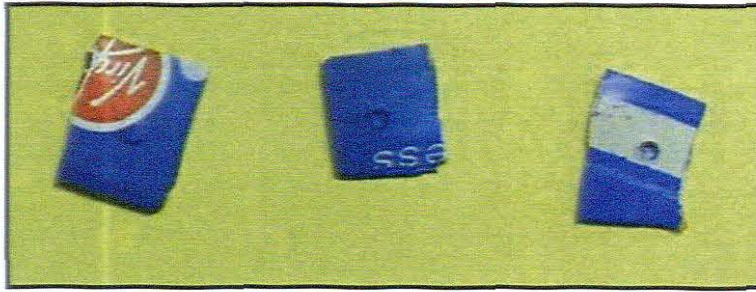


Figure 6.3: ABS samples from a credit card spot welded

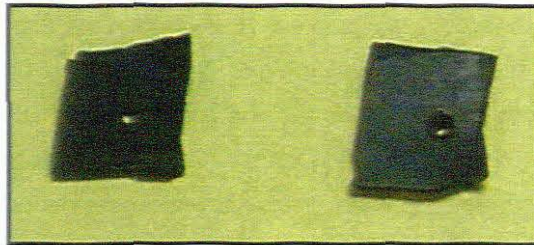


Figure 6.4: Pure ABS samples spot welded together

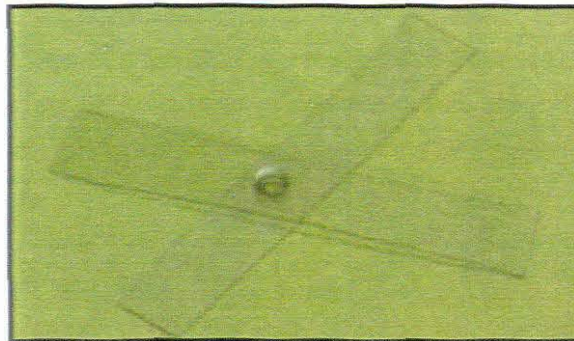


Figure 6.5: Polyester samples spot welded

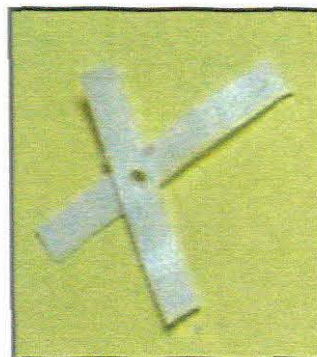


Figure 6.6: PVC strip samples spot welded



**Figure 6.7: PET samples spot welded**

The ABS samples in Figure 6.4 both had a good penetration and bond as the actual welding joint could clearly be seen on both ends of the welding joint. The ABS samples shown in Figure 6.3, however, did not have good penetration and the weld was poor, because the weld was not properly formed. Figures 6.5 – 6.7 shows thinner samples of Polyester, PVC and PET respectively spot welded at the same conditions. All of the welding joints on these samples had excellent penetration and the welding joints were strong (see Section 6.1.2).

From observing the spot welds on each sample, it was evident the welding operation was dependant on various conditions. On closer inspection it was seen the welding penetration of some of the initial samples was too shallow, resulting in a poor weld. This was the result of the combination of a low welding force and a short weld time. Therefore, as with any handheld tool, the quality of the weld is proved dependant on the correct use of the tool.

### **6.1.2 The tensile strength test**

The machine used for testing the tensile strength of the spot welding joints was the Instron 8801 material strength tester (see Figure 6.8). The tests were carried out at the Mechanical Engineering Department on the Cape Town Campus of CPUT.

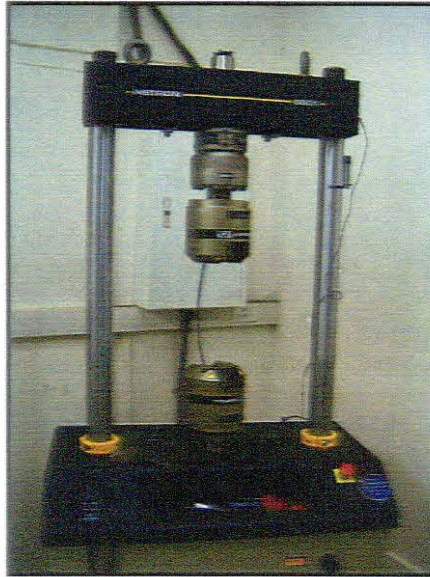


Figure 6.8: The Instron 8801 material strength tester

Since the machine is used to test the tensile strength of materials much larger than the plastic samples, an adaptor had to be constructed to mount the plastic sample without interfering with the welding joint.

An easy solution for this was to use two 100mm iron rods with a diameter of 10mm to clamp into the jaws of the tester. A square piece of metal plate (length of 50mm and width of 50mm) was welded onto each able to mount a welded sample. To ensure the welded area remained unaffected, a hole was machined in the centre of the metal plate. The plastic sample could then be glued onto the metal plates and clamped like a sandwich. The glue used to attach the sample to the metal plate was cyanoacrylate (commonly known as Super Glue) with specified tensile bond strength of 210 kg/cm<sup>2</sup> (Bostik, 2007).

The bond formed by the Super Glue was not strong enough for the tensile strength tests, so Pratley Steel Quickset was used instead. The bond made by the Super Glue was torn off at a pulling force of 230 N. The strength of the bond made by Pratley Steel Quickset glue was stated as 20 MPa on the manufacturer's datasheet (Pratley, 2009). This glue was also not strong enough and broke loose from the plastic as the sample was being pulled. Finally, after consulting a plastics expert, it was suggested Pratley 1-2-3 be used; Pratley 1-2-3 forms a better bond with plastic materials (Pratley, 2009).



Figure 6.9: The adaptors used to secure the samples for tensile strength tests

### 6.1.3 The chemical quality test

For this test a glass jar with a screw-on lid was half-filled with acetone. The lid had to be fastened tightly as the acetone was ketone based and would evaporate if not covered. The plastic samples were then fully immersed (see Figure 6.10).

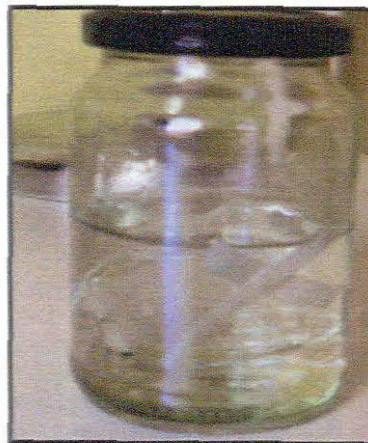


Figure 6.10: A spot welded sample immersed in acetone

The length of this test was chosen as three hours, within the recommended time for such chemical test. One of each of the samples shown in Figures 6.3 – 6.7 was tested to see assess the overall quality of the spot welded samples. The results of the tests are discussed in Section 6.1.4.

### 6.1.4 Plastic welding test conclusion

The acceptable weld strength for plastic welding joints was taken to be 75% of the strength of the base material (Kamweld, 2003).

The pure ABS samples in Figure 6.4 were tested to have weld strength of 1035 N. This is 99.4 % of the tensile strength of the base material with the same diameter; the ABS strip the

e width of the welding tip had a tensile strength of 1041 N (see appendix H). These specimens are seen in plots 3 and 5 in Figure H3.

The PVC sample in Figure 6.6 was tested to have a joint strength of 213.5 N (see appendix H). The results thereof could be seen in plot 6 in Figure H3. The base PVC strip had a tensile strength of 233.3 N, which means the spot weld on the PVC sample had strength of 91.5 % of the base material of that width. The result of this specimen is shown in plot 1 in Figure H3.

The welding joint of the polyester sample in Figure 6.5 was pulled apart at a pulling force of 161.86 N (see appendix H). The base polyester sample strip had a tested 217.94 N tensile strength (see appendix H). The results of these specimens are shown in plot 4 and 2 in Figure H3 respectively.

The chemical quality test was performed on all spot welded plastic samples. None of the samples separated from the spot weld and the weld remained perfect; no swelling was noted at the spot welding joints.

The transducer was loaded with a polypropylene sample and the captured waveforms of the unfiltered (top) and filtered (bottom) signal is shown in Figure 6.11.

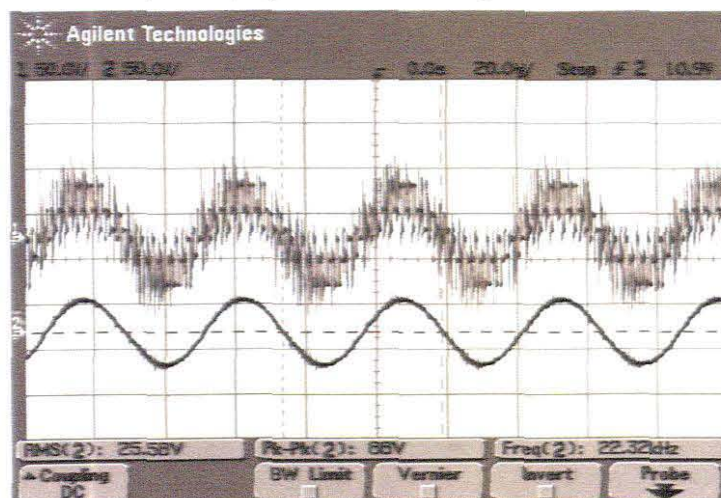


Figure 6.11: Unfiltered and filtered waveforms while performing plastic welding

After the two tests were completed and results were evaluated, it was evident the system could produce good quality spot welds. The weld strength was, however, largely influenced by the downward force applied to the welding tool and the time taken to perform a weld. For a hand-held tool, these factors were determined by the skill of the user.

## 6.2 Testing the system as an ultrasonic drill

The difference between the drilling operation and the welding operation with the same horn tip was the downward force applied to the transducer tool. When even a Newton or above extra force was applied in the downward position by hand the tip will drill through plastic and other materials. The thicker plastic samples unsuitable for spot welding with an ultrasonic plastic spot welder were used to test the drilling operation. Photos of the drilled samples are shown in Figure 6.12 – Figure 6.16.



Figure 6.12: The top view of a 17mm thick HDPE sample after being drilled

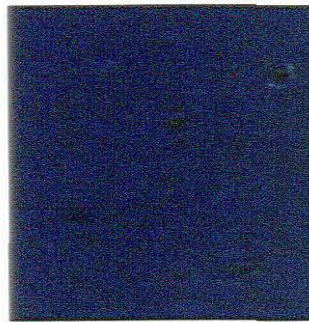


Figure 6.13: The bottom view of Figure 6.12

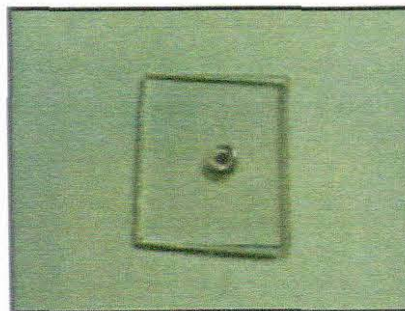


Figure 6.14: Drilled 3.0mm Perspex sample



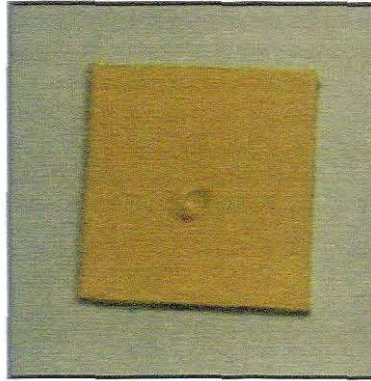


Figure 6.15: Drilled 3.0mm polypropylene sample

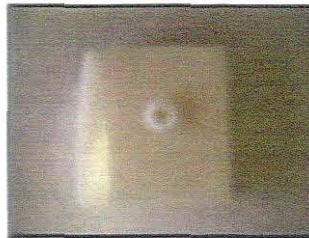


Figure 6.16: Drilled acetal sample

These were exposed to the drilling operation for 5 seconds and downward force from a free hand applied to the transducer. As can be seen from results, the 17mm HPDE sample was drilled through in 5 seconds multiple times. The 3mm plastic sample was also easily drilled through within 5 seconds. However, the 3mm PP sample was drilled to a depth of only 2.2 mm. The acetal sample could also reach a drilling depth of only 1.8 mm.

### 6.3 Conclusions

A method for testing the effectiveness of the system as a plastic spot welder was presented and results shown. To determine if the system could be implemented for other ultrasonic applications, it was tested as an ultrasonic drill. Because of its tip shape and size it suited itself to that application quite easily. Chapter Seven draws up the final conclusions of the research and evaluates if the research aims and objectives asked at the beginning of the study were achieved.

## **CHAPTER SEVEN CONCLUSIONS AND RECOMMENDATIONS**

This chapter presents a summary of the work covered in this thesis, the conclusions drawn from the experimental results and recommendations for future work in this field.

### **7.1 Auxiliary power supply**

An auxiliary power supply was designed and built to operate from the same DC voltage as the multicell inverter and each output had to be electrically isolated. The design of the power supply was discussed in the thesis. It was successfully tested on the multicell inverter used in the project and the results shown in Chapter Five.

### **7.2 Multicell inverter**

The multicell inverter was introduced and the design discussed in detail in Chapter Four. A 3 cell (4 level) multicell inverter was designed and built successfully. The inverter was designed to operate with a switching frequency of 300 kHz per cell, relating to a 900 kHz apparent switching frequency as seen by the load. The inverter was tested successfully with both resistive and ultrasonic loads and the results were presented in Chapter Five.

Benefits noted from using the multicell inverter topology were as follows:

- high switching frequency resulted in a smaller output filter necessary for a conventional class-D inverter,
- the voltage sharing nature of the inverter resulted in smaller switches and
- lower conduction losses reduced the size of the heat sink; in this case a PCB heat sink was designed and implemented.

### **7.3 Ultrasonic plastic welding system**

The ultrasonic plastic welding system in general operated effectively. The power supply was able to drive the ultrasonic transducer in plastic welding operations over the entire experimental period. The ultrasonic transducer with the available horn tip melted and various plastics samples as shown in Chapter Six. It also welded thin plastic strips together. The system will work even better if a horn tip is designed specifically for plastic welding applications.

### **7.4 Conclusions to main research question**

The main problem in this study was to discover if the multicell inverter could drive a non-linear load. An ultrasonic transducer was chosen as the non-linear load for this study. From the results presented in Chapter Five it can be seen the multicell inverter was capable of

driving an ultrasonic load successfully at a fixed frequency. The efficiency of the multicell inverter with an ultrasonic load was calculated to be 95.6 %.

To be able to easily simulate various inverter topologies with an ultrasonic transducer, the next problem was to research and implement a simple yet accurate method of measuring an equivalent model for the transducer. Chapter Three discussed the ultrasonic transducer as an electrical load and a simple equivalent circuit for the transducer from previous research was presented and used. The actual versus measured results for this model were presented in Chapter Three and as in Appendix G.

After proving the successful operation of the multicell inverter with an ultrasonic transducer, the next challenge was to see whether the inverter and transducer combination could produce an effective plastic weld. Various thermoplastic samples were sourced. The information regarding the strength of an effective weld also had to be researched to measure the experimental welding joint strengths. The results shown in Chapter Five suggests with correct application from the welder (using the correct welding force and welding time), an ultrasonic plastic welding machine could produce effective and strong welds; where the weld strength is higher than 75 % of the strength of the base material (Kamweld, 2003).

After developing a system for ultrasonic plastic welding, the next question was if the system was versatile enough for other ultrasonic applications. It was easy to test the system for ultrasonic drilling as the horn tip of the transducer was more suited to this application. The difference in the ultrasonic welding and drilling application came down to the downward force applied to the transducer. The system was tested as a drill on various plastic samples which were thicker than the ideal range for welding operating. The results shown in Chapter Six indicated the ultrasonic transducer tool worked excellently as a drill on both thermoplastics and thermosets. This proved its versatility in application of the ultrasonic transducer tool and power supply combination.

## **7.5 Thesis contributions**

The main contributions of this thesis are as follows:

- it was the first time that a multicell inverter topology had been implemented on an ultrasonic load. The multicell inverter worked well with both resistive and ultrasonic loads. It proved that a non-linear load could be driven with a multicell inverter. A comprehensive background study was carried out and no reference was found of any work in this area that has been done previously.
- a quick and effective electrical model for an ultrasonic transducer was presented to simulate an inverter with an ultrasonic load electrically and

- this work proved the versatility of the ultrasonic transducer tool and power supply combination. This opened doors for the use of this inverter topology in other ultrasonic areas, i.e. ultrasonic cutting, ultrasonic drilling and ultrasonic cleaning.

## **7.6 Future work**

Future work should focus on the following areas:

- Size optimisation by redesigning circuit boards and using surface mount packages for all components. Also to replace the T0220 MOSFET packages with direct-FET packages to reduce the effect of the parasitic inductance and capacitance caused by the package manufacturing.
- Redesign the entire inverter system to be on one circuit board.
- Control system to control the welding process.
- Implementation of a mode locking technique such as admittance locking.
- Implement a variable PWM to the buck converter to automatically adjust the bus voltage on turn-on of the power supply.

## REFERENCES

- Anon. 2002. *Switchmode™ Power Supply Reference Manual, Rev.3A*. <http://www.onsemi.com> [10 April 2008].
- Anon, *Power MOSFET*. [http://en.wikipedia.org/wiki/Power\\_MOSFET](http://en.wikipedia.org/wiki/Power_MOSFET) [15 January 2008].
- Bostik. 2007. *Bostik superglue technical data sheet*. <http://bostik.co.za> [30 July 2009].
- Boylstadt, R.L. 1994. *Introductory Circuit Analysis*. 7<sup>th</sup> Edition. Merril.
- Bracewell, R. 1965. *The Fourier Transform and Its Applications*. McGraw Hill.
- Butterworth, S. *On a Null Method of Testing Vibration Galvanometers*. Proc. Phy. Soc. (London). 26: pp. 264 – 273.
- Chang, K. 2003. *Improving the transient response of a bolt-clamped Langevin transducer using a parallel resistor*. Ultrasonics 41, pp. 427-436.
- Davies, J. 2002. *Continuous Wave Mode Locking for the Determination of the Acoustic Nonlinearity Parameter B/A*. PhD thesis, Electrical Engineering, University of Cape Town, 2002.
- De Bruyn, T., De Vries, I., Mortimer, B., Tapson, J. 2001. *High Power Resonant Tracking Amplifier Using Admittance Locking*. Ultrasonics 39, pp. 257 – 261.
- Dukane Corporation, 2005. *Ultrasonic Probes/Stacks – Understanding and Caring For The Heart of Your Ultrasonic System*. <http://www.dukcorp.com/us> [21 March 2008].
- Green, A.G. *The design of high power ultrasonic transducers*. MSc Thesis, Electrical Engineering, University of Cape Town, April 2002, pp. 101 -121.
- Hamma, F., Meynard, F., Tourkhani, P., Viarogue. 1995. *Characteristics and Design of Multilevel Choppers*. IEEE PESC95 Conference Proceedings, Atlanta, USA: 1208 – 1214.
- ISA (Instrument Society of America). 1962. *ISA transactions*. Plenum Press, New York.
- Iula, A., Lamberti, N., Pappalardo, M. 2002. *Behaviour of the electromechanical coupling factor of cylinder shaped piezoceramics with different aspect ratios*. Universitadi Salerno, Via Ponte don Melillo, 84084, Fisciano (SA), Italy. Forum Acusticum. Sevilla.
- Janocha, H. 2007. *Adaptronics and Smart Structures: Basics, Materials, Design, and Applications*. Springer.
- Kaiser, K.L. 2004. *Electromagnetic compatibility handbook*. CRC Press, pp.1413.
- Killen, H. 1985. *Modern Electronic Communication Technologies*. Macmillan.
- Kamweld. 2003. *Plastic Welding*. <http://www.kamweld.com> [20 June 2009].
- Kou, X., Corzine, K.A., Y.Familiant. *Full Binary Combination Schema for Floating Voltage Source Multi-Level Inverters*. IEEE Transactions on Power Electronics, vol. 17, number 6, pp. 891 – 897.
- Lai, J., Peng, F.Z. *Multilevel Converters – A New Breed of Power Converters*. IEEE Transactions on Industry Applications, vol. 32, pp. 509 – 517, May/June 1996.

- Levy, M., McAvoy, B.R. 1993. *Ultrasonics Symposium 1993*. IEEE Ultrasonics, and Frequency Control Society, Institute of Electronics Engineers, Ferroelectrics IEEE Ultrasonics. University of Michigan. Page 875.
- Ling, S., Luan, J., Li, X., Ang, W. 2006. *Input electrical impedance as signature for nondestructive evaluation of weld quality during ultrasonic welding of plastics*. NDT&E International 39, pp. 13 -18.
- Malloy, R.A. 1994. *Plastic part design for injection molding: an introduction*. Published by Hanser Verlag. Page 405,
- Mason, W.P. 1935. *An electromechanical representation of a piezoelectric crystal used as a resonator*. Proc. IRE, Vol.23, no. 10, pp 1252 – 1263.
- Meynard, T.A., Foch, H. 1992. *Multi-level Conversion: High Voltage Choppers and Voltage – Source Inverters*. Proceedings of the IEEE Power Electronics Specialist Conference, pp. 397-403.
- Meynard, T.A., Foch, H. 1995. *Multilevel converters and derived topologies for high power conversion*. Industrial Electronics, Control, and Instrumentation. Proceedings of the 1995 IEEE IECON 21st International Conference. Vol. 1, pp:21 - 26
- Meynard, T.A., Foch, H., Forest, F., Turpin, C., Richardeau, F., Delmas, L., Gateau, G. and Lefeuvre. 2002. *Multicell Converters : Derived Topologies*. IEEE Transactions on Industrial Electronics, Vol. 49, No.5, October, 2002.
- Microchip Corporation. *PIC 16F87X Datasheet*.  
<http://ww1.microchip.com/downloads/en/DeviceDoc/30292c.pdf> [12 June 2008].
- Mistry, K. 1997. *Plastic welding technology for industry*. Assembly Automation 17, pp.196 – 200.
- Mohan, N., Underland, T.M., Robbins, W.P. 1989. *Power Electronics: Converters, Applications and Design*. New York: Wiley.
- Molepo, S.A.2003.*A Multilevel Inverter for DC Reticulation*.M.Sc. thesis, University of Stellenbosch.
- MPInterconsulting. 2002. *BLTW Ultrasonic plastic welding transducers*. <http://www.mpi-ultrasonics.com/transducer-bltw.html> [19 January 2009].
- Peric, L. 2004. *Coupled Tensors of Piezoelectric Materials State*. MPI.
- Powerex application note.2007 .*General Considerations: IGBT and IPM Modules*.  
[www.pwr.com](http://www.pwr.com) [15 March 2008].
- Pratley. 2009. *Pratley steel quickset technical information*.  
<http://www.pratleydistributing.com> [30 September 2009]
- Rajagopal, K. 2008. *Textbook of engineering physics - Part i*. PHI Learning Pvt. Ltd.
- Rodriguez, J., Lai, J.S., Peng, F.Z. 2002. *Multilevel inverters: A survey of topologies, controls and applications*. IEEE transaction on industrial electronics, vol. 49, no. 4, pp. 724-738.
- Society of Plastics Industry, Inc. 1976. *Plastics Engineering Handbook*. Fourth Edition.

Edited by Joel Frados. Van Nostrand Reinhold Company.

Soto, D., Green, T.C.2002. *A comparison of high-power converter topologies for the implementation of facts controllers*. IEEE transactions on Industrial Electronics, vol. 49, no. 5, pp. 1072 – 1080.

Stansfield, D. 1990. *Underwater Electroacoustic Transducer*. Bath University Press and Institute of Acoustic.

Suslick, K.S.1988. *Ultrasound: Its Chemical, Physical and Biological Effects*. Published by VCH Publishers. University of Michigan.

Tan, L. 2008. *Digital Signal Processing – Fundamentals and Applications*. Academic Press, Elsevier.

Tolbert, L.M., Peng, F.Z. 1998. *Multilevel converters for large electric drives*. IEEE Applied Power Electronics Conference (APEC-1998),pp.530-536.

Troughton, M.J. 2008. *Handbook of Plastics Joining: A Practical Guide*. International Institute of Welding. Edition 2. Page 15. Published by William Andrew.

Tsujino, J., Ueoka, T., Hasegawa, K., Fujita, Y., Shiraki, T., Okada, T. and Tamura, T. 1996. *New methods of ultrasonic welding of metal and plastic materials*. Ultrasonics 34, pp. 177 – 185.

Tsujino, J., Hongoh, M., Yoshikuni, M., Hashii, H. and Ueoka, T. 2004. *Welding characteristics of 27, 40 and 67 kHz ultrasonic plastic welding systems using fundamental and higher-resonance frequencies*. Proceedings of Ultrasonics International 2003. Vol. 42, Issues 1-9, pp. 131 – 137.

Van Dyke, K. 1925. *The Electric Network Equivalent of a Piezoelectric Resonator*, volume 895A. Phys. Rev.25.

Vishay Products. *SUM75N04-05L datasheet*.  
<http://www.vishay.com/mosfets/list/product-73247/> [10 April 2008].

Welding Technology Institute of Australia (WTIA), 2006. *Ultrasonic welding of plastics used in medical devices*. <http://www.wtia.com.au> [15 February 2008].

Wolbert, B. *Designing P.C.Board Heat Sinks*. Micrel, 2006.

Wu, A.M., Xiao, J., Markovic, D., Sanders, S.R. 1999. *Digital PWM control: Applications in voltage regulation modules*. IEEE Power Electronics Specialists Conference, Charleston, SC, vol.1, pp. 77 – 83, June 1999.

## APPENDICES

### APPENDIX A: ABBEON CAL, INC. ULTRASONIC PLASTIC WELDER QUOTE

## ABBEON CAL, INC.

800.922.0977 805.966.0810 WWW.ABBEON.COM  
123 GRAY AVENUE, SANTA BARBARA, CA 93101-1809



## ORDER QUOTATION

Date: March 5, 2009

Following is the quotation you requested:

Company Name: Cape Peninsula University of Technology  
Contact Name: Edward Davies  
Phone: 27 21 4603808 email: daviese@cput.ac.za  
Delivery Address: Cnr Keizergrach and Tennant Street  
Zonnebloem, Cape Town  
Western Cape 7500  
South Africa

#### Items Requested

Item#	Qty	Description	Unit Price	Extended Price
H540/CV54	1	Ultrasonic Handheld Welder 40kHz, 5000W	\$4,800.00	\$4,800.00
H540/CV54horn	1	Horn for Model H540/CV54 Ultrasonic Welder	\$650.00	\$650.00

Please specify type of welding horn tip when ordering. See  
Abbeon.com for options

Subtotal	\$5,450.00
Funds transfer fee	\$40.00
Shipping Chg	\$589.00
<b>Total</b>	<b>\$6,079.00</b>

Payment Terms: Shipment upon receipt of Funds Transfer

Wire Transfer to: Santa Barbara Bank & Trust, Santa Barbara, CA 93101

Account Name: Abbeon Cal Inc., Routing # 122220593, account # 08108383

FOB: Shipping Point, Massachusetts

Shipping Method: UPS Worldwide Expedited

Lead Time: 4 to 6 weeks

Estimated delivery time: 6-8 days

Quotation expiration: June 30, 2009

Thank you for your request!

Sincerely,

Bob Brunzman  
VP Marketing



**APPENDIX B: SHARPERTEK ULTRASONIC WELDER SPECIFICATIONS AND QUOTE**

**Ultrasonic Handheld Welder**

**Welds, Spot Welds, Stakes, and Inserts**

**Model H520/CV52**

Frequency/Power:	20 kHz: 500 watts
Input Voltage:	Standard 120 volts or optional 220 volts 50/60 Hz Regulated between 95-135 volts or 190-65 volts.
Weld Time:	0.1-9.9 seconds
Dimensions:	8.5in H x 13.5in W x 7.5in D (216mm H x 340mm W x 190mm D)
Weight:	10lbs. (4.5kg.)
Hand Gun Specs:	
Dimensions:	1.9in (48.3mm) D, 7.6in (193mm)L (w/ std. tip)
Weight:	1.5 lbs (0.68kg)
Horn:	Integral with threaded end to accept replaceable tips
Material:	Titanium
Tip:	Standard- 1/2"(12.7mm) diameter flat faced titanium tip (see chart for other tips)
Cable Specs:	Hardwired into hand gun. (optional detachable cable available)
Lengths:	10ft standard (optional 15ft or 25ft available)



These 500-watt welders contain two overload protection circuits, one for the power supply and the other for the converter. The systems overload circuit protects the power supply from exceeding its maximum wattage. The advanced converter protection circuit is designed to protect against excessive voltage or current caused by the application. With a response time of less than 2 micro-seconds, these circuits instantaneously prevent internal component damage to the power supply and converter.

**Model H540/CV54**

Frequency/Power:	40 kHz: 500 watts
Input Voltage:	Standard 120 volts or optional 220 volts 50/60 Hz Regulated between 95-135 volts or 190-265 volts.
Weld Time:	0.1-9.9 seconds
Dimensions:	8.5in H x 13.5in W x 7.5in D (216mm H x 340mm W x 190mm D)
Weight:	10lbs. (4.5kg.)
Hand Gun Specs:	
Dimensions:	1.9in (48.3mm) D, 6.3in (160mm)L (w/ std. tip)
Weight:	1.5 lbs (0.68kg)
Horn:	Supplied and Priced Separately
Material:	Titanium or Aluminum
Cable Specs:	Hardwired into hand gun. (optional detachable cable available)
Lengths:	10ft standard (optional 15ft or 25ft available)

(ORDER HORN AND TIP SEPARATELY)

Hi;  
The 500 Watt Machine is \$3500. It includes the horn.

The machine alone is \$3200.00.

The Voltage is 220 Volts.

Regards;

Gus N  
Sharpertek  
2005 Pontiac Road Unit A  
Auburn Hills MI 48326  
Tel: 248-340-0593  
Cel: 248-930-9653  
Fax: 248-340-6189  
[www.SharperTek.com](http://www.SharperTek.com)

This message is intended only for the use of the Addressee(s) and may contain information that is PRIVILEGED, CONFIDENTIAL and/or EXEMPT FROM DISCLOSURE under applicable law. If you are not the intended recipient, you are hereby notified that any disclosure, copying, distribution, or use of the information contained herein is STRICTLY PROHIBITED. If you received this communication in error, please destroy all copies of the message, whether in electronic or hard copy format, as well as attachments and immediately contact the sender by replying to this email. Thank you!

-----Original Message-----

From: SALES SHARPERTEK [<mailto:sales@sharpertek.com>]  
Sent: Thursday, March 05, 2009 11:18 AM  
To: Gus N  
Subject: FW: 500 W ultrasonic plastic welder

-----Original Message-----

From: Edward Davies [<mailto:DaviesE@cput.ac.za>]  
Sent: Thursday, March 05, 2009 8:11 AM  
To: [sales@sharpertek.com](mailto:sales@sharpertek.com)  
Subject: 500 W ultrasonic plastic welder

To whom it may concern,

I wish to receive a formal quotation via e-mail for a 500W ultrasonic plastic welding system (portable). Could you please quote me (1) for a 500W supply and the transducer/horn and (2) only the power supply.

Thank you.

Regards,  
Edward Davies

Edward Davies  
CPUT M&V Team Member  
Cape Peninsula University of Technology  
Tel.: 021 460 3808  
Email: [daviese@cput.ac.za](mailto:daviese@cput.ac.za)

## APPENDIX C: CALCULATED EQUIVALENT CIRCUIT PARAMETERS OF THE ULTRASONIC TRANSDUCER WITH BOOSTER AND HORN IN VARIOUS LOAD CONDITIONS

### Transducer, Booster and horn in free Air

$C_o$	= 587.57pF
$C_m$	= 105,13pF
$R_m$	= 8.051 ohm
$L_m$	= 0.50701 H
$f_m$	= 21800 Hz
$f_{ar}$	= 23670 Hz
$Y_{max}$	= 0.1243 S
$Y_{min}$	= 9.12e-005 S
$ Z_m $	= 8.0451 ohm
$ Z_{ar} $	= 1.0965e+004 ohm

### Transducer, Booster and horn with Polypropylene (PP) as load

$C_o$	= 683.14 pF
$C_m$	=120.58 pF
$R_m$	=14.816 ohm
$L_m$	= 0.44002 H
$f_m$	= 21850 Hz
$f_{ar}$	= 23700 Hz
$Y_{max}$	= 0.0676 S
$Y_{min}$	= 1.0620e-004 S
$ Z_m $	= 14.7929ohm
$ Z_{ar} $	= 9.4162e+003 ohm

### Transducer, Booster and horn with High Density Polyethylene (HDPE) as load

$C_o$	= 701.25 pF
$C_m$	= 123.660 pF
$R_m$	= 14.086 ohm
$L_m$	= 0.42828 H
$f_m$	= 21870 Hz
$f_{ar}$	= 23720 Hz
$Y_{max}$	= 0.0711 S
$Y_{min}$	= 1.0910e-004 S
$ Z_m $	= 14.647 ohm
$ Z_{ar} $	= 9.1659e+003ohm

### Transducer, Booster and horn with Polyvinyl Chloride (PVC) as load

$C_o$	= 620.02 pF
$C_m$	= 110.21 pF
$R_m$	= 12.706 ohm
$L_m$	= 0.48274 H
$f_m$	= 21820 Hz
$f_{ar}$	= 23680 Hz
$Y_{max}$	= 0.0788 S
$Y_{min}$	= 9.6300e-005 S
$ Z_m $	= 12.6904 ohm
$ Z_{ar} $	= 1.0384e+004 ohm

Transducer, Booster and horn with Perspex as load

$C_o$  = 623.73 pF  
 $C_m$  = 114.14 pF  
 $R_m$  = 15.797 ohm  
 $L_m$  = 0.46741 H  
 $f_m$  = 21790 Hz  
 $f_{ar}$  = 23700 Hz  
 $Y_{max}$  = 0.0634 S  
 $Y_{min}$  = 9.7100e-005 S  
 $|Z_m|$  = 15.7729 ohm  
 $|Z_{ar}|$  = 1.0299e+004 ohm

APPENDIX D: SCHEMATIC DIAGRAMS

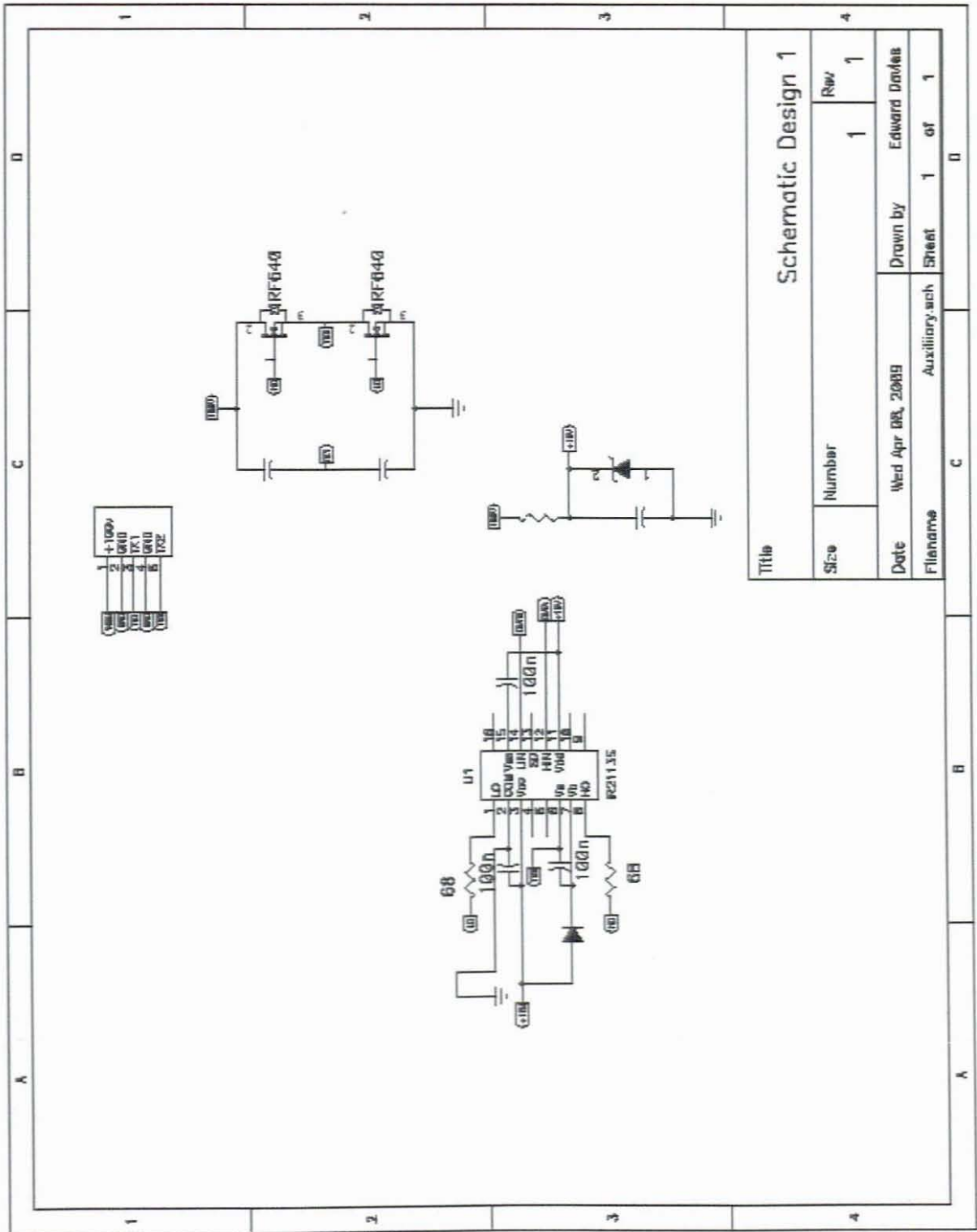
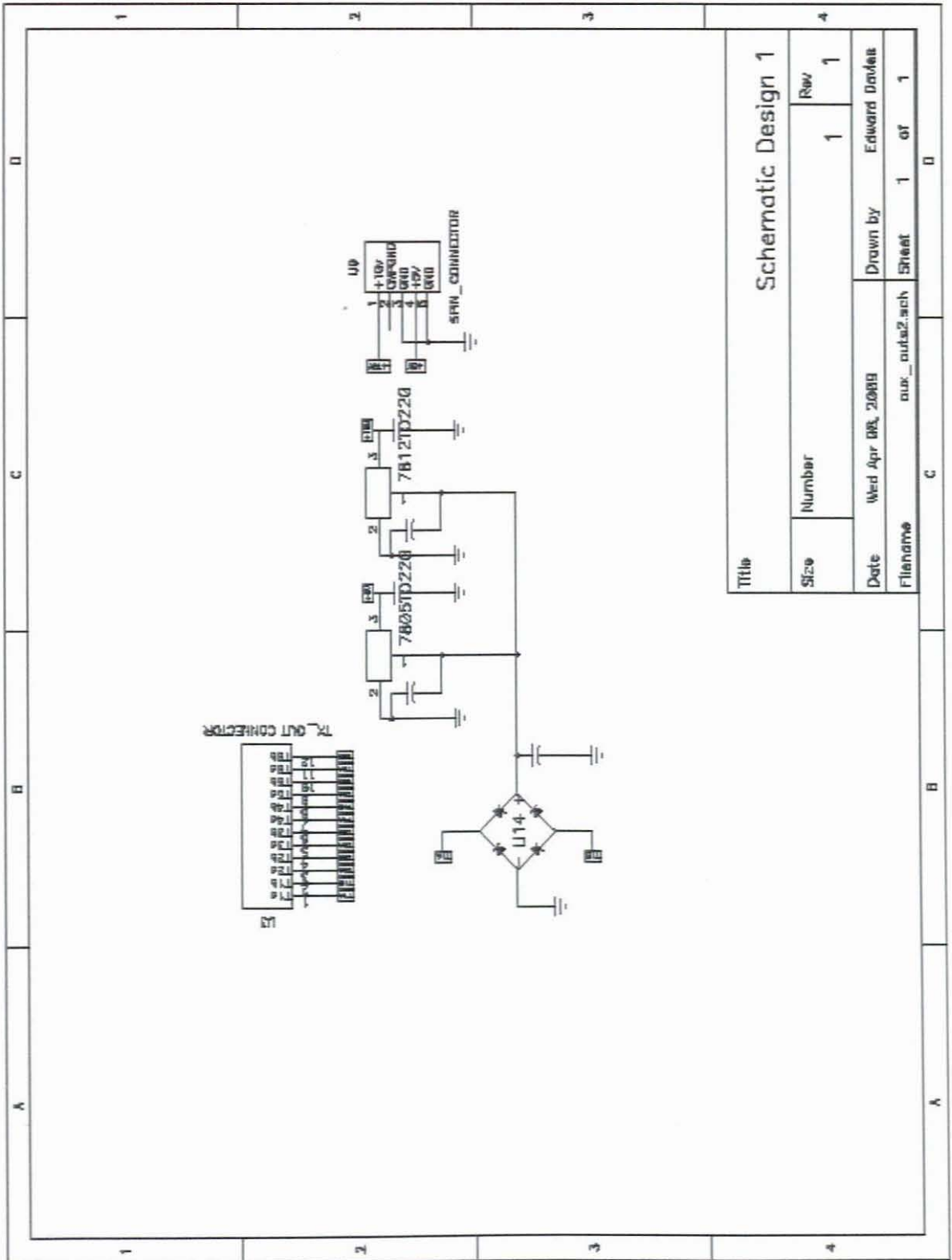


Figure D1: PCAD Schematic of the auxiliary power supply half-bridge inverter stage



Title		Schematic Design 1	
Size	Number	1	1
Date	Drawn by	Wed Apr 08, 2009	Edward Davies
Filename	Sheet	aux_outa2.sch	1 of 1

Figure D2: PCAD Schematic of the auxiliary power supply regulator stage

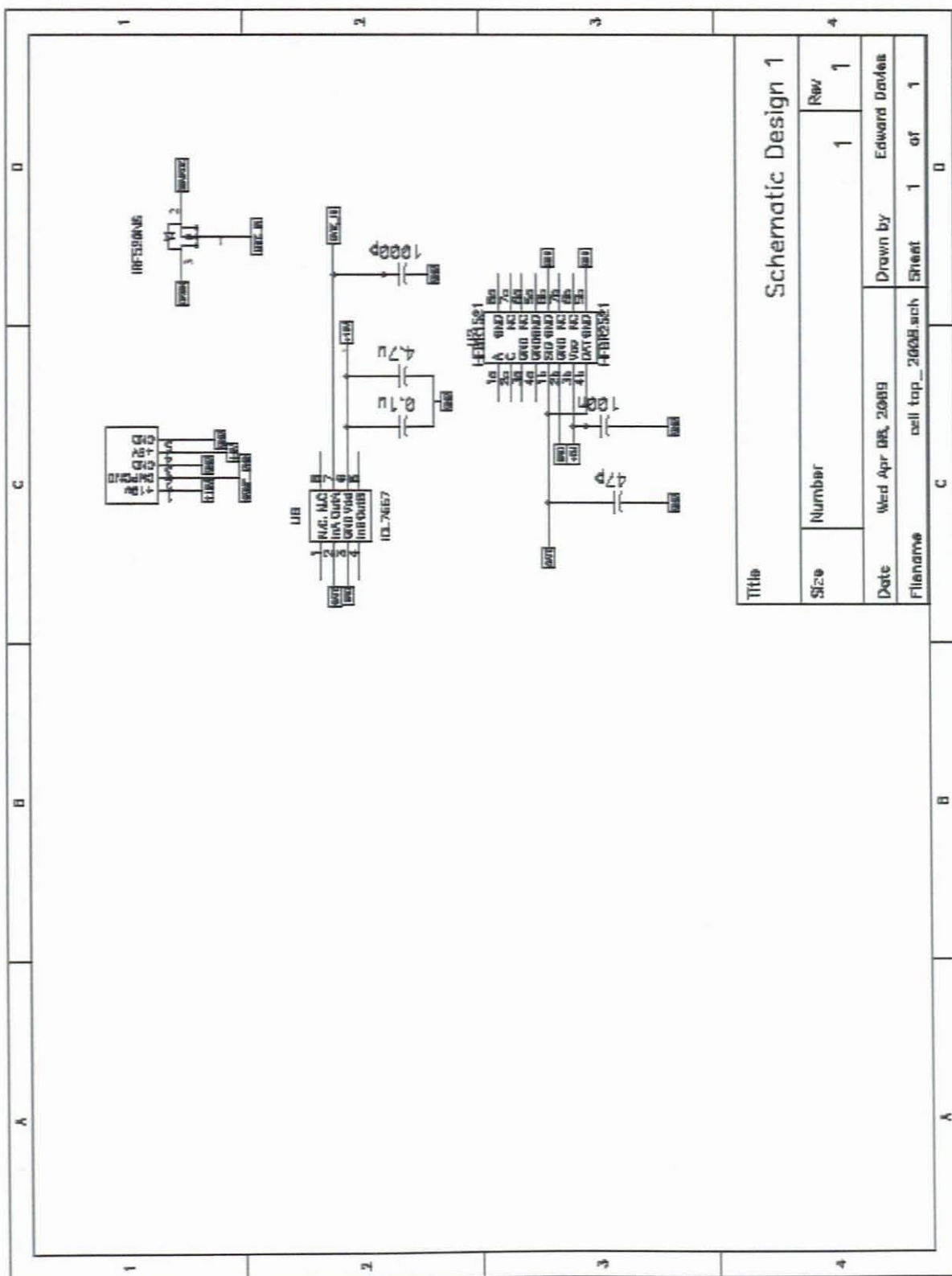


Figure D3: PCAD Schematic of the high side switch circuit for a single cell of multicell inverter

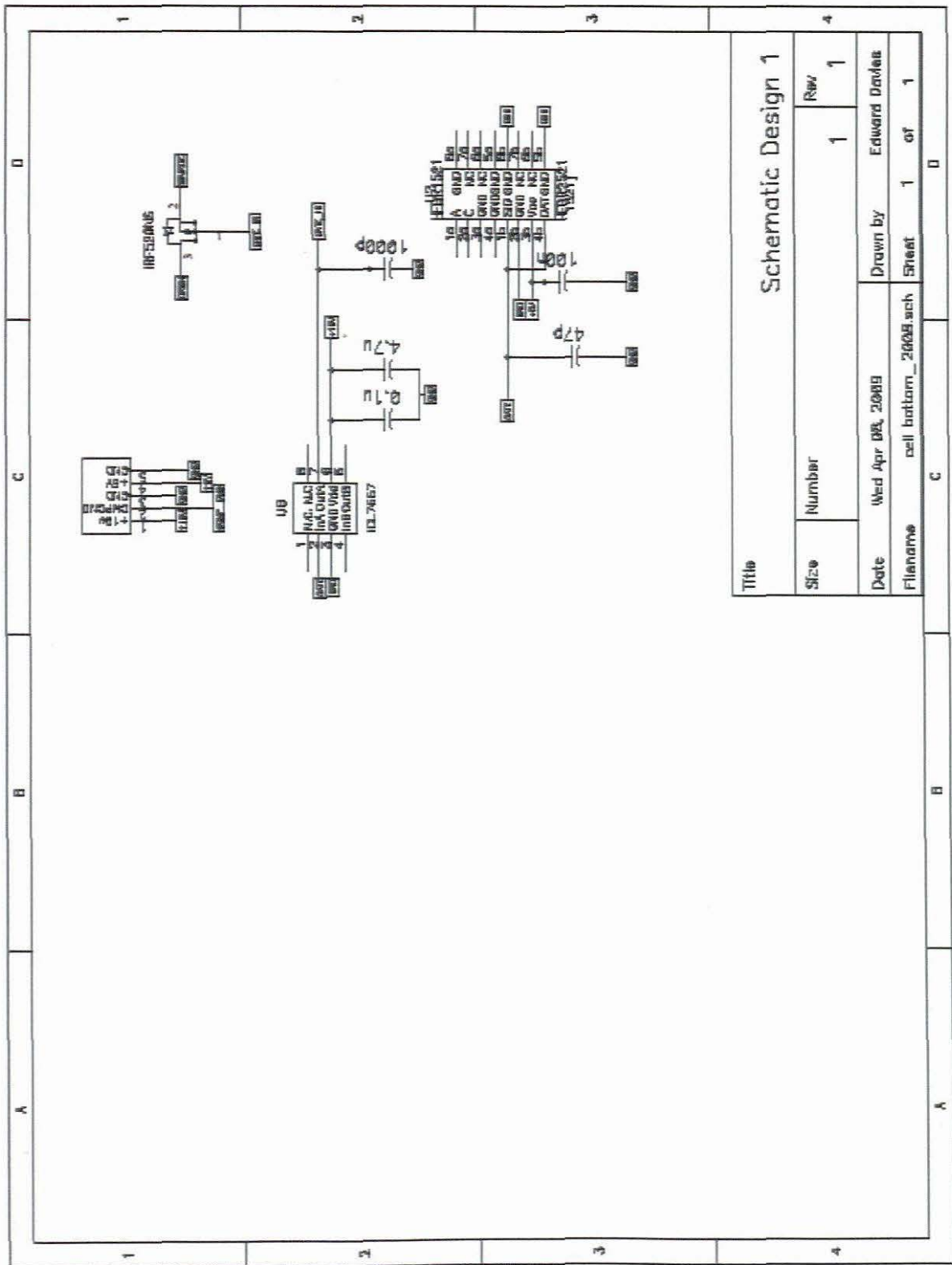


Figure D4: PCAD Schematic of the low side switch circuit for a single cell of multicell inverter



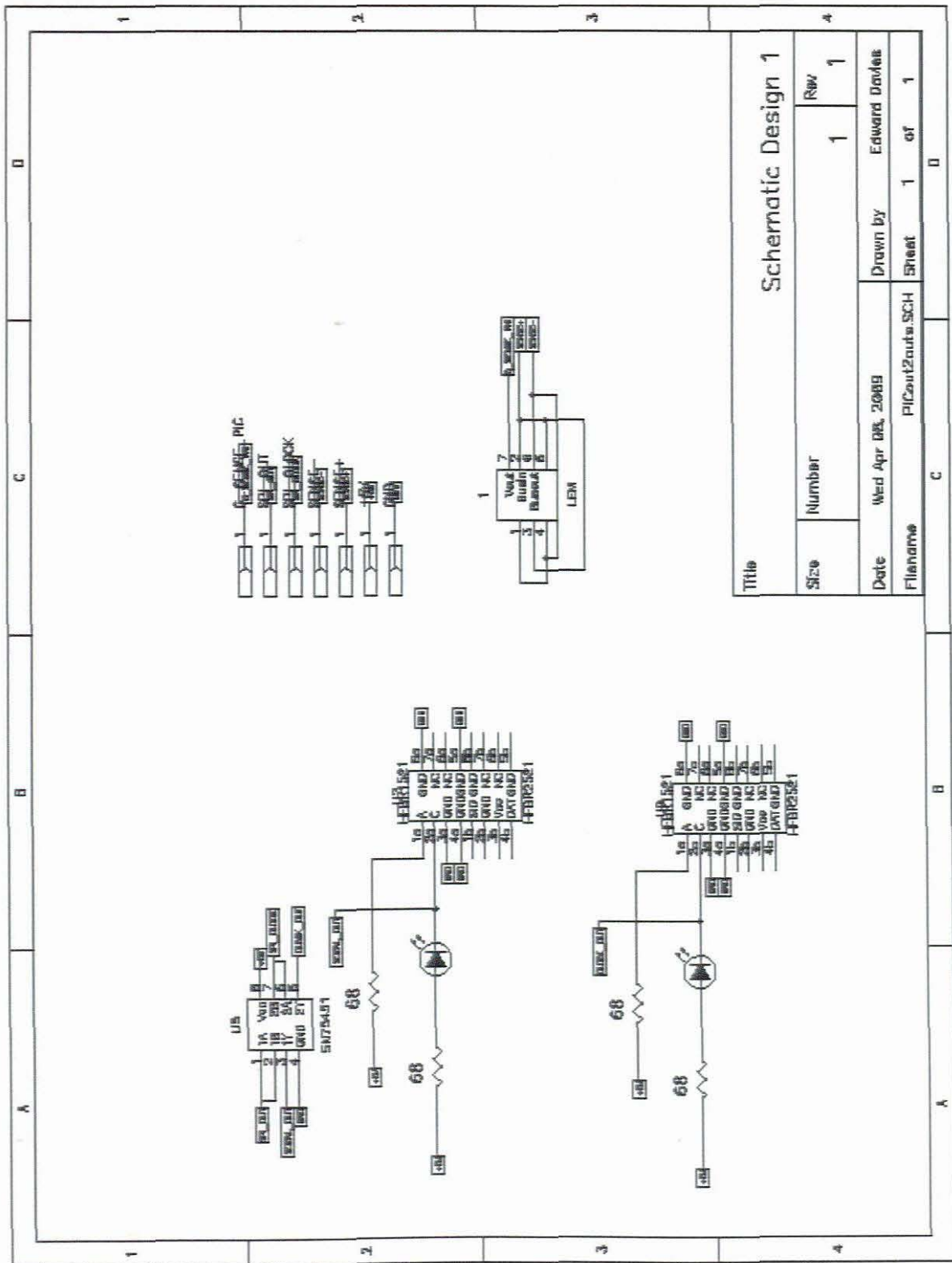
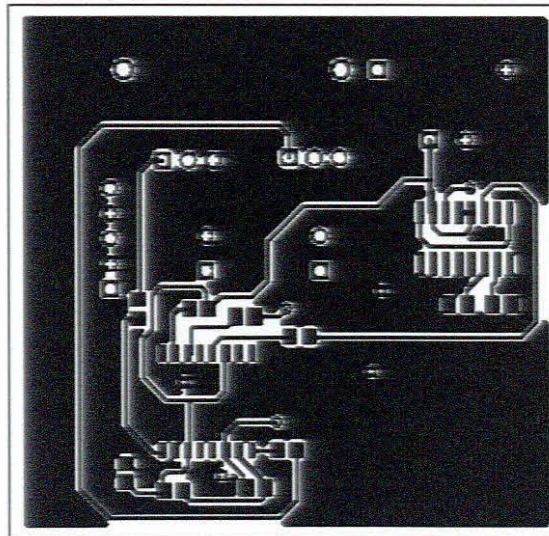
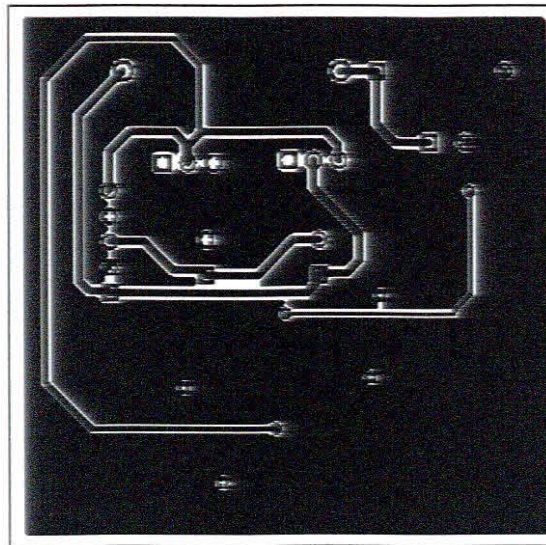


Figure D5: PCAD Schematic of the microcontroller interface board

## APPENDIX E: PCB LAYOUTS



Initials and Surname:	Edward Davies
Supervisor Name:	Dr. R.H. Wilkinson
Student Number:	202008576
Scale:	2:1
Board Type:	Double Sided
Layer Identifier	Top Layer
Boards Required:	1



Initials and Surname:	Edward Davies
Supervisor Name:	Dr. R.H. Wilkinson
Student Number:	202008576
Scale:	2:1
Board Type:	Double Sided
Layer Identifier	Bottom Layer
Boards Required:	1

Figure E1: PCAD PCB layout of the half-bridge inverter for auxiliary power supply

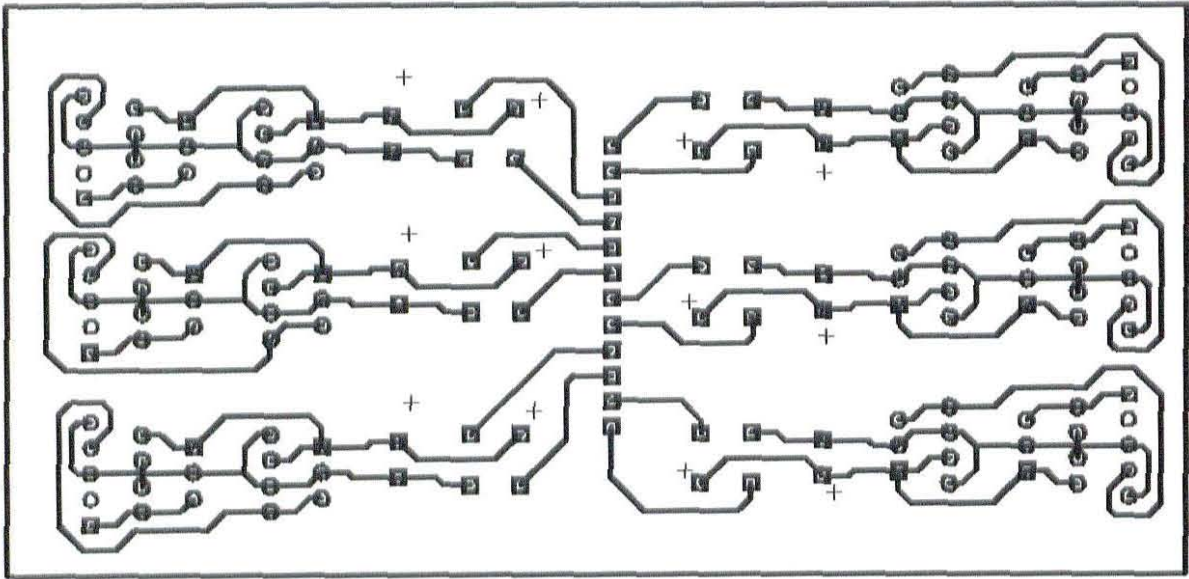
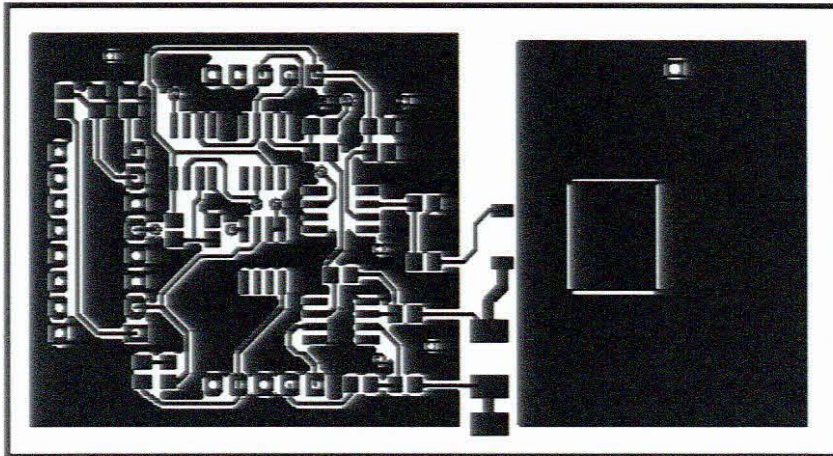
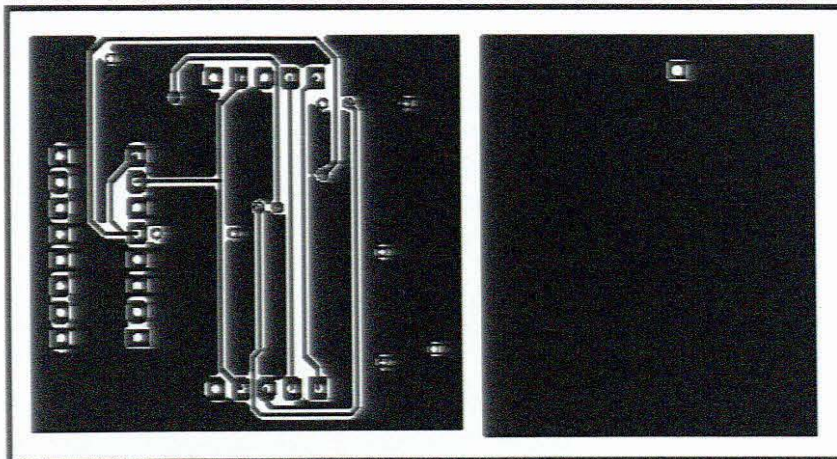


Figure E2: PCAD PCB layout of regulating stage for auxiliary power supply

Initials and Surname:	Edward Davies
Supervisor Name:	Dr. R.H. Wilkinson
Student Number:	202008576
Scale:	2:1
Board Type:	Single Sided
Layer Identifier	Bottom Layer
Boards Required:	1

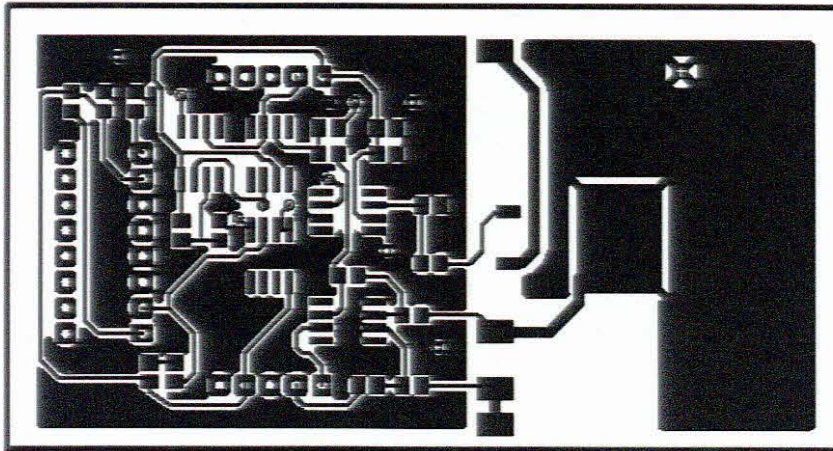


Initials and Surname: Edward Davies  
 Supervisor Name: Dr. R.H. Wilkinson  
 Student Number: 202008576  
 Scale: 2:1  
 Board Type: Double Sided  
 Layer Identifier: Top Layer  
 Boards Required: 1

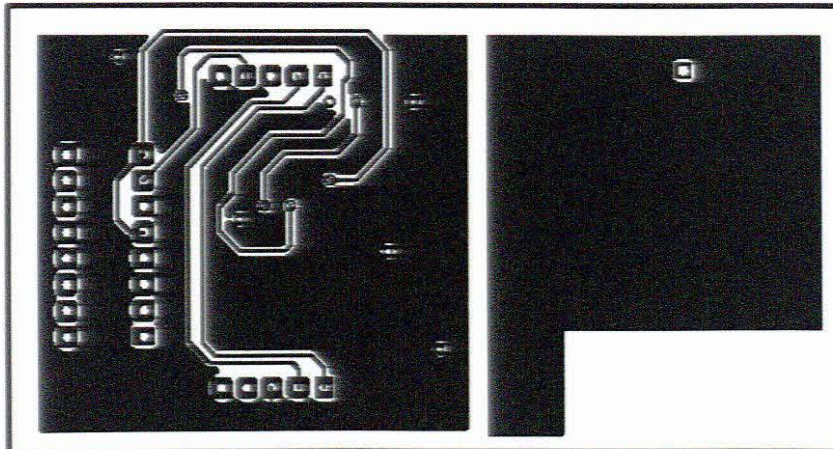


Initials and Surname: Edward Davies  
 Supervisor Name: Dr. R.H. Wilkinson  
 Student Number: 202008576  
 Scale: 2:1  
 Board Type: Double Sided  
 Layer Identifier: Bottom Layer  
 Boards Required: 1

Figure E3: PCAD PCB layout of the high side switch of the single cell of a multicell inverter

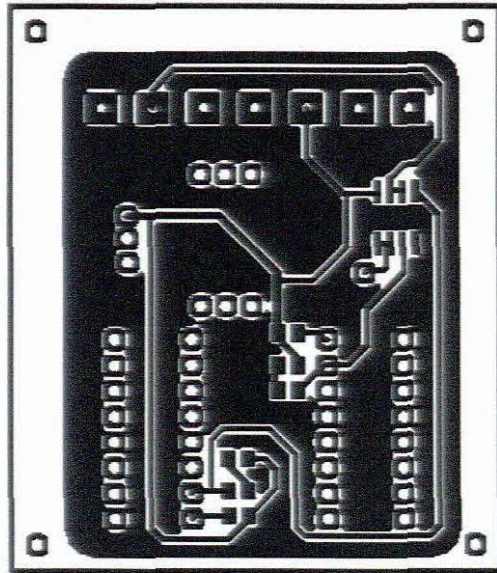


Initials and Surname: Edward Davies  
 Supervisor Name: Dr. R.H. Wilkinson  
 Student Number: 202008576  
 Scale: 2:1  
 Board Type: Double Sided  
 Layer Identifier: Top Layer  
 Boards Required: 1

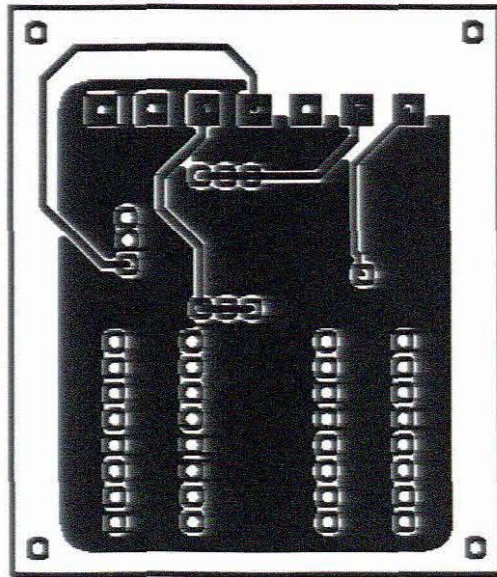


Initials and Surname: Edward Davies  
 Supervisor Name: Dr. R.H. Wilkinson  
 Student Number: 202008576  
 Scale: 2:1  
 Board Type: Double Sided  
 Layer Identifier: Bottom Layer  
 Boards Required: 1

Figure E4: PCAD PCB layout of the low side switch of a single cell of the multicell inverter



Initials and Surname:	Edward Davies
Supervisor Name:	Dr. R.H. Wilkinson
Student Number:	202008576
Scale:	2:1
Board Type:	Double Sided
Layer Identifier	Top Layer
Boards Required:	2



Initials and Surname:	Edward Davies
Supervisor Name:	Dr. R.H. Wilkinson
Student Number:	202008576
Scale:	2:1
Board Type:	Double Sided
Layer Identifier	Bottom Layer
Boards Required:	2

Figure E5: PCAD PCB layout of the microcontroller interface board



## APPENDIX F: PROGRAMME

### F.1 MATLAB

```
fm = 21790;
fn = 23700;
Ym = max (Y);
Yn = min (Y);
wn = 2*pi*fn;
wm = 2*pi*fm;
keff = sqrt (1 - (fm^2)/(fn^2));
Qm = (wn)/(2*(wn-wm)) * abs(Ym)/abs(Yn);
R1 = 1/(abs(Ym - Yn));
L1 = (Qm * R1) / wm;
C1 = 1 / (wm * Qm * R1);
Co = C1*(1/(keff^2) - 1);
Co = Co;
Lm = L1;
Rm = R1;
Cm = C1;
w = 2*pi.*frequency;
Z2 = Rm + j.*w.*Lm - (j./(Cm.*w));
Y2 = 1./Z2;
Z1 = -j./(Co.*w);
Y1 = 1./Z1;
Ytot = Y1 + Y2;
plot (frequency, abs(Ytot));
hold on
plot (frequency, Y, 'r');
```

**APPENDIX G: MEASURED AGAINST SIMULATED ADMITTANCE VERSUS FREQUENCY PLOTS OF THE ULTRASONIC TRANSDUCER WITH DIFFERENT LOADS**

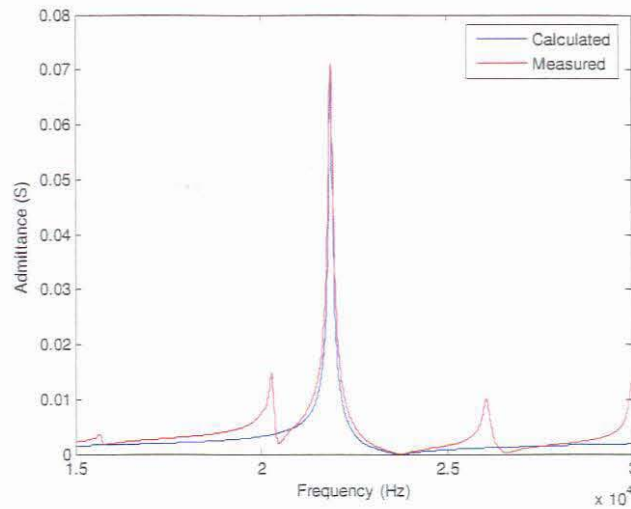


**Figure G1: A comparison between the measured admittance values versus frequency and the calculated values with the aid of a BVD model of a BLT transducer with a horn and booster and HDPE as a load**

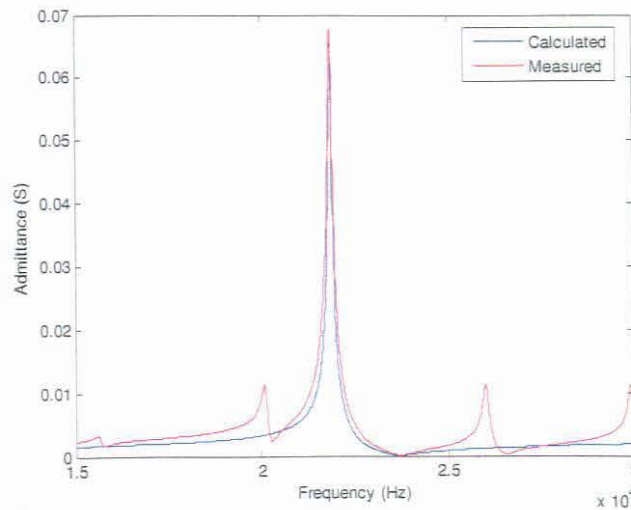


**Figure G2: A comparison between the measured admittance values versus frequency and the calculated values with the aid of a BVD model of a BLT transducer with a horn and booster and PP as a load**

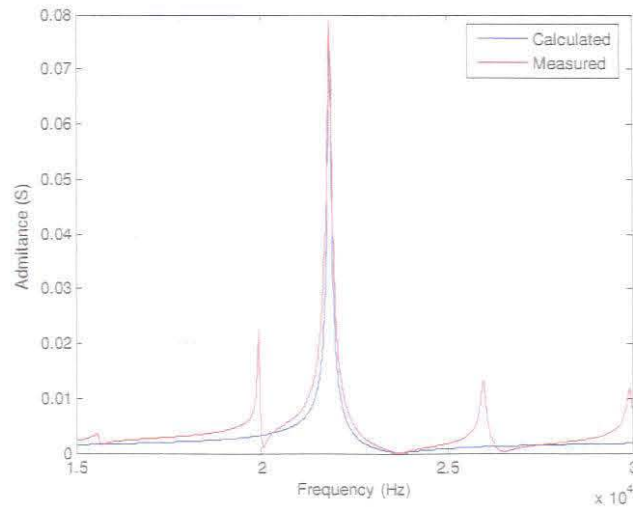


**Figure G3: A comparison between the measured admittance values versus frequency and the calculated values with the aid of a BVD model of a BLT transducer with a horn and booster and PVC as a load**

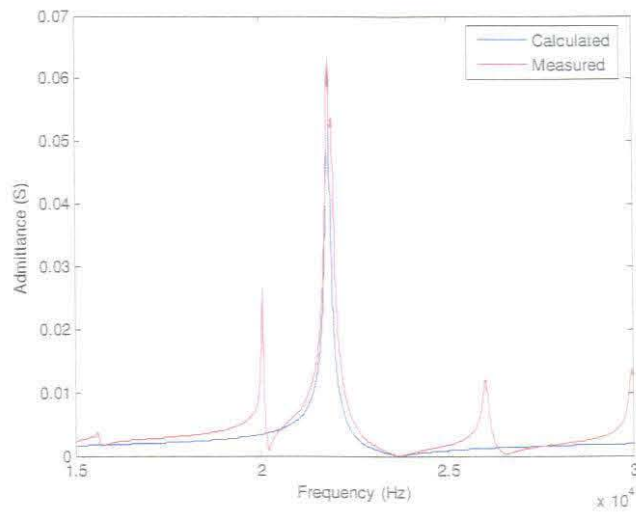


**Figure G4: A comparison between the measured admittance values versus frequency and the calculated values with the aid of a BVD model of a BLT transducer with a horn and booster and Perspex as a load**

## APPENDIX H: TENSILE STRENGTH TEST RESULTS

Specimen 1 to 1

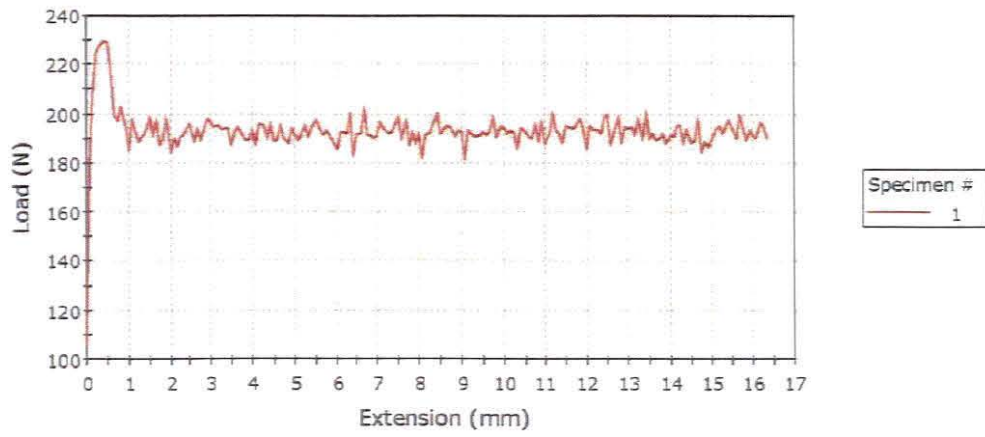


Figure H1: Tensile strength test of sample glued with Superglue

Specimen 1 to 1

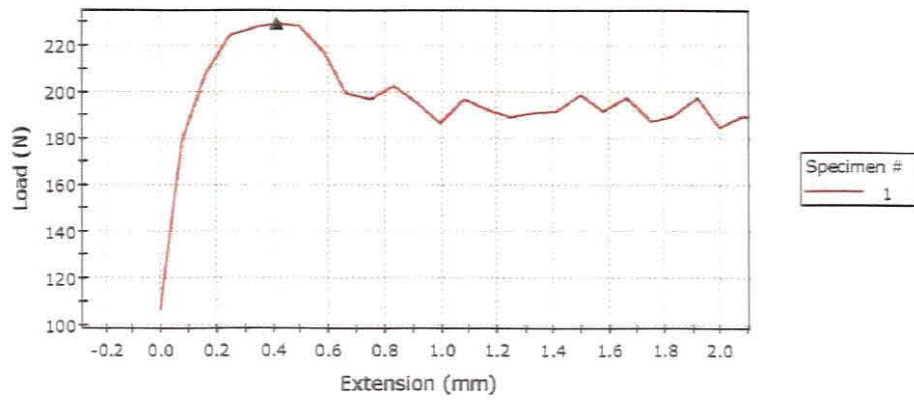


Figure H2: Tensile strength test of sample glued with Pratley Steel Quickset

	Maximum Load (N)
1	233,29258
2	217,97419
3	1035,16579
4	161,86237
5	1041,13817
6	213,46807

Various Plastic Specimens

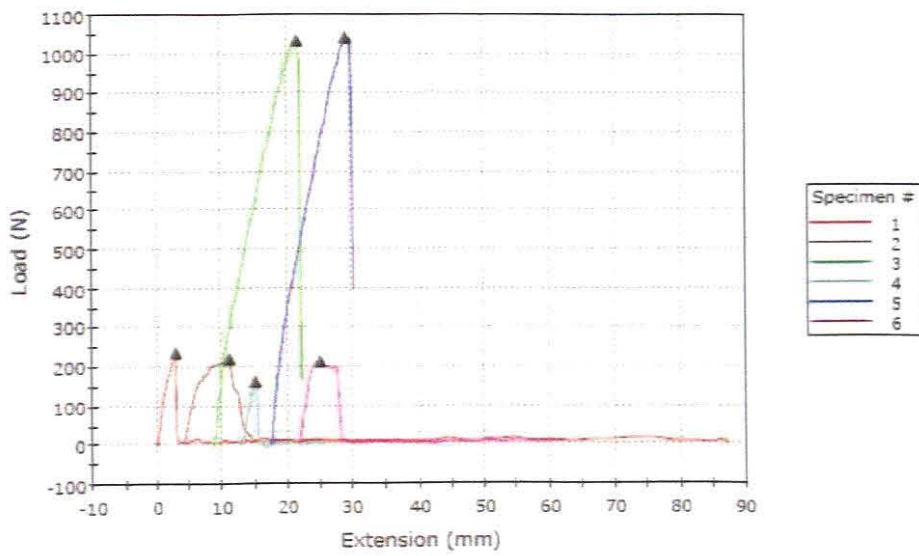


Figure H3: Tensile strength test of various samples glued with Pratley 1-2-3